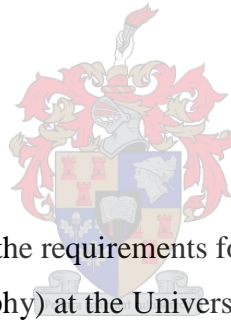


THE INFLUENCE OF GEOGRAPHIC FACTORS ON THE DISTRIBUTION OF NATURAL RADIONUCLIDES

by

Alwyn Petrus Geysler



Thesis presented in partial fulfilment of the requirements for the degree of MMil in Military Science
(Military Geography) at the University of Stellenbosch

Supervisors: Commander (Dr) J. Bezuidenhout
 Commander H.A.P. Smit

December 2017

DECLARATION

By submitting this research thesis, I declare that the entirety of the work contained therein is my own, original work, that I am the sole author thereof, that reproduction and publication thereof by Stellenbosch University will not infringe any third party rights and that I have not previously in its entirety or in part submitted it for obtaining any qualification.

Signature:

Date: December 2017

Copyright © 2017 Stellenbosch University

All rights reserved

ABSTRACT

The primordial radionuclides ^{40}K , ^{232}Th , and ^{238}U have been present in almost all rocks, soils, and minerals since the formation of Earth. These radionuclides emit gamma radiation that is detectable by means of a scintillation detector. By measuring the concentrations of ^{40}K , ^{232}Th , and ^{238}U in an area it is possible to draw radioelement maps. These radioelement maps were then used in a qualitative analysis to establish the influence of local geographic factors on the distribution of natural radionuclides. The research site is a granite outcrop, Baviaansberg, and the immediate area surrounding the outcrop. Baviaansberg is situated in the Saldanha Bay Military Area on the West Coast of South Africa.

The available literature on the impact of geographic factors on the distribution of natural radionuclides are limited. Scientific radioelement mapping in military areas in South Africa has only been completed by Bezuidenhout (2012). The research provided the opportunity to study the feasibility of establishing a link between natural radionuclide concentrations and geographic factors within a military area. Hence, the aim of the research was to investigate the relationship between geographic factors and the distribution of natural radionuclides of a particular area. Radioelement maps were used to analyse the impact of the respective geographic factors “geology”, “topography”, “soil type”, “hydrology”, “wind” and “human activity” on the distribution of the concentrations of natural radionuclides. Radiation measurements of the natural radionuclides in the research site were completed by means of *in situ* measurements using a NaI(Tl) scintillation detector connected to a tablet computer. Once the natural radionuclide concentrations were extracted by means of Full Spectrum Analysis (FSA), radioelement maps were created from the results. Qualitative analysis was performed on the radioelement maps by means of comparing it to the slope raster, slope profiles, a flow accumulation raster, wind data, Google Earth images, a human activities map, a soil type map, Spline vs Kriging raster, Th vs K raster, U vs K raster, and a U vs Th raster. The qualitative analysis aimed to establish the influence of the identified geographic factors on the spread of natural radionuclide concentrations.

The results indicated that the geology of an area influences the distribution of natural radionuclides. The highest concentrations of natural radionuclides were found close to the granite outcrops on Baviaansberg. Slope was used to determine the influence of topography. The results revealed that slope influences ^{40}K concentrations to a greater extent than ^{232}Th and ^{238}U concentrations due to the solubility of ^{40}K . The different soil types within Baviaansberg also displayed unique associated natural radionuclide

concentrations. According to the research results, the hydrology of Baviaansberg impacted on the spread of ^{40}K , ^{232}Th and ^{238}U concentrations. However, ^{40}K was influenced to a greater extent because of its solubility. The impact of the dry summer winds on the distribution of natural radionuclides became apparent through a comparison of the leeward and windward slopes of Baviaansberg. On the leeward slope higher concentrations of natural radionuclides were recorded than on the windward slope due to small particles that are removed from the windward slope and deposited on the leeward slope. Research results concerning the influence of human activities on the distribution of natural radiation were inconclusive. Further research needs to be conducted in order to confirm a definite relationship, should it in fact exist. True to the aim of the research, the study established that it is feasible to validate the influence of geographic factors on the distribution of natural radionuclides by analysing the natural radionuclide concentrations of an area.

OPSOMMING

Die primordiale radioaktiewe nukliëdes ^{40}K , ^{232}Th , en ^{238}U is reeds sedert die ontstaan van die aarde teenwoordig in byna alle rotse, grondtipes, en minerale. Hierdie nukliëdes straal gammastrale uit wat gemeet kan word met 'n sintillasiedetektor. Deur die konsentrasies van ^{40}K , ^{232}Th , en ^{238}U in 'n area te meet was dit moontlik om radioelementkaarte te teken. Die radioelementkaarte is dan gebruik gedurende kwalitatiewe-analise om die invloed van die lokale geografiese faktore op die verspreiding van die natuurlike radioaktiewe nukliëdes te bepaal. Die area geselekteer vir hierdie studie is 'n granietskop, Baviaansberg, en die onmiddellik omliggende area van die kop. Baviaansberg is geleë in die Saldanhaabaai Militêre Area aan die Weskus van Suid-Afrika.

The available literature on the impact of geographic factors on the distribution of natural radionuclides are limited. Scientific radioelement mapping in military areas in South Africa has only been completed by Bezuidenhout (2012). The research provided the opportunity to study the feasibility of establishing a link between natural radionuclide concentrations and geographic factors within a military area.

Die beskikbare literatuur wat die impak van geografiese faktore op die verspreiding van natuurlike radioaktiewe nukliëdes beskryf is beperk. Wetenskaplike radioelement kartering van militêre areas in Suid Afrika was nog net behartig deur Bezuidenhout (2012). Die navorsing bied die geleentheid om te bepaal of daar wel 'n verhouding is tussen die natuurlike radioaktiewe nukliëde konsentrasies and geografiese faktore in a militêre area. Die doel van die navorsing was om die verhouding tussen die geografiese faktore en die verspreiding van natuurlike radioaktiewe nukliëdes van 'n area te bepaal. Radioelementkaarte is gebruik om die impak van die geografiese faktore, geologie, topografie, grondtipe, hidrologie, wind- en menslike aktiwiteite, op die verspreiding van die konsentrasies van natuurlike radioaktiewe nukliëdes te ontleed. Die stralingmetings van die natuurlike radioaktiewe nukliëdes in die studie area is gedoen via *in situ*-opmetings deur gebruik te maak van 'n NaI(Tl) sintillasie detektor wat aan 'n tabletrekenaar gekoppel was. Die konsentrasies van die natuurlike radioaktiewe nukliëdes is met behulp van Volspektrumanalise bereken, waarna radioelementkaarte ontwikkel is. Kwalitatiewe-analise is met behulp van 'n hellingsraster op die kaarte, hellingsprofile, 'n vloei-opeenhopingsraster, winddata, Google Earth-beelde, 'n menslike aktiwiteitskaart, grondtipekaart, Spline- teenoor Kriging-raster, *Th*-teenoor *K*- raster, *U*- teenoor *K*-raster, en 'n *U*- teenoor *Th*-raster onderskeidelik uitgevoer. Dit is gedoen

om die invloed van die geïdentifiseerde geografiese faktore op die verspreiding van die natuurlike radioaktiewe nukliëdes te bepaal.

Die resultate dui daarop dat die geologie van 'n area die verspreiding van natuurlike radioaktiewe nukliëdes beïnvloed. Die hoogste konsentrasie van natuurlike radioaktiewe nukliëdes was naby aan die graniet-dagsome van Baviaansberg gevind. Helling is gebruik om die invloed van die topografie te bepaal. Die studie het bevind dat, as gevolg van die oplosbaarheid van ^{40}K , helling die ^{40}K -konsentrasies tot 'n meerdere mate as die ^{232}Th - en ^{238}U - konsentrasies beïnvloed. Die verskillende grondtipes binne Baviaansberg dui ook op unieke natuurlike radioaktiewe nukliëdkonsentrasies vir elke grondtipe. Volgens die resultate dui die hidrologie van Baviaansberg daarop dat die hidrolgie van 'n area die ^{40}K , ^{232}Th , en ^{238}U konsentrasies beïnvloed. Dog, as gevolg van sy oplosbaarheid, is ^{40}K die meeste beïnvloed. Die impak van die droeë somerwind op die verspreiding van radioaktiewe nukleïdes kom aan die lig wanneer die loefkant- en lykanthellings met mekaar vergelyk word. Die lykanthelling van Baviaansberg toon hoër konsentrasies natuurlike radioaktiwiteit as die loefkanthelling as gevolg van die verwydering van klein deeltjies aan die loefkant wat aan die lykant gedeponeer word. Resultate van die invloed van menslike faktore op die verspreiding van natuurlike radioaktiewe nukliëdes was onbeduidend. Verdere navorsing word aanbeveel om 'n bewysbare verband aan te toon. Getrou aan die die doel van hierdie navorsing, het die studie bewys dat dit moontlik is om die invloed van geografiese faktore op die verspreiding van natuurlike radioaktiewe nukliëdes te bepaal deur die natuurlike radioaktiewe konsentrasies van 'n area te analiseer.

KEY CONCEPTS

Denudation: The processes responsible for breaking down Earth's surface are jointly called denudation.

Full Spectrum Analysis: Full spectrum analysis (FSA) is a method used to convert the counts in the gamma spectrum to concentrations in Becquerel per kilogram. FSA uses the concept of obtaining standard unitary spectra of ^{40}K , ^{238}U and ^{232}Th separately. These standard spectra were then fitted onto the *in situ* spectrum by respectively adding each standard spectrum. The FSA process follows the principle of producing a combined spectrum from standard normalised spectra and fitting it to the spectrum of an unknown source.

Geographic Factors: Those geographic factors that influence soil development and distribution and, in turn, natural radionuclide distribution. In terms of this research, the factors considered were geology, topography, soil type, hydrology, wind, human influence.

GIS: Geographic Information System is a system that captures, stores, evaluates, analyses, manages and presents spatial data.

Natural Radionuclide Measurement: Measurement of the radiation of natural radionuclide concentrations by means of a detector.

Natural Radionuclides: The primordial radionuclides ^{40}K , ^{232}Th , and ^{238}U that emit gamma radiation responsible for natural radiation.

Radioelement Mapping: The mapping technique of using radiation measurements to create concentration maps of the measured radioelements.

Research Site: The physical location within the Saldanha Bay Military Area in which the field measurements for the study were completed.

ACKNOWLEDGEMENTS

To our Lord God Almighty for his unrelenting love and consistent care, especially during challenging times.

To my supervisors, Commander (Dr) Jacques Bezuidenhout and Commander Hennie Smit, thank you for your guidance, support and positive criticism. I am particularly grateful towards Cdr (Dr) Bezuidenhout for his guidance during field work and managing the challenges of radiation detection.

To my wife and children for being you. You always brought me back to reality on those days that I needed it most.

To Dr Tyrel Flügel for your valuable inputs and advice.

To Mr Richard Clarke for your assistance with Excel.

“But as for me and my house, we will serve the Lord.”

Joshua 24:15

TABLE OF CONTENTS

DECLARATION	ii
ABSTRACT	iii
OPSOMMING	v
KEY CONCEPTS.....	vii
ACKNOWLEDGEMENTS.....	viii
TABLE OF CONTENTS.....	ix
LIST OF TABLES.....	xiii
LIST OF FIGURES.....	xiv
LIST OF APPENDICES.....	xvi
LIST OF ACRONYMS AND ABBREVIATIONS	xvii
CHAPTER 1: INTRODUCTION.....	1
1.1 BACKGROUND AND RESEARCH SITE.....	1
1.1.1 Background	1
1.1.2 Research site	4
1.2 PROBLEM FORMULATION, RESEARCH AIM AND OBJECTIVES	6
1.2.1 Problem formulation	6
1.2.2 Research aim	7
1.2.3 Research objectives.....	7
1.3 RESEARCH SITE GEOLOGY	8
1.4 RADIOELEMENT MAPPING.....	9
1.5 NATURAL RADIONUCLIDE MEASUREMENT	10
1.6 RESEARCH DESIGN	12
1.7 THESIS OUTLINE	13

CHAPTER 2: DENUDATION PROCESSES IN THE PHYSICAL ENVIRONMENT AND NATURAL RADIATION 14

2.1	DENUATION IN THE PHYSICAL ENVIRONMENT.....	14
2.1.1	Geology of the physical environment	14
2.1.2	Weathering	15
2.1.3	Mass wasting.....	16
2.1.4	Erosion	17
2.1.5	Factors influencing denudation.....	18
2.2	GEOLOGY AND NATURAL RADIATION.....	20
2.2.1	Igneous rocks	20
2.2.2	Granite.....	21
2.2.3	Soil	22
2.2.4	Natural radionuclides and their decay series.....	22
2.3	PROPERTIES OF RADIATION	26
2.3.1	Fundamentals of radioactivity.....	26
2.3.2	Statistical behavior of radioactive decay	28
2.3.3	Gamma- ray photon interaction with matter	30
2.3.4	Detector response.....	33
2.4	DENUATION PROCESS IN THE PHYSICAL ENVIRONMENT AND NATURAL RADIATION	39

CHAPTER 3: RADIATION MEASUREMENT AND ANALYSIS ON BAVIAANSBERG 41

3.1	THE SALDANHA MILITARY AREA AND BAVIAANSBERG.....	41
3.2	RADIATION MEASUREMENT ON BAVIAANSBERG	46
3.2.1	Device setup and calibration.....	46
3.2.2	Sampling procedure	47
3.2.3	Data collection	49
3.3	FULL SPECTRUM ANALYSIS OF THE BAVIAANSBERG DATA.....	50
3.4	TECHNIQUES USED TO PREPARE DATA FOR QUALITATIVE ANALYSIS	55
3.5	RADIATION MEASUREMENT AND ANALYSIS ON BAVIAANSBERG.....	58

CHAPTER 4: THE INFLUENCE OF GEOGRAPHIC FACTORS ON THE DISTRIBUTION OF NATURAL RADIONUCLIDES59

4.1	DISTRIBUTION OF THE CONCENTRATION OF NATURALLY OCCURRING RADIONUCLIDES	59
4.1.1	Potassium distribution.....	59
4.1.2	Thorium distribution	62
4.1.3	Uranium distribution	64
4.2	RELATIONSHIP BETWEEN NATURAL RADIONUCLIDE CONCENTRATIONS AND PHYSICAL GEOGRAPHIC FACTORS	65
4.2.1	Geology	66
4.2.2	Slope.....	68
4.2.3	Soil type	76
4.2.4	Hydrological impact.....	78
4.2.5	Aeolian impact	84
4.2.6	Human impact	86
4.3	NATURAL RADIATION AND GEOGRAPHIC FACTORS	89

CHAPTER 5: CONCLUSION AND RECOMMENDATION91

5.1	BACKGROUND, AIM AND OBJECTIVES OF THE STUDY.....	91
5.2	GEOGRAPHIC FACTORS AND THEIR INFLUENCE ON NATURAL RADIONUCLIDE CONCENTRATIONS	93
5.3	THEORETICAL AND PRACTICAL IMPLICATIONS AND APPLICATIONS OF THE RESEARCH.....	94
5.4	LIMITATIONS AND POSSIBLE IMPROVEMENTS OF THE RESEARCH.....	95
5.5	UNANSWERED QUESTIONS AND NEW DIRECTIONS FOR FURTHER RESEARCH	96

LIST OF REFERENCES98

APPENDICES.....109

APPENDIX A:	COORDINATE AND CONCENTRATIONS TABLE	109
APPENDIX B:	⁴⁰ K ACTIVITY CALCULATIONS FROM NECSA CALIBRATIONS	125
APPENDIX C:	²³² Th ACTIVITY CALCULATIONS FROM NECSA CALIBRATIONS.....	126
APPENDIX D:	²³⁸ U ACTIVITY CALCULATIONS FROM NECSA CALIBRATIONS	127
APPENDIX E:	AN EXTRACT OF THE BINNED VALUES OF ⁴⁰ K.....	128

APPENDIX F: AN EXAMPLE OF THE STANDARD NORMALISED SPECTRA AND <i>IN SITU</i> SPECTRA DATA	129
APPENDIX G: EXTRACT OF THE TABLE FOR FSA.....	132
APPENDIX H: AN EXAMPLE OF A VISUAL FIT OF ONE OF THE MEASUREMENT POSITIONS	134

LIST OF TABLES

- Table 1.1, p 2 General representation of the typical concentrations of important radioactive elements in various rock types.
- Table 3.1, p 55 Index of selected measurement positions for error calculation, together with their error percentage and live time.

LIST OF FIGURES

- Figure 1.1, p 5 Google earth images indicating (a) position of Saldanha Bay on the West Coast of South Africa, (b) location of the Saldanha Bay Military Area and the research site, and (c) respective geographic positions of Baviansberg and Malgaskop.
- Figure 1.2, p 11 Basic block diagram of a NaI(Tl) detector (7.62 x 7.62 cm) setup.
- Figure 1.3, p 12 Schematic representation of research design.
- Figure 2.1, p 23 ^{40}K decay chain.
- Figure 2.2, p 24 ^{232}Th decay series.
- Figure 2.3, p 25 ^{238}U decay series.
- Figure 2.4, p 31 Incoming γ - ray photon undergoing Compton Scattering with electron.
- Figure 2.5, p 33 Interaction of γ - ray photons with matter.
- Figure 2.6, p 34 Energy spectrum demonstrating comparison of response functions between good and poor resolution.
- Figure 2.7, p 35 Example of energy spectrum.
- Figure 2.8, p 36 Graphic representation of intermediate size detector.
- Figure 2.9, p 37 Spectra that demonstrate interaction of γ - ray photon (with higher and lower energies) with detectors.
- Figure 2.10, p 38 Spectrum indicating influence of surrounding materials in incoming gamma-rays.
- Figure 3.1, p 42 Three-dimensional image extracted from DEM of Baviansberg.
- Figure 3.2, p 43 Areas of human activity in the research site.
- Figure 3.3, p 45 Soil type of the research site.
- Figure 3.4, p 47 NaI(Tl) scintillation detector.
- Figure 3.5, p 47 Clip of fishnet grid and predetermined measurement positions of research site.
- Figure 3.6, p 48 Distribution plot of GPS control point measurements.
- Figure 3.7, p 56 Comparison between ordinary Kriging and thin plate splines of ^{40}K concentration levels.
- Figure 4.1, p 60 ^{40}K concentration measurements.
- Figure 4.2, p 61 Distribution of ^{40}K concentrations as overlay on contour map of Baviansberg.
- Figure 4.3, p 62 ^{232}Th concentration measurements.
- Figure 4.4, p 63 Distribution of ^{232}Th concentrations as an overlay on the contour map of Baviansberg.

- Figure 4.5, p 64 ^{238}U concentration measurements.
- Figure 4.6, p 65 Distribution of ^{238}U concentrations as an overlay on contour map of Baviaansberg.
- Figure 4.7, p 66 Google Earth image of research site.
- Figure 4.8, p 67 Comparison between the ^{40}K , ^{232}Th , and ^{238}U concentrations to the granite outcrops of Baviaansberg.
- Figure 4.9, p 69 Comparison between the ^{40}K concentrations, slope raster and granite outcrops of Baviaansberg.
- Figure 4.10, p 70 Comparison between the ^{232}Th concentrations and slope raster.
- Figure 4.11, p 72 Comparison between the ^{238}U concentrations and slope raster.
- Figure 4.12, p 73 Google Earth image of the study area that indicates the positions of the transects used to determine the slope profile of Baviaansberg.
- Figure 4.13, p 74 Slope profile of Baviaansberg.
- Figure 4.14, p 76 Illustration of the ratio of the distribution of ^{232}Th to ^{40}K concentrations as an overlay on the contour map of Baviaansberg.
- Figure 4.15, p 76 Illustration of the ratio of the distribution of ^{238}U to ^{40}K concentrations as an overlay on the contour map of Baviaansberg.
- Figure 4.16, p 77 Soil types as an overlay on the radioelement map of ^{40}K .
- Figure 4.17, p 78 Soil Type as an overlay on the radioelement map of ^{232}Th .
- Figure 4.18, p 79 Soil Type as an over lay on the radioelement map of ^{238}U .
- Figure 4.19, p 80 Flow accumulation raster as an overlay on the contour map of Baviaansberg.
- Figure 4.20, p 82 Comparison between the ^{40}K concentrations and flow accumulation raster.
- Figure 4.21, p 83 Google Earth image of the research site indicating the areas with differences in values between Kriging and thin plate splines.
- Figure 4.22, p 84 Illustration of the ratio of distribution of ^{238}U to ^{232}Th as an overlay on the contour map of Baviaansberg.
- Figure 4.23, p 85 Comparison of the (a) flow accumulation raster, (b) the granite outcrops and (c) the ratio of ^{238}U to ^{232}Th .
- Figure 4.24, p 86 Wind direction distribution of the Saldanha area.
- Figure 4.25, p 87 Human activities as an overlay on the radioelement map of ^{40}K .
- Figure 4.26, p 88 Human activities as an overlay on the radioelement map of ^{232}Th .
- Figure 4.27, p 88 Human activities as an overlay on the radioelement map of ^{238}U .
- Figure 4.28, p 89 Human activities as an overlay on the map that indicates the ratio of $^{232}\text{Th}/^{40}\text{K}$.
- Figure 4.29, p 90 Human activities as an overlay on the map that indicates the ratio of $^{238}\text{U}/^{40}\text{K}$.

LIST OF APPENDICES

- Appendix A: Coordinate and Concentrations Table
- Appendix B: ^{40}K Activity Calculations from NECSA Calibrations
- Appendix C: ^{232}Th Activity Calculations from NECSA Calibrations
- Appendix D: ^{238}U Activity Calculations from NECSA Calibrations
- Appendix E: Extract of Binned Values of ^{40}K
- Appendix F: Example of Standard Normalised Spectra and *In Situ* Spectra Data
- Appendix G: Extract of Table for FSA
- Appendix H: Example of Visual Fit of one of the Measurement Positions

LIST OF ACRONYMS AND ABBREVIATIONS

CSIR	Council for Scientific and Industrial Research
DEM	Digital Elevation Model
FWHM	Full Width at Half Maximum
FCS	Clayey Sand with Weathered Granite Soil Type
FCQ	Fine to Coarse Sandy Soils with Coquina and Granite Outcrops Soil Type
FSA	Full Spectrum Analysis
GIS	Geographic Information Systems
GPS	Global Positioning System
IAEA	International Atomic Energy Agency
MCA	Multi-channel Analyser
NECSA	South African Nuclear Energy Corporation
SLG	Sandy Loam Soil with Granite Rocks Soil Type
SMA	Saldanha Bay Military Area

CHAPTER 1: INTRODUCTION

Chapter 1 provides the motivation for researching the impact of geographic factors on the distribution of natural radionuclides. It commences with a background explanation of geology, natural radiation and radioelement mapping, and also provides a description of the research site. Thereafter, the research problem is formulated, and research aim and objectives are discussed. The focus then shifts to a brief overview of the geology of the research site, radioelement mapping and natural radionuclide measurement. The chapter concludes with a schematic representation of the research design and a description of the outline of the thesis.

1.1 BACKGROUND AND RESEARCH SITE

This section provides a brief background on natural radionuclides and the physical environment as well as radioelement mapping and the applications thereof. Thereafter the research site was identified and discussed in terms of location and history of the area.

1.1.1 Background

Natural radiation sources were formed during the creation of the earth and have since been present in the physical environment (Wang 2002). These naturally occurring radioactive mineral deposits are found in apposite geological environments such as unconformity, veins and surficial deposits. The presence of primordial radionuclides in outcrops enhances the background radiation of a specific area (Baranwal 2006). Natural or environmental radiation is associated radiation from these primordial radioactive nuclides which have half-lives comparable to the age of Earth. These naturally occurring radionuclides are nuclides from the Potassium 40 (^{40}K), Uranium 238 (^{238}U) and Thorium 232 (^{232}Th) series (Albusini et al. 2008). These primordial radionuclides will be referred to as natural radionuclides. Trace quantities of these elements, together with their daughter nuclides, exist in all types of rock and soil. The concentration levels of ^{40}K , ^{232}Th , and ^{238}U and their daughters in soil are therefore dependent on the geology of the parent material from which the soil originates (Montes et al. 2012). Research by Bezuidenhout (2012) has also revealed that human activities play a role in altering the concentrations of natural radionuclides by disturbing the top soil.

The level of radioactivity depends on the type of rock and the mineral composition of the rock. The three radioelements responsible for natural radioactivity are ^{40}K , ^{232}Th , and ^{238}U . The amount of each of the aforementioned radioelements present in various rock types are presented in Table 1.1

Table 1.1 General representation of typical concentrations of important radioactive elements in various rock types (Adapted from Sharma 1997).

Rock type	Uranium (Bq/kg)	Thorium (Bq/kg)	Potassium (Bq/kg)
Granite	62	73	1176
Basalt	7	12	248
Shale	62	49	836
Sandstone	12	8	186
Limestone	22	7	93
Beach sand	37	24	93

From Table 1.1 it is evident that granite, compared to other rock types, contain relatively higher levels of radioelements. It can then be inferred that soil originating from granite will bear a similar radioactive signature.

Granite contains admixtures of ^{40}K , ^{232}Th , and ^{238}U (Arafa 2004; Llope 2011). The concentrations of the natural radionuclides may include daughter nuclides that emit gamma (γ) - ray photons with characteristic intensities and energies ranging from tens of keV to thousands of MeV (Llope 2011). γ -ray emissions, background radiation of these natural radionuclides, are measurable with a detector which makes it possible to map the variations in the distribution of natural radiation.

By mapping variations in the concentration of natural radionuclides it is possible to create radioelement maps. These radioelement maps are used in various academic and commercial applications. Radioelement mapping, for example, has been successfully used in uranium exploration and mining, geological mapping, and mineral and regolith mapping (Aboelkhair & Rabei 2012). Radioelement mapping has also been used in various studies and industries. It is regularly used in environmental studies to indicate the environmental impacts of natural radioactivity (El-Taher & Madkour 2011). It is also used in environmental assessments and monitoring of gamma-radiation contamination levels (Tyler 2004; Din

2009; Al-Sharkawy et al. 2012). Radioelement mapping may also be used to determine the influence of the deposition of heavy minerals and organic compounds in soil (Van der Graaf et al. 2007) and in coastal sediment, and in establishing the influence of deposition on the ecology and economy of a country (Obhodaš & Valković 2010). Radioelement maps can also be compiled of salt marsh environments that identify areas of greater risk of anthropogenic activity to living creatures (Tyler 1999). Radioelement mapping is used in geothermal studies to assist in determining the heat produced by radioactive decay in rocks which in turn is essential in aiding the explanation of the thermal history of Earth (Chiozzi et al. 2000; Abbady 2010).

In pedology, radioelement mapping is used to map soil erosion in cultivated fields through *in situ* radiometrics that will calculate the average rate of soil redistribution on archaeological sites (Tyler et al. 2001). Radioelement mapping is also used in the general mapping and assessing of erosion in any environment (Li et al. 2010). The mining industry uses radioelement mapping to determine places of larger concentrations of heavy mineral deposits (Macdonald et al. 1997; De Meijer 1998; Rozendaal et al. 1999). This will provide the mining industry with important information on the locality of specific minerals (Croft & Hutchinson 1999). Radioelement mapping is used as an economic and cost effective tool to determine possible mining sites in the petroleum and coal industries (Jibiri & Farai 2005), or as a monitoring tool for nuclear fallout. Regular measurements of a specific area serve as a monitoring system to detect nuclear fallout (Sowa et al. 1989; Baré & Tondeur 2011).

Medical studies also use radioelement mapping to measure long term radiation exposure (UNSCEAR 2000; UNSCEAR 2008). The monitoring process is aided by creating these radioelement maps to determine the exposure levels of the population to naturally occurring radiation (Ghiassi-nejad 2001; Karam 2002; Agbalagba & Onoja 2011). Archaeological studies use radioelement maps to map the distribution of potassium which could indicate locations of possible archaeological exploration (Moussa 2001, Reynolds 2011).

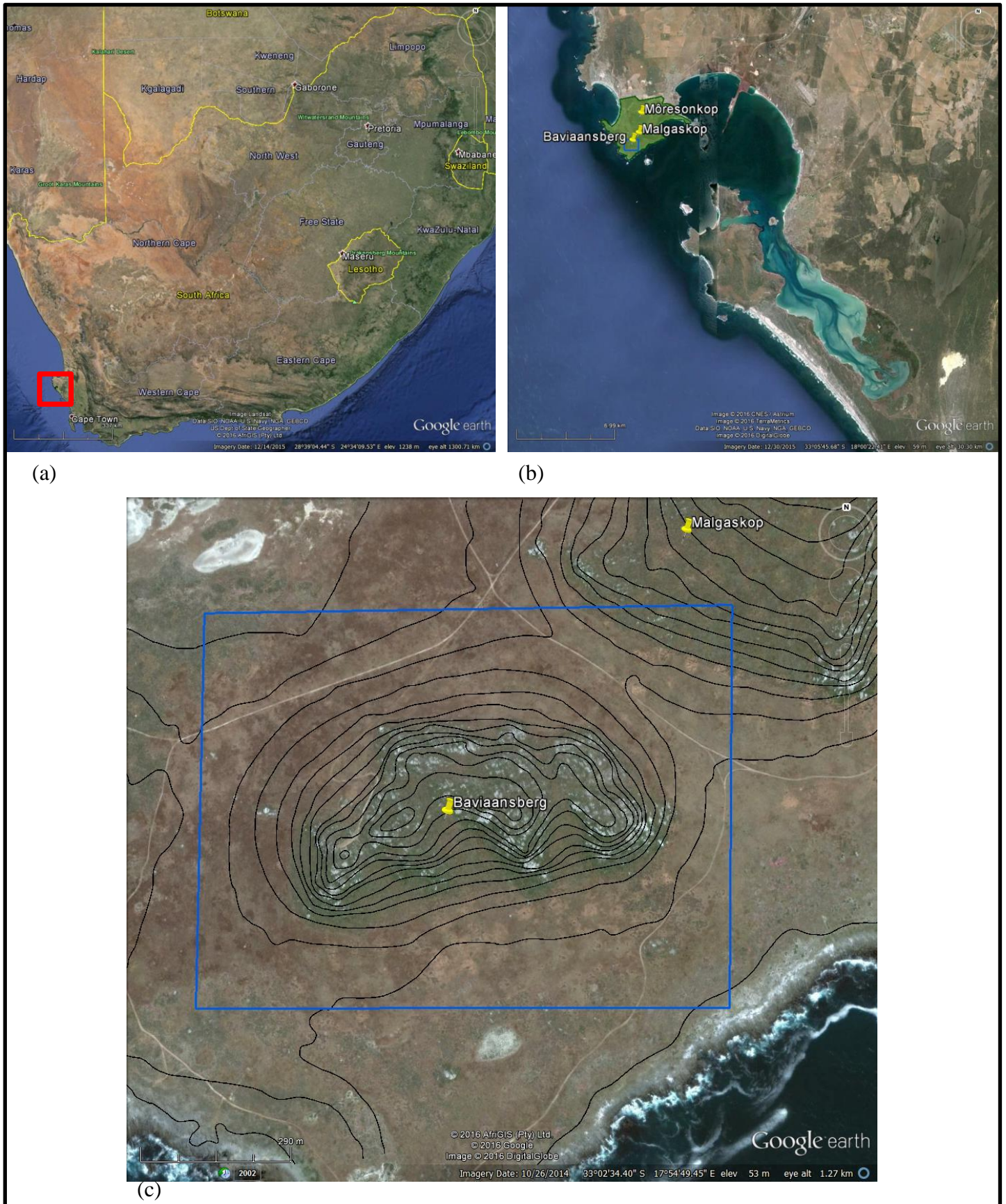
From the preceding paragraphs it is clear that γ - ray measurements are used in a variety of fields. Analyses of these maps aim at either detecting areas of high radionuclide concentrations, or the influence of one factor on the distribution patterns of natural radionuclides concentration. There is a definite scope within this area of research to study the influence of a combination of geographic factors on the distribution of natural radionuclides.

1.1.2 Research site

The West Coast of South Africa is well known for its archaeology as well as its granite hills and outcrops. The lithology of the West Coast is dominated by 600 – 650 million year old shale. Millions of years of erosion caused the overlying shale to erode, thus exposing the underlying granite. The granite outcrops are an estimated 500 million years old and forms part of the Cape Granite system (Scheepers & Armstrong 2002; Schloms 2012 Pers com).

The concentration levels of the natural radionuclides within these igneous granite outcrops are determined by the geological processes by which they were formed. In turn, these igneous granite outcrops determine the natural radiation concentration levels of the soil produced from these rocks. Igneous rocks contain relatively high concentrations of natural radionuclides which in turn contribute to similarly high levels of natural radionuclides within the soil surrounding these outcrops (Abusini et al. 2008; Tzortzis et al. 2003; Tzortzis et al. 2004). The exposed granite outcrops on the West Coast of South Africa have been exposed to weathering and erosion for the past 500 million years. This implies that the top soil within the areas surrounding the granite outcrops consists mainly of weathered granite particles. These soils should also then bear the same radiation signature as the surrounding granites.

Saldanha Bay Military Area (SMA) is situated on the West Coast of South Africa, Figure 1.1 (a). The SMA houses three granite outcrops, Malgaskop, Baviaansberg and Môresonkop, as seen in Figure 1.1 (b). These granite hills form part of the Cape Granite suite (Allsopp & Kolbe 1965; Franceschini & Compton 2004). Figure 1.1 (c) indicates the positions of Baviaansberg and Malgaskop within the research site. Baviaansberg was identified as the research site as it is uniquely situated such so that the prevailing winds are onshore with little land between the ocean and the hill. The prevailing winds are north-westerly in winter, and south-easterly in summer (Provincial Government of the Western Cape 2005; www.windfinder.com).



Source: Google Earth (2016)

Figure 1.1 (a) – (c) Google earth images indicating (a) the position of Saldanha Bay on the West Coast of South Africa, (b) the area of the Saldanha Bay Military Area indicated by the green polygon and the study area as the blue rectangle, and (c) the positions of Baviaansberg and Malgaskop in the research site.

The major phase of human activity on and around Baviaansberg occurred during the Second World War (WWII), when buildings, bomb shelters and vantage points were erected. Some farming activity also occurred post WWII. Since WWII, the SMA has mostly been reserved for military training and other military activities. Currently, there are no substantial human activities taking place in or around the area, apart from an occasional military route march. Baviaansberg has therefore been void of intense human activities for the past 40 years (Bezuidenhout 2012). However, human activity is only one of the factors playing a role in the distribution of the concentration levels of natural radiation in soil. Other geographic factors to consider are geology, topography, soil type, hydrology, and wind. All these factors will be explained in more detail in Section 2.1.

1.2 PROBLEM FORMULATION, RESEARCH AIM AND OBJECTIVES

The problem formulation is deliberated in this subsection to provide the reason for this specific research. Thereafter the aim of the research and the research objectives are provided.

1.2.1 Problem formulation

As mentioned in Section 1.1, the granites of the West Coast of South Africa were first exposed to the atmosphere about 500 million years ago after the overlying shales eroded away (Scheepers & Armstrong 2002; Schloms 2012 Pers com). Since then these granitic hills have been exposed to various geographic factors and had undergone weathering and erosion. The overlying shale also continued to erode. Baviaansberg, situated in the SMA is a granitic hill that is the result of these processes.

Because of the specific location of Baviaansberg and the prevailing wind directions there would have been little to no aeolian deposition. It is important to note that both prevailing wind directions are onshore conditions; it reaches the research site with very little land between the shore and Baviaansberg. Overlying shale would also have further eroded away, whereas weathered and eroded granite would form the 'new' overlying soil.

Aeolian deposits from distant geographic locations thus rarely occur on these outcrops. It was found that the surrounding soil immediately below the hills is mostly broken down granite (Bezuidenhout 2012). Granite is a mixture of various minerals and carries detectable natural radiation signatures of ^{40}K , ^{232}Th , and ^{238}U (Llope 2011). The detection and plotting of these natural radiation signatures provide a unique

radioelement map of the area. As mentioned in Section 1.1, there are various applications for these radioelement maps. Currently, however, there exists little literature on the information a radioelement map may provide in terms of geographic factors that can influence distribution of the concentration of natural radionuclides.

The research might provide a tool to predict high and low natural radionuclide concentrations by studying the local geographic factors of an area. It will also allow researchers to describe soil movement in an area under the influence of geographic factors by means of studying the area's natural radionuclide levels. Scientific radioelement mapping in a military area in South Africa has also only been completed by Bezuidenhout (2012). This research offered a unique opportunity to address this gap in the research by using radioelement mapping results from a military area to study the influence of geographic factors on the distribution of natural radiation concentrations.

In order to successfully complete the research the research problem needs to be addressed. The hypothesis of the research is as follows: Do local geographic factors like geology, topography, soil type, hydrology, wind and human activities influence the distribution of natural radionuclides on a small scale?

1.2.2 Research aim

The aim of the research was to measure the variations in the concentration levels of the naturally occurring radionuclides of Baviaansberg in the SMA in order to establish the feasibility of predicting the impact of various geographic factors on the distribution of the concentration of natural radionuclides. To operationalise this aim, radioelement maps were created from the measured data and the various geographic factors in the research site that plays a role in the distribution of soil, and natural radionuclide concentrations, in turn, were identified.

1.2.3 Research objectives

The research objectives provided a guideline during the planning and preparation of the research. Stated objectives were reached in the following order:

1. **Objective 1.** Complete a literature review of the available literature relevant to the research.
2. **Objective 2.** Decide on and calibrate instruments to measure naturally occurring radiation.

3. **Objective 3.** Identify and demarcate the research site for *in situ* measurements.
4. **Objective 4.** Measure naturally occurring radiation in the research site.
5. **Objective 5.** Extract concentrations of natural radionuclides of ^{40}K , ^{232}Th , and ^{238}U .
6. **Objective 6.** Create various radioelement maps, as well as various geographic maps, such as slope and accumulation rasters.
7. **Objective 7.** Perform a qualitative analysis and establish the influence of geographic factors on the spread of natural radionuclide concentrations.

1.3 RESEARCH SITE GEOLOGY

Earth's crust is composed of various rocks, which in turn are made up of various minerals. The combination of these minerals and their unique chemical and atomic structures determines the natural levels of radiation of these rocks (Marshak 2001). The research site consisted of Baviaansberg, a granitic outcrop that was exposed due to eustatic change where the surrounding shale eroded away and exposed the underlying granitic outcrops (Roberts & Brink 2002). Over the past 500 million years these granitic outcrops were weathered and eroded, distributing the soil from the weathered granite over the area and eventually creating the hills we may observe today (Scheepers & Armstrong 2002; Schloms 2012 Pers com).

The granite outcrops have undergone chemical, mechanical and biological weathering. Weathering patterns within the research site has an influence on distribution of various concentrations of the natural radionuclides. One of the reasons for variation in the concentrations of natural radionuclides is that potassium is more mobile than uranium or thorium. Potassium is the most soluble and would be transported much easier under any weathering conditions (Wilford 2002). The mobility of Thorium is considered to be extremely low (Al-Hilal & Al-Ali 2016). Uranium, on the other hand, is regarded as more soluble than thorium, thus also more mobile than thorium (Ruffel et al. 2006; Al-Hilal & Al-Ali 2016).

Erosion is the removal of soil particles from their original position (Hess 2014). The factors influencing erosion will also influence the distribution of the concentration levels of ^{40}K , ^{232}Th , and ^{238}U . It is important to determine the factors that influence the rate of erosion and weathering of the research site as these factors influence the distribution patterns of soil within the research site. These factors will then

in turn influence the distribution of the concentrations of the natural radionuclides due to the various levels of mobility of ^{40}K , ^{232}Th , and ^{238}U . Weathering and erosion as well as the geographic factors that influence the distribution of natural radionuclides will be analysed in detail under the denudation processes as explained in Sections 2.1.2 and 2.1.4.

1.4 RADIOELEMENT MAPPING

Granite is a mixture of various minerals and carries detectable signatures of ^{40}K , ^{232}Th , and ^{238}U (Llope 2011). Soil originating from granite will bear a similar radiation signature, which makes it possible to produce a unique radioelement map of the area. Radioelement concentrations of granite, or any rock or soil type, is dependent upon its mineral configuration and its origin (De Villiers 2011). Radioelement maps are derived by obtaining relevant field data via either *in situ* measurements or sampling. The measurement positions may then be identified through either random sampling, or setting minimum required data points from which a map can be drawn (Van Wijngaarden, Venema & De Meijer 2002a).

In situ measurements were the chosen method to collect data in this research for reasons stated next. *In situ* measurements are used to make detailed radioelement maps, because said measurements are sensitive to data variability attributed to the physical geography of the area (Dobos et al. 2000). One of the advantages of doing *in situ* measurements rather than taking soil samples is that it is both time and cost-effective. Rather than doing time consuming and expensive field work to take soil samples, return to the laboratory, do laboratory measurements and ultimately data analysis, everything except data analysis may be completed during *in situ* measurements. *In situ* measurements also allows for a faster assessment of radiation exposure and changes in radiation exposure (Jibiri & Farai 2005; Van Wijngaarden et al. 2002b; Li et al. 2010)

An effective technique to acquire sampling points was applied by drawing a fishnet grid over the research site using ArcGIS, as per discussion with geographer, Dr T. Flügel (2013). In so doing, a grid was created over the research site and automatically chose a sampling point in the middle of each block in the grid. The latitudes and longitudes of each point were extracted and provided an accurate position of each sampling point. Once all data were collected from each measuring point, a GIS database was created. Consequently, a radioelement map was created from field measurement data. It was important to use the correct spatial interpolation method as it influenced the accuracy of data collection and analysis, and also had an impact on the aesthetic appeal of the radioelement map (Chang 2012).

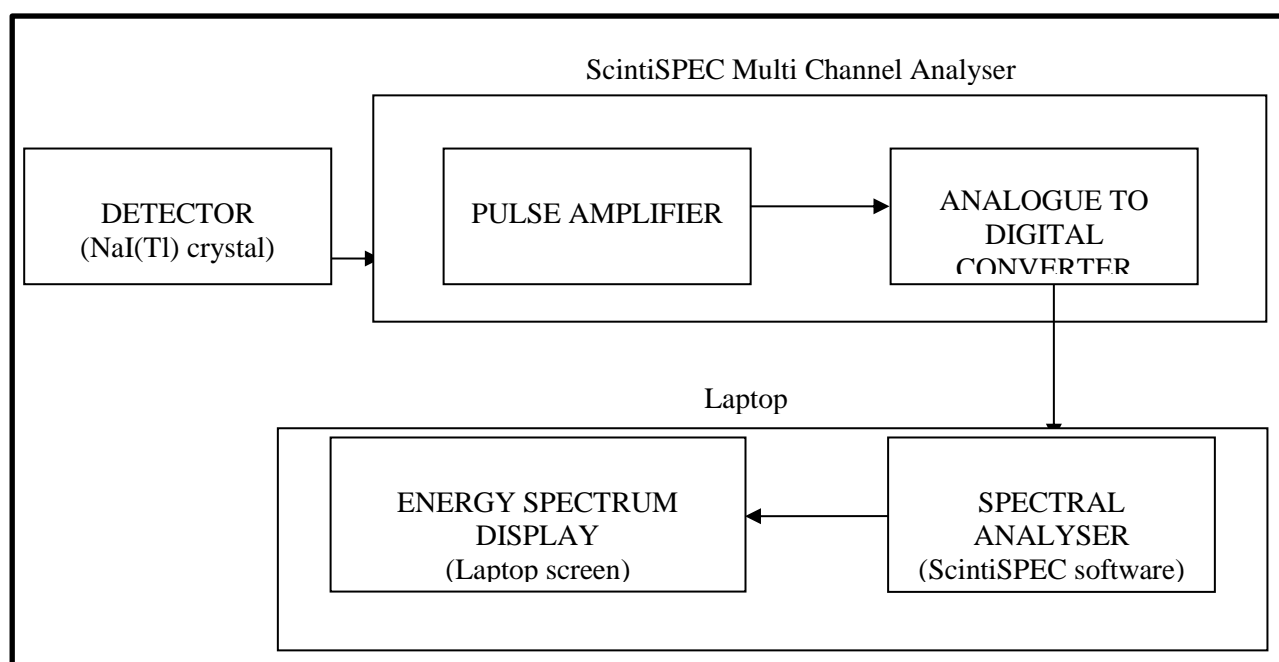
Spatial interpolation is the process through which unknown points (pixels without values) are assigned values (Chang 2012). Various interpolation methods exist, but for this research two options were tested, thin-plate splines and ordinary Kriging. Thin-plate splines generated a surface area that ran through all the measurement points. This surface area was created to have the least amount of change in slope at all points (Franke 1982). Thin plate splines are not limited to the minimum and maximum values of the measurements. Thin plate splines may, however, create overshoots (steep gradients) in data poor areas (Chang 2012). Ruffel et al. (2006) used a technique called thin-plate splines with tension (also described in Chang (2012) to allow for or correct errors in data poor areas. The result was a smoother and more accurate image. Chang (2012) recommends using thin-plate splines for surfaces such as elevation or water tables because of their smooth and continuous features. Chang (2012) also described a technique known as Kriging. Kriging is a geostatistical method for spatial interpolation. What makes Kriging unique is that it makes the assumption that spatial variation of a feature is neither totally random (stochastic), nor deterministic. It considers that spatial variation could comprise three elements: a spatially correlated element that denotes the variation of the regionalized variable (semi variance), a “drift” or structure that denotes a trend, and a random error term. The inclusion and the analysis of these elements developed Kriging into an interpolation method which is now widely used across geostatistics (Chang 2012). Both thin-plate splines and Kriging were used to create a radioelement map of Baviaansberg. The two maps were compared and the map with the best results was chosen. Section 3.2.4 provides a detailed explanation of the techniques applied.

1.5 NATURAL RADIONUCLIDE MEASUREMENT

In situ measurements were completed by using a Sodium Iodide Thallium Infused (NaI(Tl)) detector (7.62 x 7.62 cm). The NaI(Tl) crystal in the detector is a sodium iodide crystal in which thallium is added to act as the activator in order to produce an efficiency of 12% (Knoll 2000). This is ideal in the case of *in situ* measurements, as a small portable detector can be designed due to the NaI(Tl) crystal that produces a relatively large light output. NaI(Tl) is hygroscopic, i.e. very sensitive to exposure to the atmosphere and water. The NaI(Tl) crystal will deteriorate when it absorbs water. These crystals must be sealed and kept in an airtight container before use. The exceptional light yield of the crystals is one of its key characteristics. The NaI(Tl) crystal shows a small but measurable non-proportionality that is even greater at lower energies. Generally, this crystal is accepted as the standard scintillation material for gamma-ray spectroscopy (Knoll 2000). The NaI(Tl) crystal is also quite fragile and can be damaged by mechanical or thermal shock. Its decay time is 230 ns, which is relatively long for fast timing or high counting rates.

An unwanted characteristic of the crystal, at high counting rates, is the phosphorescence that builds up due to the multiple overlaps from previous pulses. It is important to note, especially with *in situ* measurements, that the NaI(Tl) crystal is sensitive to fluctuating temperatures. The scintillation yield of the crystal also decreases with the increase in operating temperatures, which results in poorer energy resolution (CSIR 2014). This problem was solved by performing pre- and post- measurement calibrations. The calibration techniques on the equipment, as well as post-calibration techniques will be clarified in detail in Sections 3.2 and 3.3. The scintillation decay time of the NaI(Tl) crystal is a function of temperature, producing a slightly faster response at higher temperatures. Another notable advantage for researchers is the fact that the crystal is relatively cheap and robust in comparison to other scintillation crystals (Knoll 2000). Alternative types of detectors are available, such as those that are Caesium Iodide Thallium Infused (CsI(Tl)), Caesium Iodide Sodium Infused (CsI(Na)) and Bismuth Germanate (BGO), each of which has its own strengths and weaknesses (Knoll 2000). However, for the purpose of this study only the NaI(Tl) detector was discussed as the detector best suited for *in situ* measurements.

A NaI(Tl) detector (7,62 x 7,62 cm) coupled to a scintiSPEC multi-channel analyser (MCA) was used to record the gamma-ray signatures of ^{40}K , ^{232}Th , and ^{238}U respectively. The scintiSPEC MCA is produced by ICX Technologies, and has a USB connection to a laptop computer through which operating voltage is obtained and signal communication is achieved (Bezuidenhout 2012). Figure 1.2 is a basic schematic representation of the detector setup.



Source: IAEA (2003: 13)

Figure 1.2 A basic block diagram of a NaI(Tl) detector (7.62 x 7.62 cm) setup.

A Full Spectrum Analysis (FSA) was completed on every recorded γ -ray spectrum of every measurement position. FSA is a method used to convert the counts in the γ spectrum to concentrations in Becquerel per kilogram. The result of FSA is that the concentrations of thorium, potassium and uranium for each measuring point were extracted (Hendriks, Limburg & de Meijer 2001; Newman et al. 2008).

1.6 RESEARCH DESIGN

The research was completed in various, sometimes overlapping, phases. The research phases are schematically portrayed in the research design in Figure 1.3.

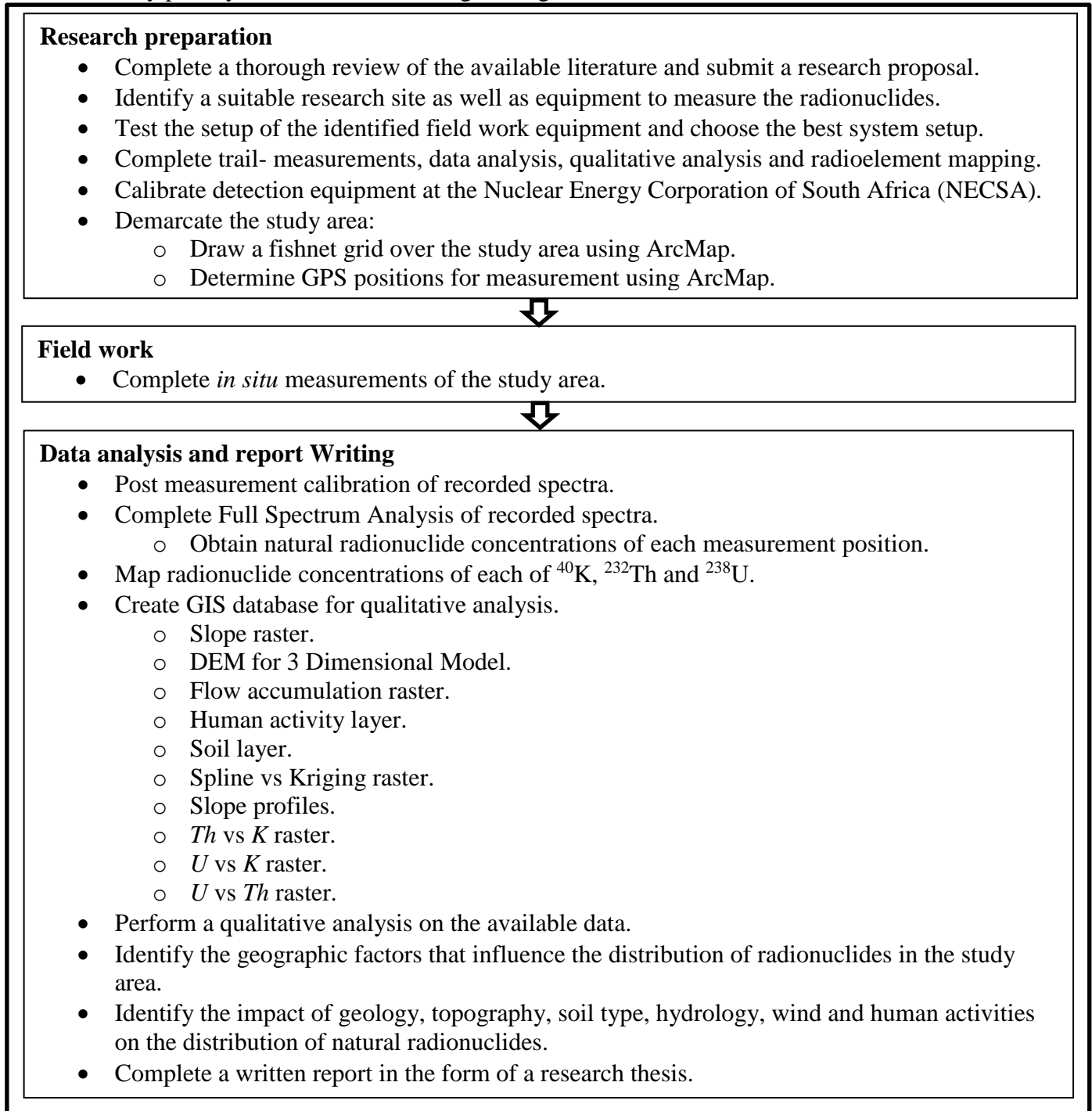


Figure 1.3 A Schematic representation of the research design.

1.7 THESIS OUTLINE

This first chapter comprises an introduction to the research and provides an overview of the research process as well as the theoretical and thought processes that guided the entire research project.

Chapter 2 is an in-depth explanation of the theoretical background upon which the research is built. It clarifies the denudation process involved in forming and distributing soil and in turn distributing natural radionuclides. The geographic factors influencing the distribution of natural radionuclides will also be identified and explained. Chapter 2 will also relay in detail natural radiation in the geological environment as well as the general properties of radiation.

Chapter 3 provides a description of the geographic terrain of the research site. It also explains the methodology of the research in terms of the equipment used, GIS methods used, data collection, radiation data analysis and qualitative data analysis.

In Chapter 4 the results of the research will be deliberated. The chapter will commence by discussing the natural radionuclide concentrations found on Baviaansberg. Thereafter the relationship between the natural radionuclide concentrations and the physical and human geographic factors within the research site will be explained.

Chapter 5 concludes the research report by providing a review of the research process. It will summarise the research results and conclusions, and provide theoretical and practical implications and applications of the research. Chapter 5 will also deliberate the limitation of the research and possible improvements of the research. Finally, it will identify unanswered questions and new directions for further research.

CHAPTER 2: DENUDATION PROCESSES IN THE PHYSICAL ENVIRONMENT AND NATURAL RADIATION

The processes of denudation in the physical environment will be the opening theme of Chapter 2. Natural radiation in the physical environment will then be discussed, followed by an overview of the properties of radiation. The chapter will conclude with a brief summary of the salient issues elaborated upon in the chapter.

2.1 DENUDATION IN THE PHYSICAL ENVIRONMENT

This section will commence with a general discussion on the geology of the physical environment. Thereafter the processes of denudation on the physical environment will be deliberated in the following order: weathering, mass wasting and erosion. The section will conclude with factors that influence denudation.

2.1.1 Geology of the physical environment

Earth's crust contains approximately 100 natural chemical elements, classified as either major elements or trace elements (Hess 2014). These elements combine to form minerals. Minerals, according to Marshak (2001), are homogenous, solid inorganic materials, formed by natural processes, with a definite chemical configuration of atoms, ions, or molecules arranged in a specific pattern to form a crystal lattice. Minerals are considered the foundation of rock formation. Most rocks, such as granite, consist of a combination of minerals. However, there are some that consist of only one mineral, for example, diamonds (Sorrel & Sandstorm 1982; Ahnert 1996). Natural radionuclides form part of the mineral composition of rocks. The combination of these natural radionuclides within each mineral produces a unique radiation signature that can be associated with a specific rock or soil type and can also be related to the process of rock formation (Sharma 1997).

According to Monkhouse & Small (1978), rocks are a composition of mineral matter which can be categorized according to the manner in which they are formed. Rocks are classified into three main groups: igneous, sedimentary and metamorphic. The formation and breaking down of these rocks occur via internal and external geomorphic processes and plays an integral part in the process of shaping Earth's

surface. The rock cycle embraces both the processes of breaking up and forming rocks in a continuous cycle (Ahnert 1996; Wilson 2010). Folding, faulting, plate tectonics and volcanism are the internal processes of the rock cycle that build Earth's surface, whereas the processes that cause Earth's surface to break down are weathering, mass wasting and erosion. The processes responsible for breaking down the earth's surface are jointly called denudation (Strahler & Strahler 1992; Phillips 2005). Denudation is the primary process in hill and soil formation through which 'softer' overlying rock erodes away, forms soil, and exposes more rigid and less erosive underlying rocks, and over time, forms big hills and even mountains (Schloms 2012 Pers com).

The process of soil formation commences at the breakdown, whether physical or chemical disintegration, of rock. These rocks are also referred to as the parent material of soil (Beamish 2014). The process of soil formation is initiated once parent material is exposed to water, air and biological factors. These factors cause the parent material to disintegrate. This physical or chemical disintegration of rock is known as weathering and is the first step in the process of denudation, followed by mass wasting and erosion (Moses, Robinson & Barlow 2014)).

2.1.2 Weathering

Weathering is the chemical or physical disintegration of rock into smaller units by means of biotic and atmospheric factors and are classified as mechanical, chemical and biological weathering (Monkhouse & Small 1978; Moses, Robinson & Barlow 2014). According to Hess (2014), the end result of weathering are boulders, cobbles, pebbles, granules, sand, silt, and dust.

Mechanical weathering is the breaking down of parent material due to various types of stresses into smaller pieces without changing its chemical composition. Most mechanical weathering occurs at or near the surface of the earth, however some mechanical weathering can occur deep below the earth's surface (Hess 2014).

Chemical weathering is where the chemical composition of the parent material is altered during the disintegration process. The rate of chemical weathering increases with the increase of the surface area that is exposed to the atmosphere as moisture in the atmosphere is an important component for chemical weathering to occur. Temperature is another contributing factor that influences the rate of chemical

weathering. An increase in both temperature and moisture increases the rate of chemical weathering, and vice versa (Briggs & Smithson 1985).

Biological weathering occurs due to the presence of plant and animal life. Plant life have the greater influence where biological weathering is concerned. Plants weaken the parent material mechanically when plant roots grow into cavities and mechanically weather rocks as these roots lengthen and expand. Lichens grow on bare rock and weaken the rock as they expand and contract, causing small fragments of rock to break off. Chemically, lichens extract minerals from their hosts through ion exchange. This form of chemical weathering weakens the parent material (Briggs & Smithson 1985; Hess 2014).

Regolith is the term used for various particles of various sizes that are broken off from the parent material during weathering. Generally, the larger pieces of regolith are closer to the parent material than the smaller ones. The smaller particles are easier transportable away from the parent material, and also more easily influenced by chemical and biological weathering (Turkington, Phillips & Campbell 2005).

Various factors influence the type and rate of weathering. The atmosphere contributes the bulk of factors responsible for weathering. As a gas, the atmosphere will be able to penetrate the smallest of openings. Oxygen, carbon dioxide and water vapour are the chief atmospheric components responsible for weathering. Changes in temperature, water, and living organisms, collectively termed biotic factors, are also important weathering factors. All these factors, together with physical properties of the parent material are involved in an integrated web to institute either mechanical, chemical or biotic weathering of rock (Marshak 2001).

2.1.3 Mass wasting

The downslope movement of weathered material effected by gravity is called mass wasting. Soil, as a by-product of weathering, is subject to such gravity induced movement. The very slow movement of soil down the slope of a hill is called soil creep. Once water is added to the weathered soil and regolith it becomes saturated and is prone to flow downhill. Said flow is faster than soil creep. Landslides occur on steeper slopes with or without the addition of water. However, water does make weathered soil and regolith more prone to landslides. Land falls occur on very steep slopes or scarps when loose regolith undergoes gravity-induced free fall (De Blij 1980; Hess 2014). Mass wasting provides a form of

transportation of weathered material from the parent material. It then also provides a method of removing natural radionuclides from the parent material.

2.1.4 Erosion

During the first step in the three-step process of denudation, erosion is the process that removes the weathered material from the source area. Erosion also provides the means for natural radionuclides to be transported away from the parent material. Erosion is either a wind driven, aeolian, or water driven, fluvial process. Human activities can enhance the rate of erosion (Briggs & Smithson 1985).

Fluvial erosion is the dominant erosive force and occurs in two main processes: unchannelled overland flow and channelled (stream) flow along valleys and gullies. Channelled flow occurs within the boundaries of a drainage divide and ends in a drainage basin where deposition of the eroded material takes place. Fluvial erosion occurs with the first fall of a rain drop where soil is transported laterally by the force of the falling raindrop. Thereafter, more raindrops cause more erosion. Erosion will further increase as water starts to flow overland - the stronger the flow of water, the heavier the particles transported. The heavier particles will also be the first to be deposited once water flow loses its force. Smaller particles will be transported a greater distance from parent material with particles in solution being transported furthest. Particles in solution will be deposited once water is stationary and has evaporated. This is called dissolution. The particles in solution may also enter the soil through drainage, depending on the depth of the drainage. Water flowing downward through soil may also drain the soil of soluble minerals and elements. The amount of erosion is dependent on the vegetation cover, slope of the terrain, soil type, geology, and the rainfall amount and intensity of an area (Strahler & Strahler 1992; Hess 2014).

Aeolian erosion is caused by the flow of air over terrain. The effect of this flow of air is similar to that of water flowing over the same terrain, but with less effect (Hess 2014). Thus aeolian erosion follows the same processes as fluvial erosion, but on a much smaller scale. Aeolian erosion also has a significantly smaller impact on landscape development. However, over time the impact of aeolian erosion becomes more prevalent in the formation of landscapes. The impact of aeolian erosion is significantly reduced in terrain with greater vegetation cover. Therefore, aeolian erosion is more prevalent in arid and desert landscapes (Strahler & Strahler 1992).

Deposition is the final act of erosion (Briggs & Smithson 1985). The amount of deposition that occurs is dependent on the type of erosion. Fluvial erosion is responsible for removing the most particles from the parent material, whereas aeolian erosion can distribute small particles over large surface areas.

2.1.5 Factors influencing denudation

Soil can be seen as the ‘final product’ in denudation. There are various factors that influence denudation and, in turn, soil development and movement. The factors to consider are geology, climate, topography, biology, time and human impact (Ahnert 1996).

Geology of the research site will be discussed in terms of rock type and landform. The composition of the parent material determines its strength and its resistance to weathering and erosion. The parent material also influences mineral composition, natural radiation signature of the eroded material as well as soil type. This will be further explained in Section 2.2 of this chapter. Types of landform contribute to the rate at which parent material will weather. A hill, for example, will undergo more weathering than an alluvial plain (McLennan 1993; Turkington, Phillips & Campbell 2005).

Climate of an area consists of the meteorological factors: temperature, wind, atmospheric moisture, precipitation, sunshine, cloudiness and atmospheric pressure. Two of these meteorological factors influence denudation rate. Should either temperature or moisture, or both, increase, so too will the effect and amount of chemical and biological processes contributing towards denudation. Drainage that drains soil of soluble minerals and elements may also change the chemical and physical properties of the soil (Ruxton & Berry 1957; Briggs & Smithson 1985).

Topography of the terrain is a defining factor in the denudation rate of an area. Topography is defined as the description of the outline of the surface area of the earth at that specific place; it includes factors such as drainage patterns, slope, elevation and relief (Briggs & Smithson 1985; Hess 2014). According to Ahnert (1996), Earth’s surface consists of areas of interconnecting slopes where the movement of weathered matter under the influence of gravity is a function of slope angle. Strahler & Strahler (1992) argues that the rate of denudation is strongly influenced by the gradients of hill slopes - the higher the gradient and the relief of a specific area, the higher the rate of denudation for that area will be. Areas of steep slopes also lend itself to greater changes in the physical and chemical properties of the terrain. This argument is supported by Ruxton & Berry (1957), Phillips (2005), and Von Blanckenburg (2005).

Because flowing water will follow the path of least resistance, it follows the streams and valleys of an area and ends up in a drainage basin. The rate of the flowing water will change with the change of relief of an area. This means the physical and chemical characteristics of streams, valleys, valley sides and drainage basins can considerably differ from one another in the same drainage area (Hess 2014). Williams and Robinson (2000) have also shown that aspect plays a role in the rate of weathering and denudation because certain slopes are exposed to prevailing meteorological conditions more than other slopes of the same area.

The biology of an area, including plants, animals and microorganisms, plays a significant role in the rate of denudation and soil formation. Burrowing animals increases the amount of air and water supply to soil. It also turns up the soil by bringing soil from the bottom layers to the surface, and *vice versa*. Lichens grow on rocks and extract minerals from rock that contributes to mechanical and chemical weathering. Decaying plants and animals also contribute to the fertilisation of soil that, in turn, changes the physical and chemical properties of soil. Larger animals will also influence the rate of denudation and soil formation. The greater the number of animals present in an area, the more the vegetation will get trampled, thus exposing soil and increasing denudation. Droppings of larger animals will also change the mineral composition of soil. The change in the mineral composition of soil is directly related to the number of animals present in an area. Vegetation cover is another contributing factor that either increases or decreases denudation and soil formation rates. An area with the exact same topography but with different vegetation cover will yield a completely different rate of denudation and soil formation. In general, the rate of denudation and vegetation cover is inversely proportional to one another with the rate of denudation decreasing with an increase in vegetation cover (Etienne 2002; Welch & McPhail, 2003; Hall et al. 2005). The biological impact on the research site is considered to be standardised. In other words, the impact thereof is the same across the area and will hence not be discussed as one of the geographic factors that influence the distribution of natural radionuclides.

Denudation is a **time** consuming process, and the rate of denudation is highly dependable on the nature of the parent material, the amount of parent material exposed to the elements as well as the characteristics of the environment (Hess 2014).

Humans have a certain impact on any environment. Denudation is not exempted from said impact. Human activities such as agriculture and urbanisation will either increase or decrease the rate of denudation (Woo & Luk 1990; Syvitski et al. 2005; Harden 2006).

Denudation mainly influences the rate of soil formation. The mineral composition of the soil formed and the natural radiation signature of that soil are highly dependent on the type of parent material. Natural radionuclides are part of the mineral composition of parent material. Natural radionuclides are distributed over a specified area during denudation. These natural radionuclides are responsible for producing natural radiation.

2.2 GEOLOGY AND NATURAL RADIATION

Natural radiation in terms of this research is defined as radiation emitted from the natural radionuclides ^{40}K , ^{232}Th , and ^{238}U . These elements are present in most rock types either as major elements or as trace elements. Baviaansberg in the research site is made up of granite only. Granite is an igneous rock type with a naturally high concentration of natural radionuclides as part of its mineral composition. This section will explain natural radiation in terms of its presence in igneous rocks, granite and soil. The section will conclude with a discussion on natural radionuclides and their decay series.

2.2.1 Igneous rocks

Igneous rocks form when magma or lava is cooled down enough to harden and form rock. The main difference between rocks formed from lava and magma is that rocks formed from lava contain less mineral components than rocks formed from magma. The reason for this difference is that magma contains gaseous components that become part of the rock once it solidifies, whereas lava's gaseous components are released as soon as it comes into contact with the atmosphere (Ahnert 1996). Igneous rocks are classified according to their mineral composition and texture. That implies that the main factors influencing the type of igneous rock are chemical composition of the lava/magma and rate of cooling. (De Blij 1980; Marshak 2001). The amounts of silicate minerals present in the chemical composition of igneous rocks are the main determinant of the type of igneous rock. There are two main groups of silicate minerals, namely, felsic and mafic minerals. Felsic minerals consist of quartz and feldspars, while mafic minerals consist of silicates abundant in magnesium and iron. The texture of igneous rocks is directly related to at which rate and where molten rock solidifies. Coarse grained rocks are formed when magma cools down slowly deep beneath Earth's surface, whereas finer grained rocks are formed when magma cools down fast near the surface of the earth, or flows out on the surface as lava. Igneous rocks that are formed when lava is cooled down on the surface of the earth are classified as volcanic or extrusive, while rocks formed when magma is cooled down below the surface of the earth are called plutonic or intrusive.

Rocks such as granite and diorite are classified as intrusive, whereas rhyolite and andesite are classified as extrusive. Granite and rhyolite have the same mineral composition, but their crystalline structure differs. Both granite and rhyolite are classified as felsic, whereas rocks such as gabbro and basalt are mafic (Strahler & Strahler 1992).

2.2.2 Granite

Granite is probably the most prominent and widespread igneous rock and has a formal classification as a felsic intrusive igneous rock. This rock type dominates the research site. Its mineral composition consists mainly of a combination of the various silicates $K(Mg,Ge)_3AlSi_3O_{10}(OH)_2$, $KAl_2(AlSi_3O_{10})(OH)_2$, and $KAlSi_3O_8$, with potassium (*K*) as a major material in the element composition of granite (Welch & McPhail 2003). Granite also contains various trace elements, including Thorium (*Th*) and Uranium (*U*), which do not form part of the mineral composition of the major silicates (Kostitsyn et al. 2007; Villaros et al. 2009). The various combinations of major and trace elements divide granite into different classes. Frost et al. (2001) produced a number of classification methods for granite. The International Union of Geological Sciences (IUGS) classification method is centred on the modal richness of quartz, plagioclase and alkali feldspar (Le Bas & Streckeisen 1991). The classification used most often is the alphabetic classification, first used by Chappel & White (1974) who documented two different types of granite in the Lachlan Fold Belt in eastern Australia. The one type of granite was a metaluminous to a weaker peraluminous type. It was fairly sodic and had a wide range of silica content, 56-77 wt % SiO_2 . It was argued that it was formed from a mafic, metaigneous source and was called the I-type granite. Another type, S-type granite, was also identified. This type of granite was overwhelmingly peraluminous, moderately potassic and contained limited to higher concentrations of silica compositions, 64-77 wt % SiO_2 . Loiselle and Wones (1979) identified an A-type granite because of its alkalinity, anhydrous characteristics and supposed anorogenic tectonic setting. White (1979) identified a type of granite that supposedly rises from the mantle, which was named M-type granite. Kilpatrick & Ellis (1992) also defined a C-type granite that is a definite charnockitic magma type. The magnetite- and ilmenite-series granitic rocks were defined and classified by Ishihara (1977). Barbarin (1999) classified granite rocks according to their silicate mineralogy, and suggested that granite rocks can be classified according to the mineralogy of granites and the relationship between the granite and its aluminium saturation. De la Roche et al. (1980) characterized igneous rocks by means of the variables R_1 and R_2 discrimination diagrams. This method uses the basalt tetrahedron of granite and after a series of processes classifies granite rock into two dimensions that are classed into two separate cationic functions R_1 and R_2 . Pearce, Harris and

Tindle (1984) used the geochemical characteristics of granite to classify the tectonic environment of these rocks, and classified granite into trace element discrimination diagrams. Based on the alphabetic classification by Chappel & White (1974), the granite hill in the research site, Baviaansberg, is classified as S-type granite, according to Scheepers (1995).

2.2.3 Soil

The denudation processes in the research site produces soil formed mainly from granite outcrops. Granite has a unique gamma radiation signature because of the presence of ^{40}K , ^{238}U and ^{232}Th in its mineral composition (Frost et al. 2001). This soil will bear the same concentration of ^{40}K , ^{238}U and ^{232}Th as these granite outcrops (Bezuidenhout 2012). Each type of soil is closely related to the parent material, but the longer the soil is influenced by factors such as geology, climate, topography, biology, time and human impact (Ahnert 1996), the more the mineral signature, and in turn the radiation signature, will differ from the parent material. This variation in the concentrations of the natural radionuclides present in soil can be measured. Through using the data on the variation in the concentrations of the natural radionuclides, a radioelement map can be reproduced. The extent of the impact of the various geographic factors can thus be inferred by plotting the variation in the radioelement signature of the soil of a specific area.

2.2.4 Natural radionuclides and their decay series

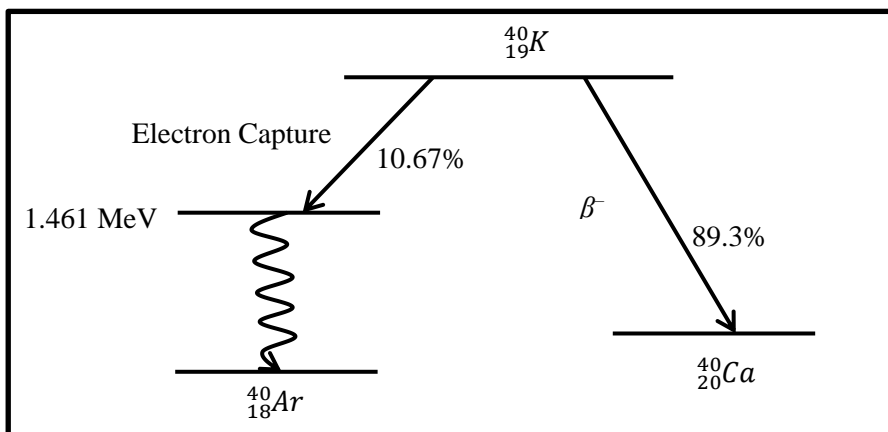
Natural occurring potassium consists of the radionuclides potassium 39 (^{39}K) at 93.26%, ^{40}K at 0.0117%, and potassium 41 (^{41}K) at 6.73%. Of these radionuclides only ^{40}K is radioactive. Gamma radiation is easily detectable, and by measuring the concentrations of ^{40}K it is possible to determine the total amount of potassium present. Naturally occurring thorium consists of 100% ^{232}Th which is radioactive and can be measured via γ - ray photon emissions from their daughter nuclides. Naturally occurring uranium consists of 0.0054% uranium 234 (^{234}U), 0.72% uranium 235 (^{235}U) and 99.27% ^{238}U . The ^{238}U radionuclide decays through various gamma emitting daughter nuclides that is measurable (Böhlke et al. 2005). γ - ray photon detection will be the mode of detection during this research. The fundamentals of radioactivity, γ - ray photon interaction and detection will be discussed in detail in Section 2.3.

All radionuclides decay over time. It is a process that occurs naturally and produces various forms of radiation, including γ - ray photons. The natural radionuclides have half-lives of 1.3×10^9 years from ^{40}K , 4.46×10^9 years from ^{238}U and 1.39×10^{10} years from ^{232}Th (IAEA 2003). Concentrations of natural

radionuclides are strongly dependent on the geology and geography of the area (Tzortzis et al. 2003). The top 30cm of soil of any area is responsible for the radiation signature of above ground level radiation measurement (Lahham, Hussein & Judeh 2009; Beamish 2013).

Secular equilibrium might occur in a decay series. Secular equilibrium occurs when decaying atoms of daughter radionuclides are the same as that of their parent radionuclide throughout the entire decay chain (Sharma 1997). Secular equilibrium in a series can be broken in cases where leaching of radionuclides can occur or can be broken due to the escape of radon gas. The research site is relatively undisturbed, so it can be assumed that secular equilibrium occurs in all the decay chains of ^{238}U and ^{232}Th .

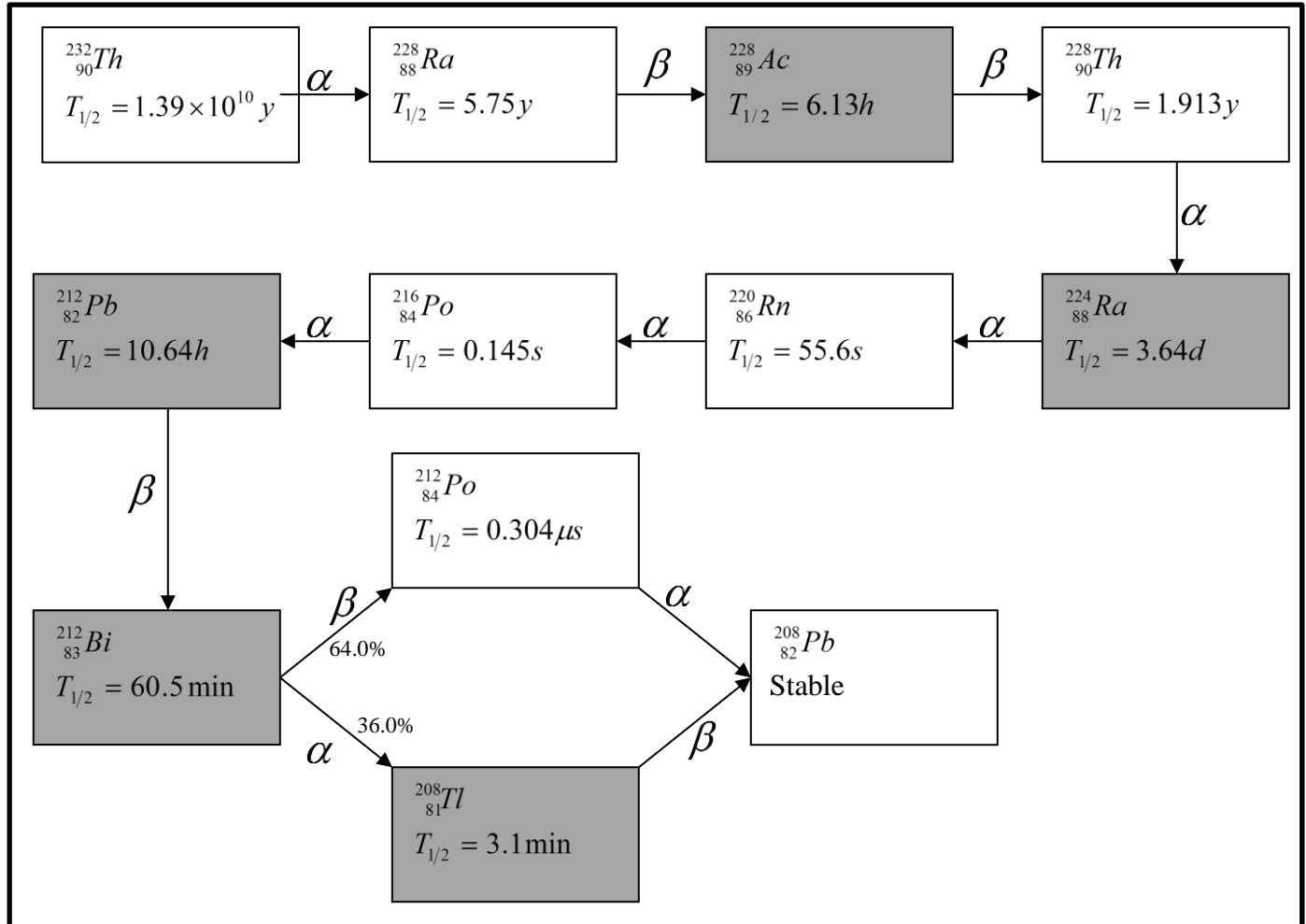
The three natural radionuclides and their daughters emit measurable gamma radiation that is ideal for *in situ* measurements (Sharma 1997; Hendriks 2003). The decay series of ^{232}Th and ^{238}U differs quite significantly from ^{40}K . The modes of decay will be discussed in detail in the following section. ^{40}K decays via β^- decay to a stable ^{40}Ca as well as, via electron capture, to ^{40}Ar that is in an excited state. The excited ^{40}Ar then de-excites to a stable ^{40}Ar through the discharge of a 1.461 MeV gamma-ray. Figure 2.1 indicates the natural decay series of ^{40}K . The majority, 89.3%, of ^{40}K decays via β^- decay to calcium 40 (^{40}Ca). Only 10.67% of the ^{40}K radionuclide decays via electron capture to argon (^{40}Ar) and produces a γ - ray photon with an energy of 1.461 MeV (Hendriks 2003; Maphoto 2004).



Source: Hendriks (2003: 16)

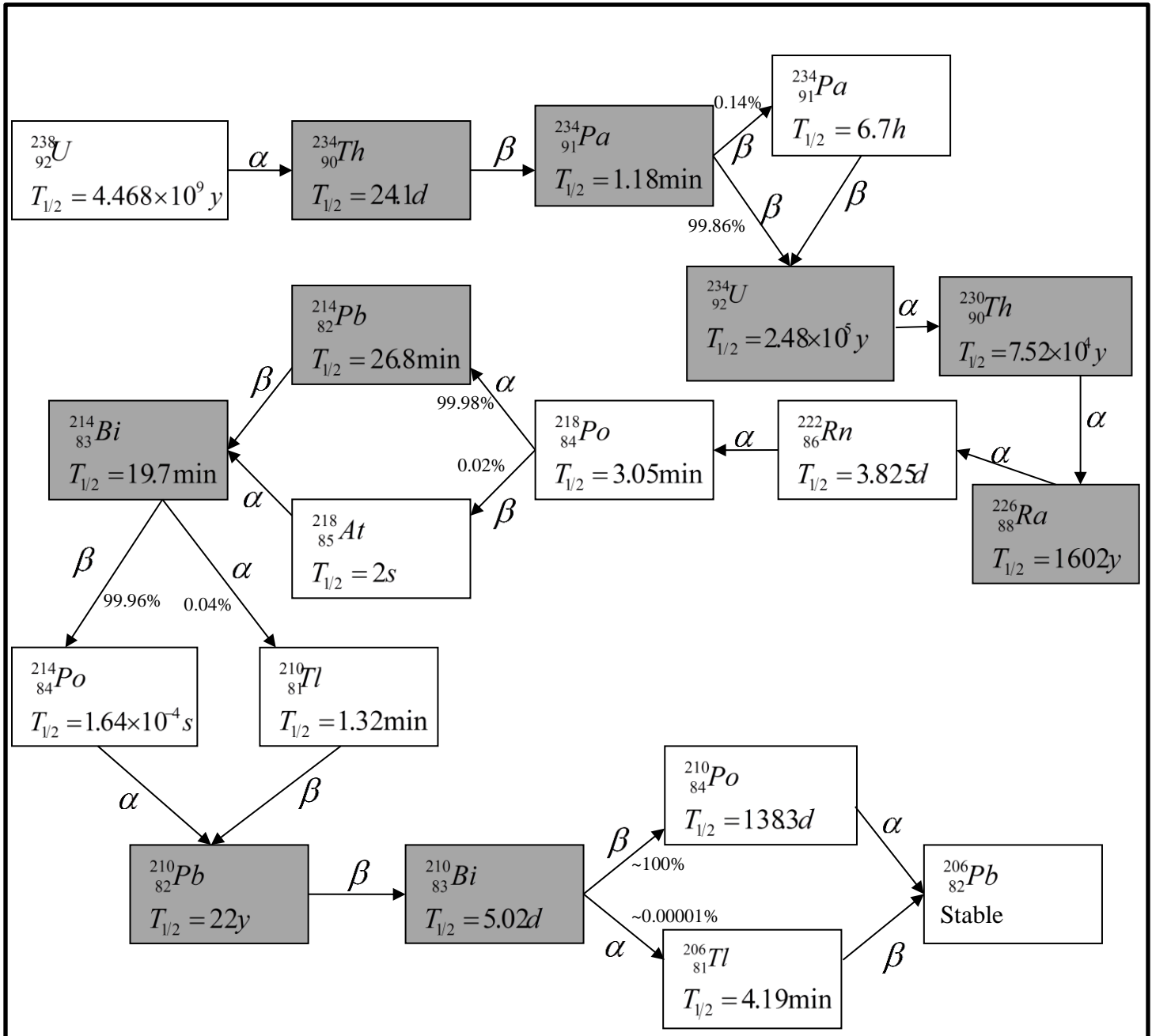
Figure 2.1 ^{40}K decay chain indicating the decays to ^{40}Ca and ^{40}Ar respectively.

^{232}Th and ^{238}U have various alpha (α) and beta (β) decays in their respective chains. Each step in the chains do not, however, decay via γ - ray photons. Only the steps indicated in grey in Figures 2.2 and 2.3 produce a γ - ray photon with unique detectable energies (Sharma 1997; Hendriks 2003).



IAEA (2003:17); Source: De Villiers (2011: 32)

Figure 2.2 ^{232}Th decay series. The grey blocks indicate the gamma emitting nuclides, $T_{1/2}$ indicates the half-life of each daughter, and α and β indicates the mode of decay.



Hendriks (2003: 17); Source: Attix (2004: 113)

Figure 2.3 ^{238}U decay series. The grey blocks indicate the gamma emitting nuclides, $T_{1/2}$ indicates the half-life of each daughter, and α and β indicates the mode of decay.

^{232}Th decays through 10 daughters to a stable ^{208}Pb nuclide, the decay series is demonstrated in the diagram in Figure 2.2. ^{238}U decays in 16 steps to a stable ^{206}Pb nuclide, the decay series is demonstrated in the diagram in Figure 2.3 (IAEA, 2003). When the measurement of the concentration of ^{238}U is

referred to in this thesis, this implies the measurement of the daughters in the ^{238}U series that give off gamma rays. This may differ from the ^{238}U concentration as discussed in this section.

2.3 PROPERTIES OF RADIATION

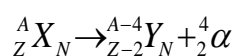
Section 2.3 constitute a discussion of the properties of radiation. The discussion will commence with an explanation of the fundamentals of radioactivity. It will also discuss γ - ray photon interaction with matter and will conclude with an explanation of γ - ray photon detection.

2.3.1 Fundamentals of radioactivity

Atoms of all radionuclides comprise of a nucleus that is surrounded by electrons; the nucleus, in turn, consists of protons and neutrons. The sum of the protons and neutrons is the mass number A , whereas Z is the atomic number and denotes the number of protons. Atoms that have the same atomic number but different mass numbers are referred to as isotopes of a specific element. On the other hand, atoms that have the same number of protons are called nuclides. These nuclides or isotopes are denoted as A_ZN , where N is the specific element (IAEA 2003).

Radioactivity, according to Sharma (1997), is the disintegration of the nucleus of an atom by the discharge of energy through particles or radiation. Some nuclides possess excess energy, charge or mass and this causes it to be unstable. This energy, charge, or mass is generally released through the process of radioactive decay. Radioactive decay is associated with four different methods of decay: alpha decay, beta decay, gamma radiation, and electron capture (Hendriks 2003; IAEA 2003):

Alpha (α) decay. When a nuclide undergoes α decay, it releases an α particle (${}^4_2\text{He}$) that comprises of two protons and two neutrons. The decay process is expressed as:



where X and Y are the parent and daughter nuclides respectively, and α is the alpha particle.

Beta (β) decay. Two types of β decay take place, β -minus (β^-) and β -plus β^+ decay. β^+ decay is associated with the release of a positively charged positron (β^+ particle) and is less common than β^- decay. β^- decay occurs more frequently and is associated with the release of a beta particle that is identical to a negatively charged electron. β^+ decay is expressed as:



where X and Y represent the parent and daughter nuclides, β^\mp represents either an electron or positron particle and $\bar{\nu}$ is an antineutrino. The neutrino or antineutrino, according to Knoll (2000), does not have a great interaction probability with matter and for all practical purposes can be ignored. Both α and β particles do not have great penetrating capability and that causes it to be absorbed relatively quickly by materials in close proximity to the radiation source (Sharma 1997; Hendriks 2003).

Gamma (γ) radiation. The nucleus of an atom may be left in an excited state following α or β decay. The excited nucleus will then de-excite by discharging the excess energy as electromagnetic radiation in the gamma region of the spectrum. Gamma radiation measurement is ideal for *in situ* measurements due to its great penetrating capability and the distinct energies of the γ - ray photons that a specific nuclide emits.

Electron capture is another process that occurs when an orbital electron is absorbed by the nucleus of an atom. A proton in the nucleus is now converted to a neutron, and the electron is then replaced with the emission of a characteristic radiation signature associated with the atom (Hendriks 2003; IAEA 2003).

Radioactive decay continues until the nuclei reaches a stable nuclide. The number of radioactive nuclides for an isotope or nuclide is expressed by the radioactivity decay law (IAEA 2003):

$$N_t = N_0 e^{-\lambda t} \quad (2.1)$$

where N_t is the number of atoms present after time t (s), N_0 is the number of atoms present at time $t = 0$, and λ is the decay constant of a radionuclide (s^{-1}). The half-life, $T_{1/2}$ in seconds (s), of a nuclide is the time taken for half of the radionuclides to decay and is expressed as:

$$T_{1/2} = \frac{0.693}{\lambda} \quad (2.2)$$

The product λN gives the activity of the radionuclide measured in Becquerel (Bq). Becquerel is the unit of measurement of radioactivity where one Bq is equal to one nucleus decaying per second, and is independent of any other physical factor (Knoll 2000).

Radioactive decay causes the number of unstable nuclei N to reduce in a time (t). The activity R of a nuclide is the number of decaying nuclei per unit of time. Following from equations 2.1 and 2.2 it can be expressed as (Hendriks 2003; Maphoto 2004):

$$R \equiv -\frac{dN}{dt} = \lambda N \quad (2.3)$$

The nuclides that form after the specific decay process takes place are referred to as the daughters of the parent nuclide. These daughters could also be unstable and would consequently undergo further radioactive decay, which will continue until a stable nuclide is reached. This chain of consecutive radioactive decay is called a decay series. According to Sharma (1997), the daughter products of nuclides are in equilibrium with its parent nuclide when the number of daughter atoms, N_i , that disintegrate per second is the same as the number that is formed by the disintegration of the parent atom. Radioactive equilibrium is expressed as

$$\lambda_1 N_1 = \lambda_2 N_2 = \lambda_3 N_3 = \dots = \lambda_i N_i \quad (2.4)$$

where λ_i is the decay constant of the i^{th} radionuclide and N_i is the number of atoms in the disintegration of the i^{th} nuclide in the decay series (Sharma 1997; IAEA 2003).

2.3.2 Statistical behavior of radioactive decay

The decay of all radioactive material is a stochastic process. Every single decay event in a decay chain occurs independently from any other decay event. The time intervals between decays are also completely

independent from one another. The decay process, which is the probability that the number of nuclei (n) will decay within a unit of time, can be modelled by a Poisson distribution. A modified Poisson distribution is used in radioactive decay because the success probability, p , is small and constant. This implies that the observation time is smaller than the half-life of the radiation source, which in turn implies the number of radioactive nuclei remains constant during the process of observation. Consequently, the probability to detect a decay event from a specific nucleus is small (Knoll 2000; Hendriks 2003). According to the IAEA (2003,) the Poisson distribution for radioactive decay is expressed as:

$$P(n) = \frac{\bar{n}^n}{n!} \exp(-\bar{n}) \quad (2.5)$$

The equation states that P is the probability that the number of nuclei (n) will decay within a unit of time, if \bar{n} is the mean decay rate. The variance σ^2 must be equal to the mean value of the distribution for a process to be classified as a Poisson distribution. Poisson distribution is also used to describe the frequency of disintegration of the huge number of random atoms that undergo radioactive decay. During radioactive decay the discharge of particles and γ - ray photons is proportional to the quantity of disintegrating atoms. The standard deviation is then used to determine the range of deviations and errors of radiation measurements because the particles and gammas freed in the decay chain are proportional to the amount of decaying atoms. The standard deviation is expressed as (Knoll 2000; Hendriks 2003; IAEA 2003):

$$\sigma(N) = \sqrt{N} \quad (2.6)$$

\bar{N} is the mathematical expectation of the number of counts. The error in the measurement of N (fractional standard deviation of count) is expressed as:

$$\frac{\sigma(N)}{N} = \frac{1}{\sqrt{N}} \quad (2.7)$$

Then, for a count rate of $n = N/t$, the standard deviation is:

$$\sigma(n) = \frac{\sqrt{N}}{t} = \sqrt{\frac{n}{t}} \quad (2.8)$$

and the fractional standard deviation of the count rate n is:

$$\frac{\sigma(n)}{n} = \frac{1}{\sqrt{nt}} \quad (2.9)$$

The probable deviation ($P = 0.5$) is a multiple of standard deviation and is expressed as 0.674σ . The accuracy of measurements can be increased when equations 2.7 and 2.9 are analysed. Accuracy is improved by increasing the counts (N) measured by using equipment that is more sensitive to gamma radiation detection, in other words, to detect more events in the same space of time. An increase in count rate (n) will also improve the accuracy. This can be obtained by improving the geometry of the measurement. The measurement time also plays a vital role in accurate measurements. Increasing the time of measurement will allow more events to be recorded, which in turn increases the accuracy of the measurements (Knoll 2000; Hendriks 2003; IAEA 2003).

2.3.3 Gamma- ray photon interaction with matter

Gamma- ray photons are electromagnetic radiation that propagates at the speed of light (c), and it is characterised by discrete energy. The frequency (λ), wavelength (ν) and speed of light (c) of electromagnetic radiation are related by the equation:

$$c = \nu\lambda \quad (2.10)$$

The energy of a γ - ray photon (E) can be related to the frequency by:

$$E = h\nu \quad (2.11)$$

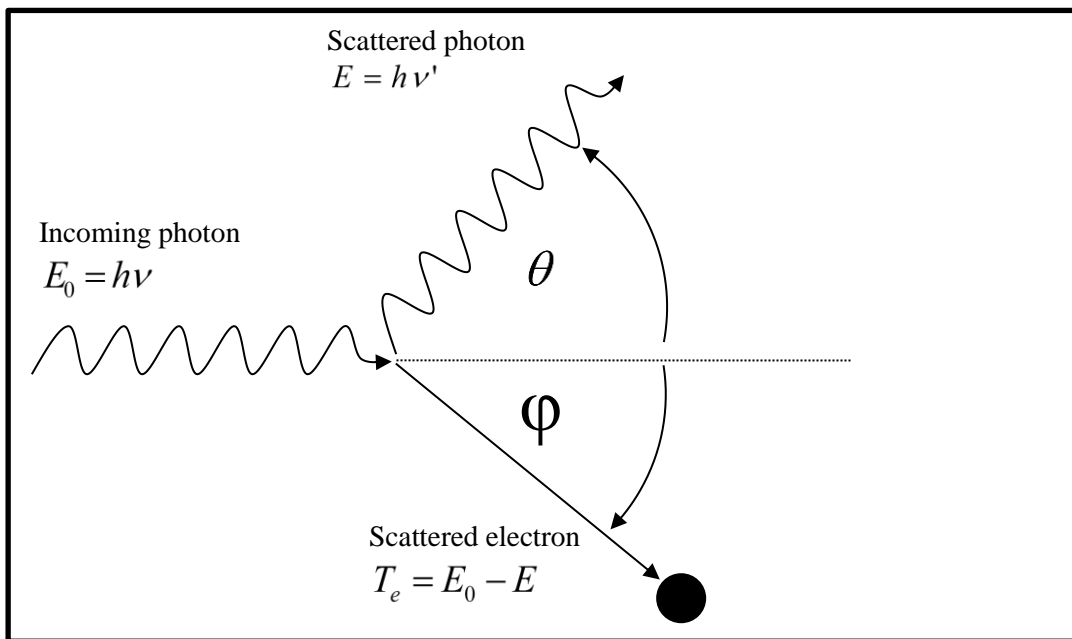
where h is Planck's constant (6.6261×10^{-34} Js). γ - ray photons have the highest energies of all the photons in the electromagnetic spectrum. γ - ray photons also have the ability to interact with matter that can cause the γ - ray photon energy to be either partially or completely transferred to an electron. The transfer of γ - ray photon energy to an electron forms the foundation of gamma radiation detection for energies up to 3 MeV. γ - ray photons interact with matter according to four mechanisms: photoelectric absorption, Compton scattering, pair production, and elastic or Rayleigh scattering (Knoll 2000; IAEA 2003).

In **photoelectric absorption** a γ - ray photon completely transfers all its energy to an atomic electron, which is then called a photoelectron. This energetic photoelectron is then ejected from one of the atom's bound shells (Knoll 2000; Hendriks 2003; IAEA 2003). The energy of the photoelectron will be expressed as:

$$E_{e^-} = E_{\gamma} - E_b \quad (2.12)$$

where E_{γ} is the incident γ - ray photon energy and E_b is the binding energy of the photoelectron in the atom. The ejected photoelectron leaves a vacant space in the atom that is filled by another electron from the next outer shell. This might cause a characteristic X-ray to be discharged which is then usually absorbed by a loosely bound electron from the outer shell of the atom. The total of the combined energies of all affected photoelectrons is equal to the incoming γ - ray photon energy. Photoelectric absorption is the main interaction method for incoming γ - ray photons with relatively low energies, up to a few hundred eV, or a reaction matter with a high Z number (Knoll 2000; IAEA 2003).

Compton scattering occurs when an incoming γ - ray photon undergoes an elastic collision with an electron in the absorbing material's atom, as depicted in Figure 2.4.



Source: Knoll (2000:51); Hendriks (2003:20)

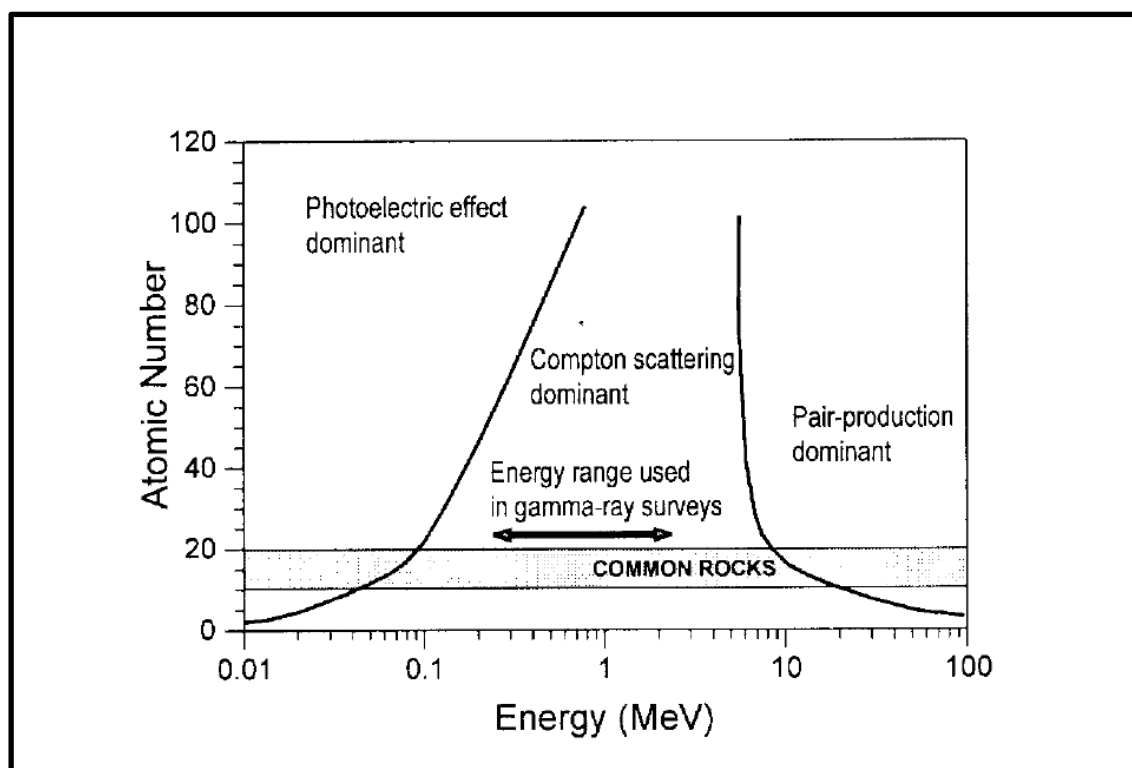
Figure 2.4 An incoming γ - ray photon undergoing Compton Scattering with an electron.

Figure 2.4 depicts an incoming γ - ray photon with an energy of $E_0 = h\nu$ colliding with an electron. The γ - ray photon is scattered at an angle θ and the electron at an angle ϕ with reference to the original track of the γ - ray photon. The γ - ray photon's energy is reduced to $E = h\nu'$ and the scattered electron's received energy (T_e) is the difference between the initial and final γ - ray photon energy. The incoming γ - ray photon is deflected through an angle θ with respect to its incoming path. During the collision an energy transfer occurs between the γ - ray photon and electron; the deflected electron is now known as the recoil electron. The scattering angles of the γ - ray photon varies from 0° to 180° , which is due to the amount of energy that is transferred and can differ from zero to almost all of the γ - ray photon energy. The energy E'_γ of the scattered γ - ray photon can be calculated by using the conservation of energy and momentum:

$$E'_\gamma = \frac{E_\gamma}{1 + \frac{E_\gamma}{m_0 c^2} (1 - \cos \theta)} \quad (2.13)$$

with $m_0 c^2 (= 0.511 \text{ MeV})$ equal to the rest mass of an electron. The γ - ray photon always retains some of its original energy, even in the case where the scattering angle is maximum, $\theta = \pi$. The probability of Compton scattering increases linearly with the increase of Z of the absorbing material (Knoll 2000; IAEA 2003).

Pair production becomes possible once the energy of the incoming γ - ray photon energy exceeds 1.02 MeV, twice the electron rest mass energy, or higher. However, pair production only becomes the dominant reaction mechanism for energies above 5 MeV (Hendriks 2003). It is also recognized in natural gamma radiation with energies up to 3 MeV. In practice the probability of pair production remains low up until the γ - ray photon energy reaches a number of MeV's. This means pair production mostly occurs during high energy γ - ray photon interactions. Pair production takes place in the coulomb field of a nucleus where the γ - ray photon transforms into an electron-positron pair. The excess energy of the γ - ray photon above 1.02 MeV is converted to the kinetic energy of the electron-positron pair. Two annihilation photons are produced once the positron has slowed down and annihilates. These annihilation photons are the secondary product of pair production (Knoll 2000; Hendriks 2003; IAEA 2003). Figure 2.5 gives a clear indication of how the interaction types are associated with specific γ - ray photon energies.



Source: IAEA(2003:11)

Figure 2.5 The interaction of γ - ray photons with matter expressed in terms of atomic number and energy. The areas indicate which interaction method is dominant in the various regions.

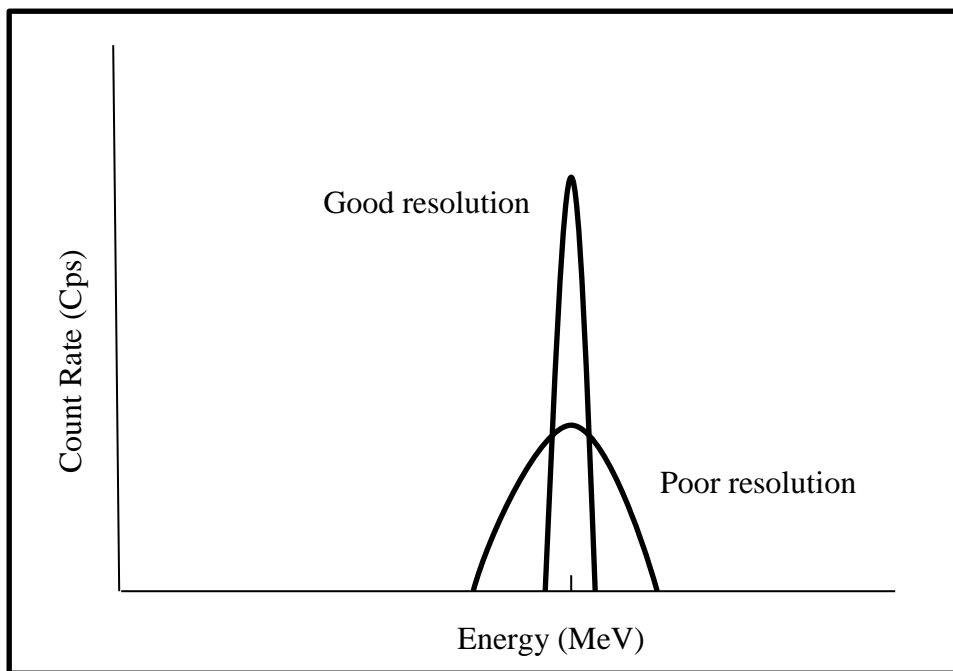
During **elastic scattering** almost no energy is transferred from the γ - ray photon. Only the direction of the γ - ray photon is changed. This type of scattering only takes place for energies below 100 keV and for absorbing materials of a high Z values (Knoll 2000; Hendriks 2003; IAEA 2003).

2.3.4 Detector response

Radiation possesses ionization characteristics. When radiation comes into contact with matter interaction certain physical and chemical effects occur. Detection instruments are designed to convert these physical and chemical effects to electrical signals that are suitable for detection. These detectors convert the radiation, be it alpha, beta or gamma radiation, to electrical signals that can equate to the energy of the detected radiation. There are various types of detection crystals that are available for use, as discussed in Chapter 1. The criteria for selecting the best detector was based purely on the detection need, as some detectors are more robust than others but have a lower efficiency, or some detectors have a very good efficiency and energy resolution but are very large in physical size. For the purpose of this research *in situ* measurements were the mode of collecting data. Therefore, the main criteria to consider when

selecting a detector would be aimed at portability, durability, and toughness, hence the choice of a Sodium Iodide Thallium Infused (NaI(Tl) detector (7.62 x 7.62 cm)).

The efficiency of a detector is the probability that incoming radiation will be absorbed by the detector crystal, in other words how much of the incoming radiation is actually detected and how much passes straight through the detector crystal or is lost due to other processes. The energy resolution of a detector is the ability of the detector to distinguish between two different γ - ray photons whose energies are very close to each other. The peaks of an energy spectrum from a detector with a good energy resolution will be very narrow in width. Figure 2.6 shows the difference between a response function with a good resolution against one with a poor resolution.



Source: Knoll (2000:113)

Figure 2.6 An energy spectrum demonstrating the comparison of response functions between good and poor resolution.

The energy resolution of a detector is defined by describing a photo peak in the energy spectrum of the detector, the term full width at half maximum is used (FWHM). The FWHM describes the full width of the photo peak at half of the maximum amplitude divided by the energy of that photo peak. The energy resolution of detectors used during *in situ* γ - ray photon measurements are standardised on the FWHM of the ^{137}Cs photo peak at 662 keV.

Another factor that was considered during the process of selecting a detector is dead time. The dead time of a detector is the time it takes for a detector to process a detected γ - ray photon. During this process all other gamma interactions are disregarded. Dead time can be caused by the physical processes in the detector itself, or by the electronics of the detector system. There will always be a probability that some of the decay events will be lost because of the statistically random nature of radioactive decay, especially when a decay event is directly followed by another. The dead time of a detector will also increase with an increase in counting rates. All attempts must be made to keep the dead time of any detector as small as possible (Knoll 2000; Hendriks 2003; IAEA 2003).

The detector size will have an influence on factors such as dead time, efficiency and resolution. As mentioned already in this section, for *in situ* measurements a smaller more robust detector would be ideal. The NaI(Tl) detector (7.62 x 7.62 cm) detector consists of a scintillator crystal (NaI(Tl)) and a photomultiplier. The principle of operation of a scintillator counter is based on the process by which an incoming γ - ray photon interacts with the scintillation crystal and produces scintillations. These scintillations are weak photons of visible light that are collected by the photomultiplier tube that in turn convert these photons into an electrical signal for detection purposes. The corresponding electrical signal output is a negative voltage pulse that has an amplitude that corresponds to the energy of the incident γ - ray photon. The electric pulses are then analysed and plotted by the multi-channel analyser (MCA) according to amplitudes. The final pulses are then placed by the MCA in a channel of which the address is proportionate to the value of the corresponding pulse amplitude. The output can be seen as the energy spectrum of the number of detected γ - ray photons per channel, as indicated in Figure 2.7 (Knoll 2000; Hendriks 2003; IAEA 2003).

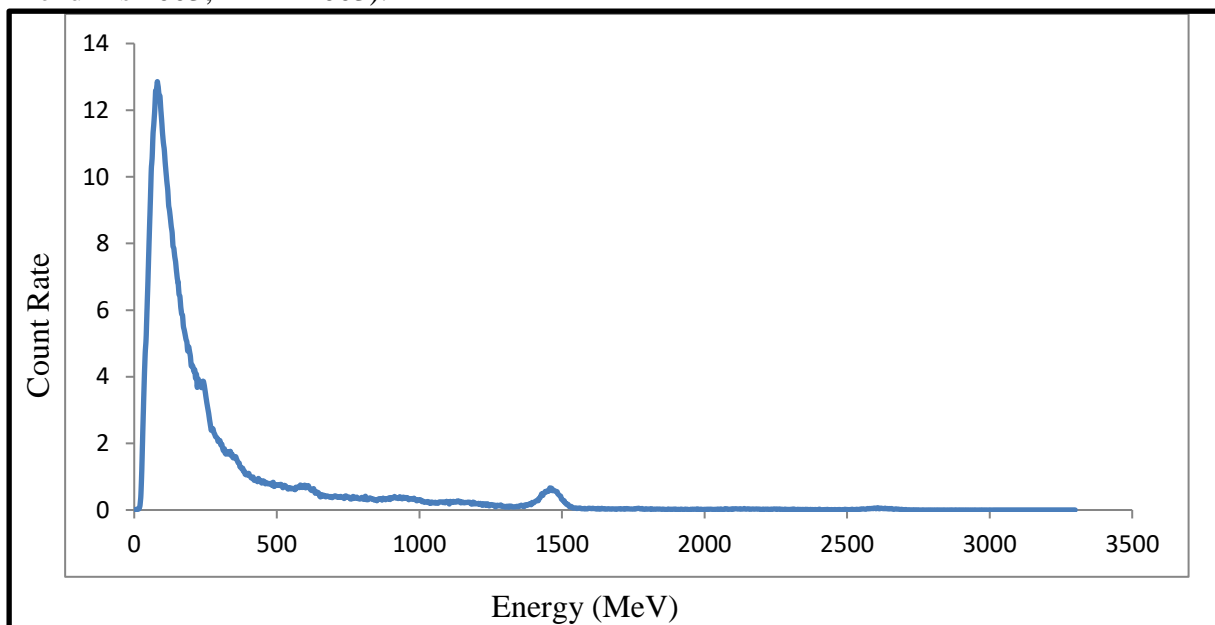
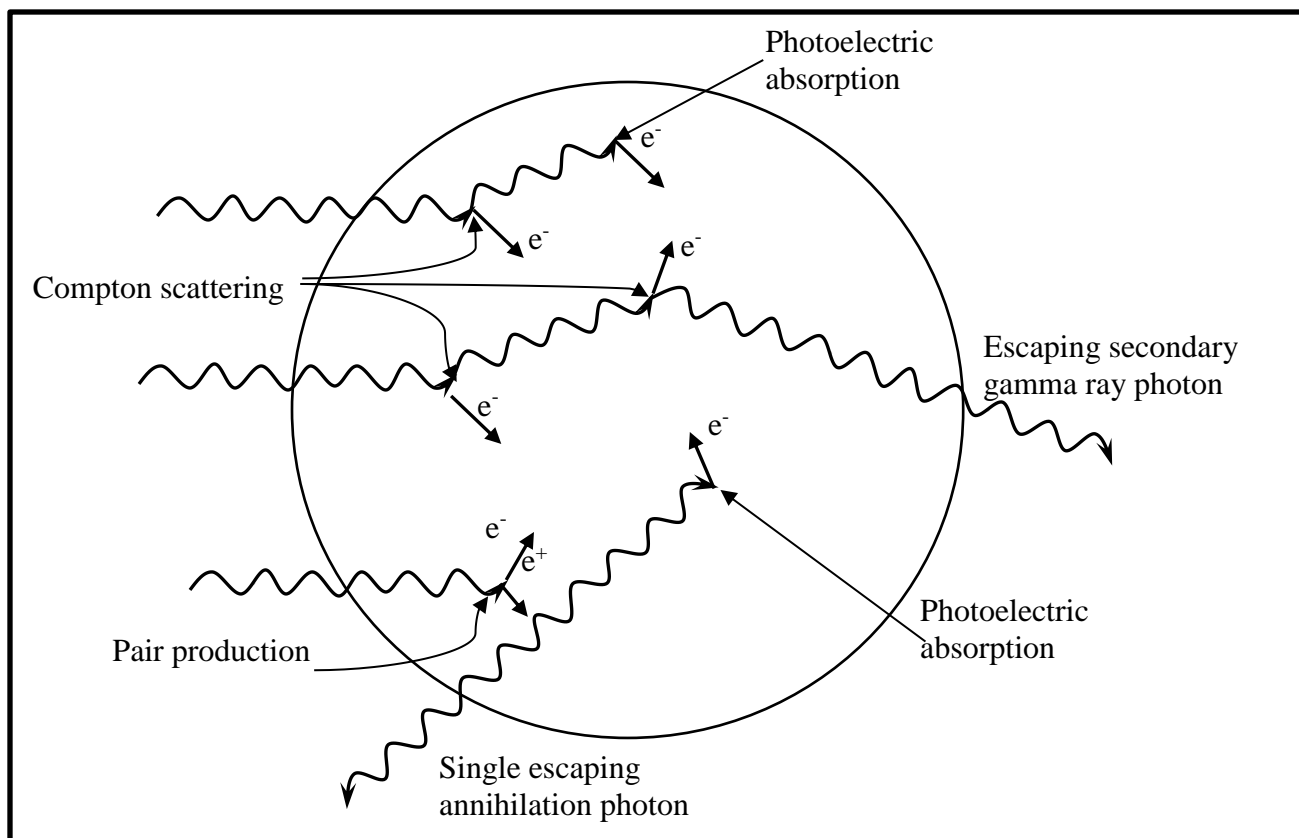


Figure 2.7 Example of an energy spectrum of the recorded radiation from one measurement.

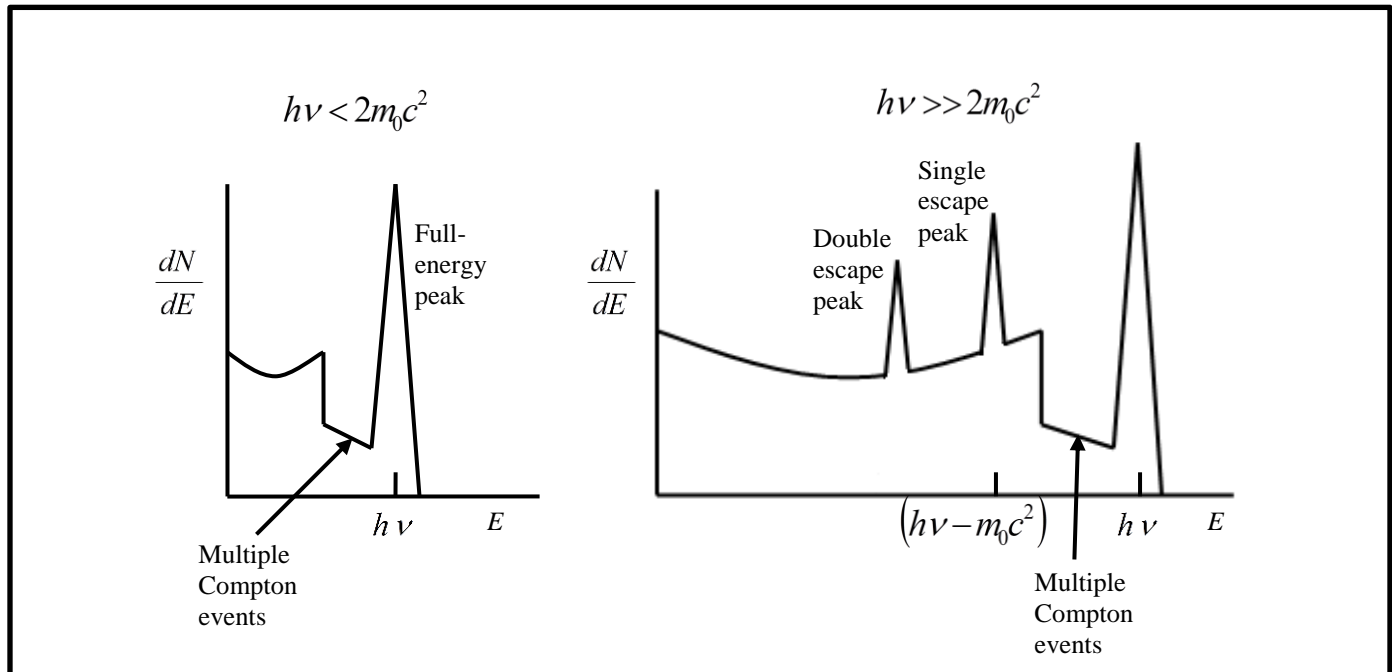
The interaction mechanisms within the detector varies according to the detector size. For small detectors, detectors of dimensions not exceeding 2 cm, the interaction mechanisms that are responsible for the final energy spectrum are mostly due to secondary gamma radiations. Secondary gamma radiation occurs from Compton scattered γ - ray photons and annihilation photons from pair production that takes place due to the interactions from the original incoming γ - ray photons and the detector crystal. In small detectors some of the secondary radiation will escape the detector. The opposite will occur in large detectors. A large detector is theoretically defined as a detector large enough for all secondary radiation to interact within the detector without allowing anything to escape. This type of detector is normally the size of tens of centimeters and will definitely not be suited for *in situ* measurements. A NaI(Tl) detector of 7.62 x 7.62 cm is classified as an intermediate size detector. Figure 2.8 provides a graphic illustration of the radiation events, the secondary radiation events and the escaped gamma radiation of an intermediate size detector. It can be seen from Figure 2.8 that some γ - ray photons are completely absorbed, and that some secondary radiation escapes detection (Knoll 2000).



Source: Knoll (2000:316)

Figure 2.8 A graphic representation of the γ - ray photon interactions in an intermediate size detector. This type of detector is small enough to transport and to be used for *in situ* measurements

The energy spectra indicate the effects of the secondary radiation, as shown in Figure 2.9. The continuum of energies in the low energy ranges of the energy spectrum is the result of the continuum of energies generated by Compton scattering. The narrow peak on the graph is known as the full energy or photo peak. Photo peak is an indication of the amount of incoming γ -ray photons that was fully absorbed within the detector. The left-hand graph is an example of an energy spectrum where the incoming γ -ray photon energy is low enough for pair production not to occur, whereas the spectrum on the right is an example of γ -ray photon energy high enough for pair production to occur (Knoll 2000).



Source: Knoll (2000:316)

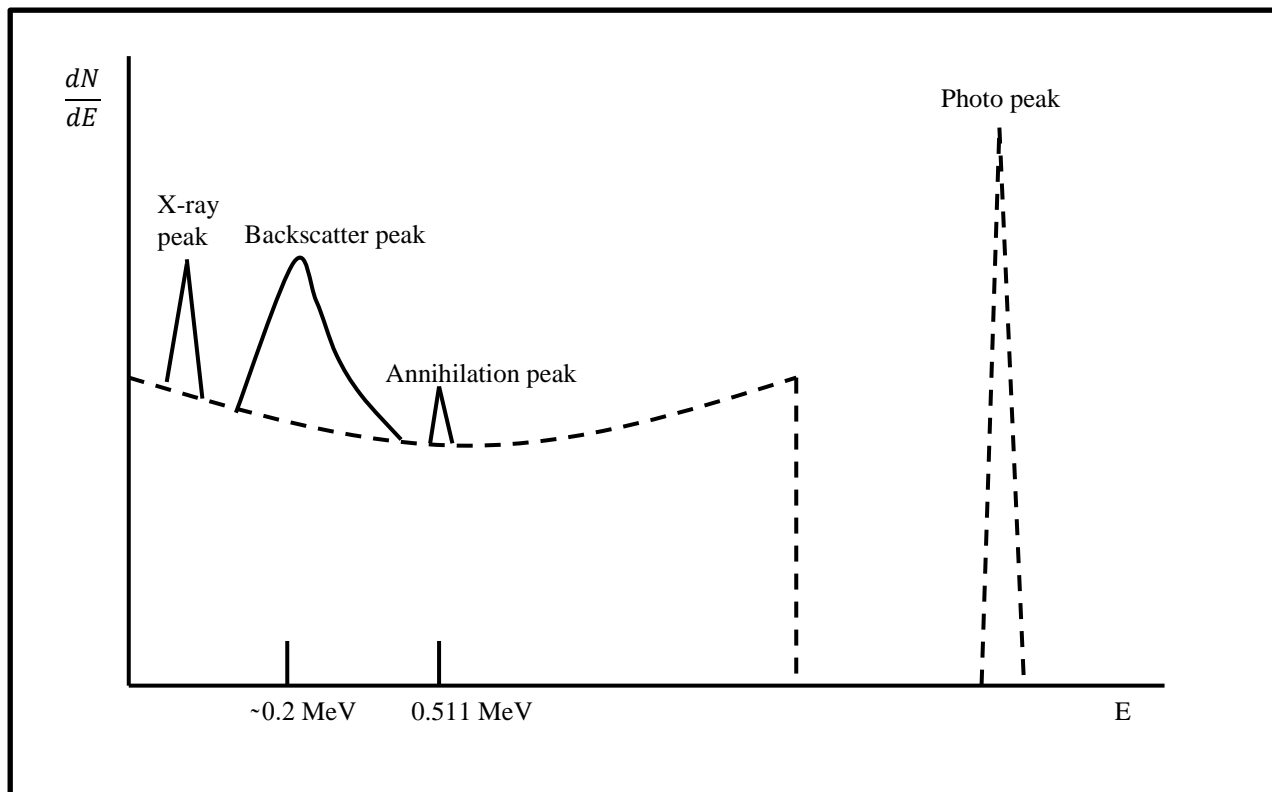
Figure 2.9 The two spectra that demonstrate the interaction of γ -ray photon with higher and lower energies with detectors.

In Figure 2.9 the graph on the left indicates the lower gamma-ray energies, below $2m_0c^2$ and on the right the higher energies, above $2m_0c^2$. The graph on the left shows the continuum from Compton scattering, the full energy peak and the influence of multiple Compton events caused by photon escape. The graph on the right additionally shows the single and double escape peaks.

The annihilation photons from pair production may escape the detector or may undergo further interaction mechanisms and be fully absorbed. These interactions lead to additional escape peaks known as single escape and double escape peaks. The double escape peak occurs if both annihilation photons escape without interaction. Single escape peak results if only one annihilation photon escapes and one

gets absorbed. Single escape peak appears at an energy of m_0c^2 or 0.511 MeV below the photo peak. The continuum of energies between single and double escape peaks are due to the possibilities of energies that exist if one or both annihilation photons are partly converted to electron energy via Compton scattering. The energy spectrum or response function is not only a product of the interaction mechanisms that occur within the detector crystal, but are also influenced by the interaction mechanisms that occur near the source and the detector housing (Knoll 2000).

The detector crystal is housed in a detector that consists of materials that could have a significant influence on the final energy spectrum, and in the case of *in situ* measurements, so could the soil and immediate surrounds. Both the detector and surrounds are potential sources of secondary radiation. Figure 2.10 shows the resultant energy spectra caused by these secondary radiations (Knoll 2000). In terms of this research it was assumed that all secondary radiations from the detector and surrounds were standard for all measurements and could thus be ignored.



Source: Knoll (2000:320)

Figure 2.10 A spectrum indicating the influence of the surrounding materials on the incoming γ -rays.

The graph indicates the expected gamma-ray spectrum due to the influence of the surrounding materials. The energy peak in the area of 0.2 to 0.25 MeV is called the backscatter peak, and is a result of the Compton scattering of the incoming γ - ray photons in the surrounding materials of the detector. The first peak in the spectrum, the X-ray peak, is the result of photoelectric absorption in the surrounding materials that releases a characteristic X-ray. Incoming γ - ray photons with high energies may react in the detector surrounding material and yield to annihilation radiation photons. This annihilation peak can appear at 0.511 MeV. Additional peaks may also appear in the energy spectrum. These peaks are the result of summation effects, and are caused by the coincident detection of two or more γ - ray photons with the same energy (Knoll 2000). The energy spectrum is a result of the energy of the incoming γ - ray photon together with all the other interaction mechanisms detected by the γ - ray detector.

It is thus clear that gamma radiation detection is dependent on detecting the specific energy of a decay event and producing a spectrum of the detected energies. The activity concentration (C) of any sample of radiation is defined as the activity per unit of mass and is presented in Becquerel per kilogram, Bq/kg. The displayed energy spectrum of a radiation source, shown in Figure 2.7, indicates the count rate, in counts per second, for every channel of detected energy. The count rate on the spectrum is then converted to activity concentration, as discussed in sections 3.2 (Knoll 2000; IAEA 2003).

Every α and γ radiation event has a distinct energy associated with its parent nuclide. The concentration of the nuclide is related to the amount of Becquerel detected of the specific energy. This can be seen on the energy spectrum as peaks on certain energy channels, such as peak A and B on Figure 2.7. As for beta decay, the emitted undetected neutrino or anti-neutrino varies in energy, thus every decay event produces a different amount of energy. This in turn produces an energy spectrum of the emitted β^\pm particles that is continuous (Hendriks 2003).

2.4 DENUDATION PROCESS IN THE PHYSICAL ENVIRONMENT AND NATURAL RADIATION

Natural radionuclides have been present on earth since the formation of the first rock. As the rate of denudation increased over time, more soil and regolith was formed. The natural radionuclides have since also formed part of the mineral composition of soil and regolith. As time on Earth went by, so have soil and regolith been spread over larger surface areas away from their parent materials, and so have the natural radionuclides in soil and regolith been spread across the surface of the earth. The concentrations

of these radionuclides varies over the surface of the earth because of the various local geographic factors that influence denudation of the physical surface. The concentrations of the natural radionuclides can be measured because each natural radionuclide produces gamma radiation with a very specific energy signature. The amount of gamma radiation from these radionuclides can be measured, because of the gamma radiation's interactive properties with matter, by means of a γ -ray detector. The NaI(Tl) detector (7.62 x 7.62 cm) was the choice of detector as it is an efficient portable detector ideally suited for *in situ* measurements. The end product of detection is an energy spectrum which provides a graphic illustration of the concentrations of the specific γ -ray photons present.

By using the natural radionuclide concentration values extracted from the γ -ray energy spectra, radioelement maps may be drawn through GIS software and techniques. The next chapter will discuss the research site, methods and equipment necessary to compile radioelement maps.

CHAPTER 3: RADIATION MEASUREMENT AND ANALYSIS ON BAVIAANSBERG

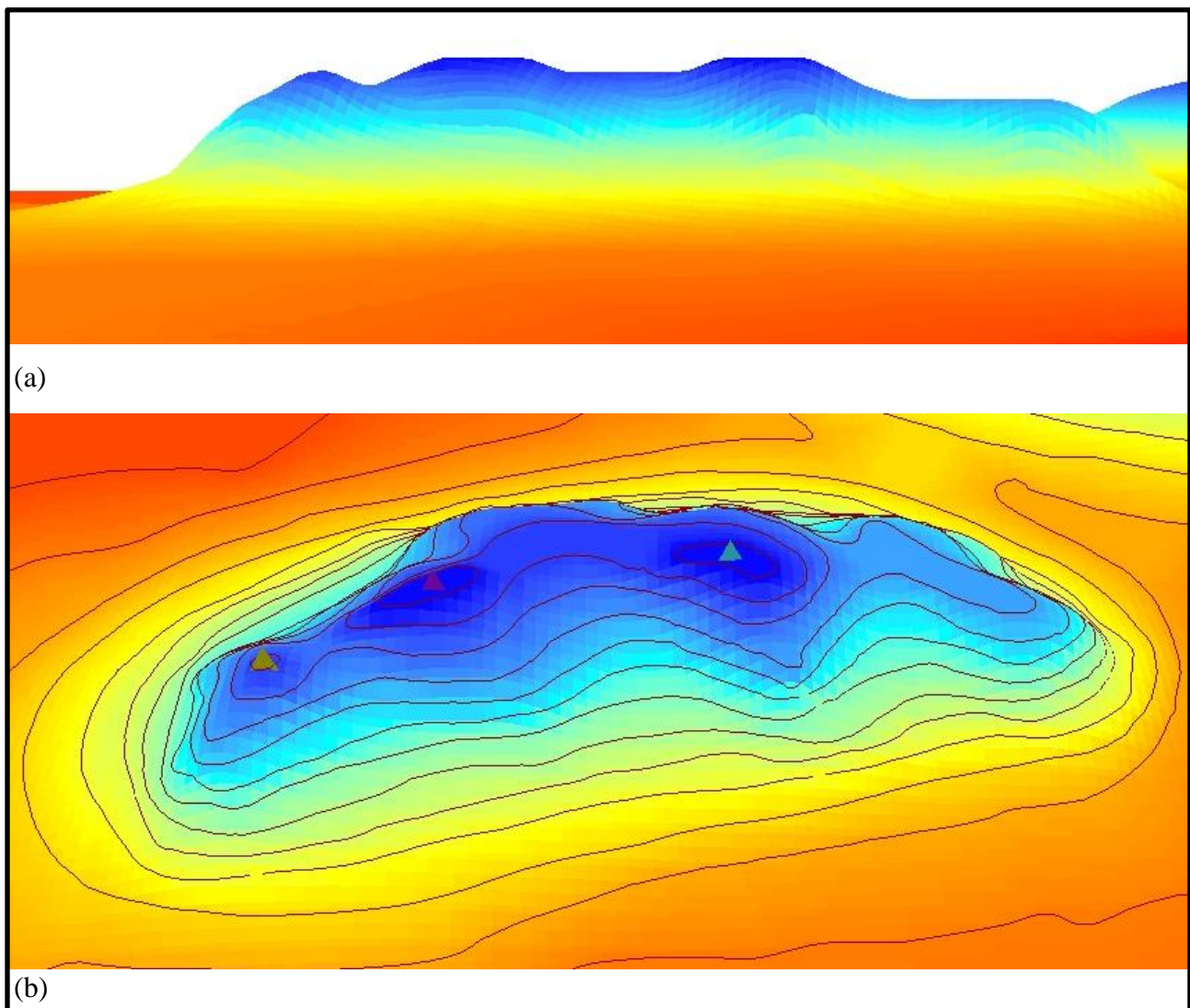
The unique physical characteristics and geographic terrain of the Saldanha Military Area and Baviaansberg will be the opening theme of this chapter. This is followed by an in-depth explanation of both the radiation measurement of Baviaansberg and the procedure of full spectrum analysis of the Baviaansberg data. Techniques for mapping the radiation of Baviaansberg will also be described. The chapter concludes with a summary.

3.1 THE SALDANHA MILITARY AREA AND BAVIAANSBERG

The research site is situated in the Saldanha Bay Military Area (SMA), close to the town of Saldanha Bay on the West Coast of South Africa. The site identified for the research is named Baviaansberg, as indicated in Figure 1.1 (a). It is located on a small peninsula at the northern end of Saldanha Bay. This specific site was chosen because of its unique geography. The geography of Baviaansberg is characterised by the prevailing south-easterly summer winds and the north-westerly winter winds that reach the hill directly from the ocean. The fact that both the winter and summer winds of Baviaansberg are onshore contributes to the uniqueness of the area. The onshore nature of the winds makes it reasonable to accept that aeolian deposition will be minimal. This means that the soil within the research site are influenced minimally by the geology from outside of the research site. The overwhelming majority deposition that occurs in the research site originates from the underlying geology of the area itself.

Local rainfall is another important geographic factor likely to influence the denudation of the area. The research site is situated in a predominantly winter rainfall region, yet occasional summer rains do occur (Provincial Government of the Western Cape 2005). Rainfall plays an important role in terms of distributing soil, and in turn, natural radionuclides across the research site. Rainfall and wind direction also have a direct bearing on the aeolian erosion that occurs within the research site. Aeolian erosion will be more prominent in the dry summer months when the south easterly winds prevail than in the wet winter months characterised by predominantly north westerly winds. The research site's soil formation is consequently influenced almost exclusively by local geographic factors. All radiation results were analysed and discussed through a consideration of local geographic factors, and their influence on natural radionuclide concentrations.

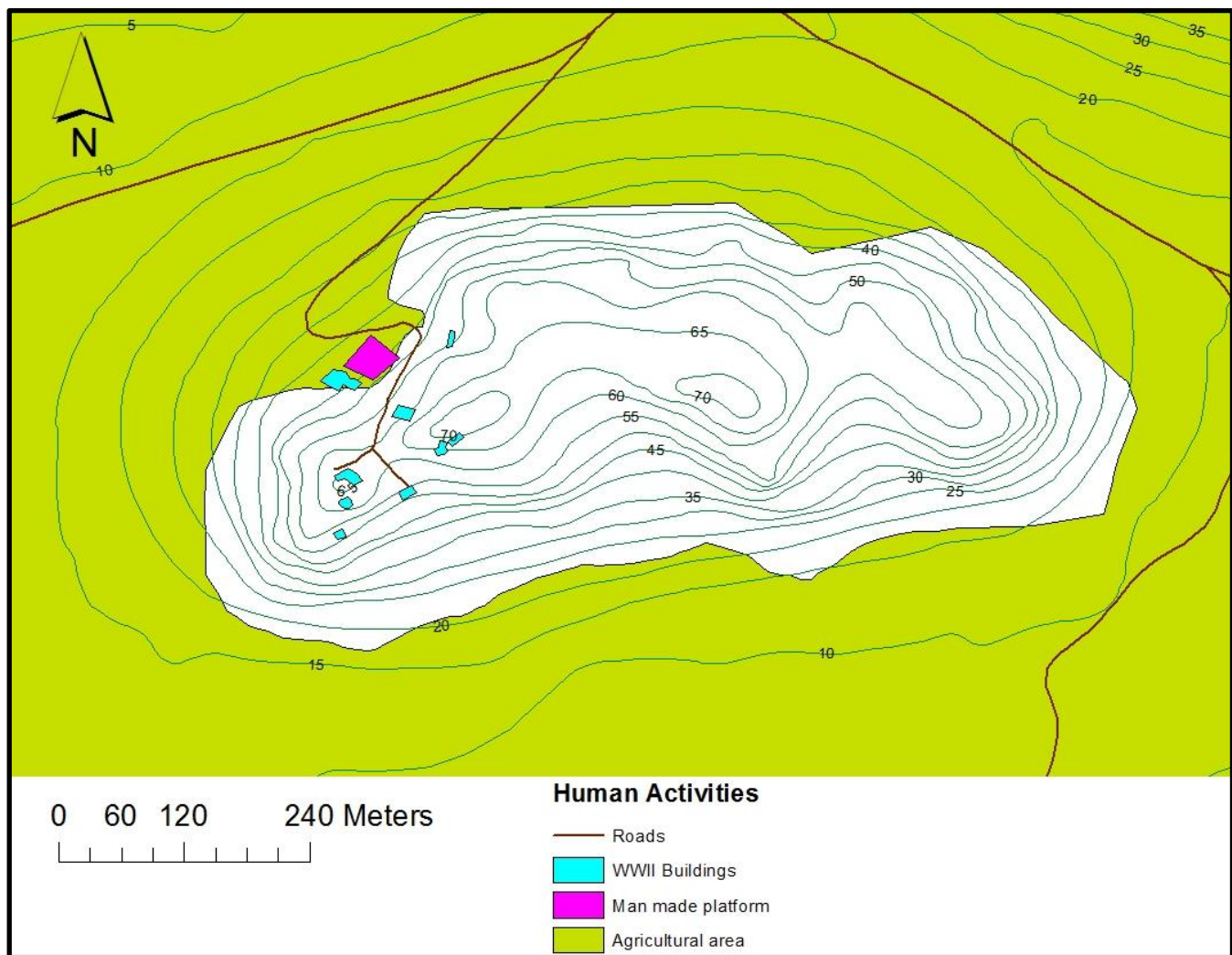
Baviaansberg in the research site is a small hill, with a height of 72 meters above mean sea level and a surface that is dominated by granite outcrops. The foot of Baviaansberg is 15 meters above mean sea level. It consists of three identifiable peaks, as indicated in Figure 3.1 (a) and (b), viz. the western, central and eastern peaks. Vegetation on Baviaansberg is classified as Saldanha Granite Strandveld that forms part of the Western Strandveld Bioregion, which again forms part of the greater Fynbos Biome (CSIR 2014). Its climate is classified as Mediterranean with an average annual rainfall of 220mm. The area is adjacent to the Namaqualand desert region (CSIR 2014). The area was exposed to diverse human activities over time.



Adapted from South Africa (1997)

Figure 3.1 A three-dimensional image extracted from a DEM of Baviaansberg. (a) A southerly view of the clearly visible three peaks of Baviaansberg. (b) An elevated view of Baviaansberg with the eastern peak indicated by the turquoise beacon, the central peak by the purple beacon and the western peak by the yellow-green beacon.

The imprint of human activities on the research site is reflected by roads and old buildings as well as the difference in vegetation cover between undisturbed areas and older agricultural areas. These human activities are indicated in Figure 3.2. There is a road on the north-western slope of Baviaansberg that leads up to the hill towards a man-made platform. The man-made platform is a built up platform where the soil has been compacted. There are World War II ruins and surviving buildings situated on Baviaansberg that commences from the 45 meter contour along the road to the top of the hill and are spread from the south-western section to the centre of Baviaansberg between the 45 meter contour and the top of the hill. The area of Baviaansberg was used for agricultural purposes after World War II. Areas impacted by farming activity are indicated in Figure 3.2. These old agricultural fields are in process of being naturally reclaimed by Saldanha Granite Sandveld Fynbos (Bezuidenhout 2012). Parts of the road surrounding Baviaansberg run through the research site at the northern and south-eastern boundaries.



Adapted from South Africa (1997)

Figure 3.2 The areas of human activities in the research site.

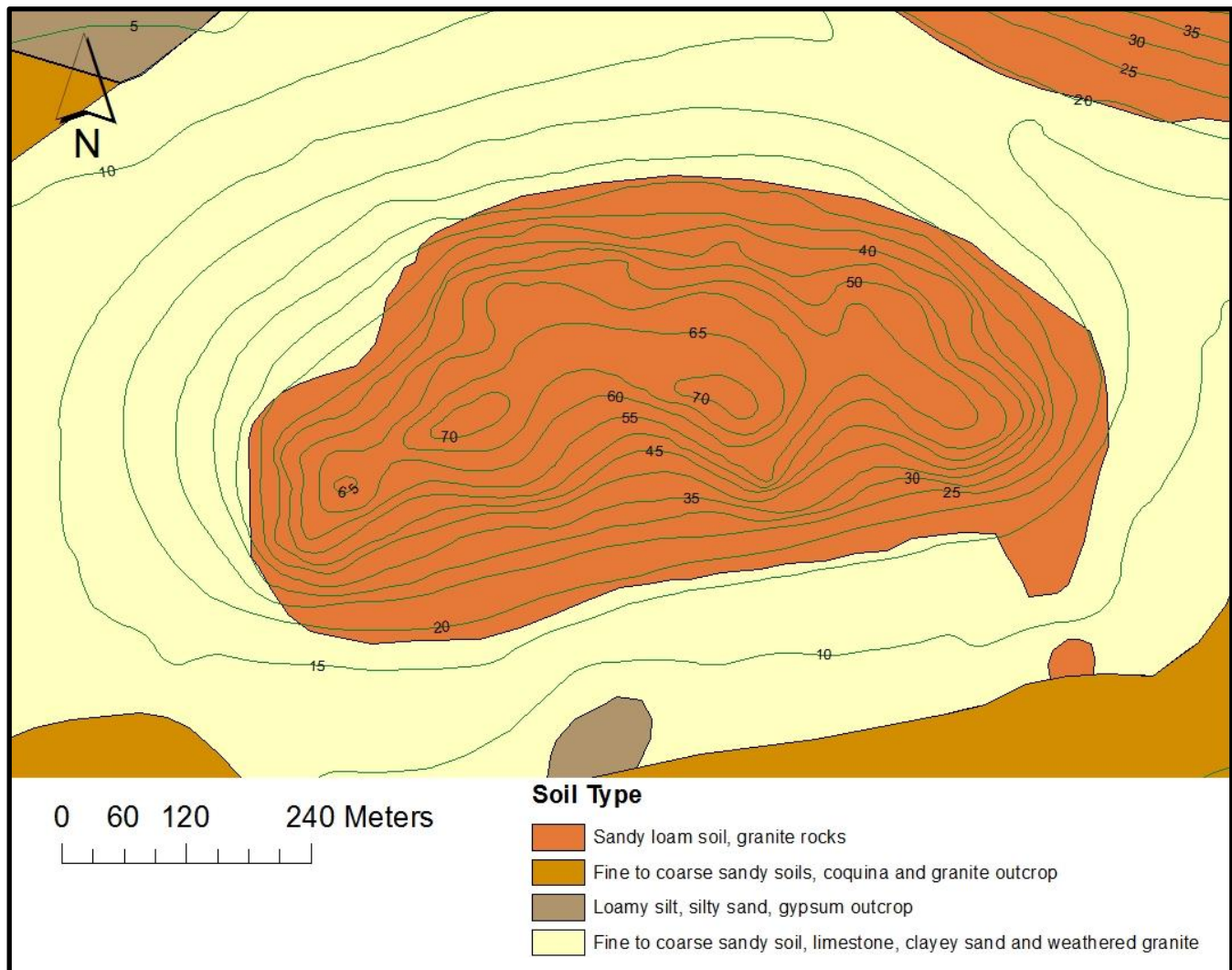
In Figure 3.2 the green area is the area used for agriculture post WWII. The turquoise and purple areas represent the buildings and platform constructed during WWII. There is also a road leading up to the WWII structures. The road also travels towards the north-western, north-eastern and south-eastern ends of the research site.

The north-eastern corner of the research site forms part of the western slope of the neighbouring hill, Malgaskop. This is evident in Figures 3.2 and 3.3 where the distance between the contours in the north-eastern corner of the research site starts to decrease from the 20 meter contour. During the field work phase of this research it was noted that there are no pertinent gully's or streams in the research site; an indication that water flow over the research site is mainly overland. For the purpose of this research it was inferred that the surrounding soils are mainly formed by denudation of the granite outcrops. The granite outcrops are indicated in Figure 1.1(c). It is important to note the positions of the granite outcrops, areas indicated as light grey in Figure 1.1(c) of the demarcated research site. Bezuidenhout (2012) showed that the average natural radionuclide concentrations of the granites on Malgaskop for ^{40}K , ^{232}Th and ^{238}U are 1348.5 Bq/kg, 102.5 Bq/kg and 59.0 Bq/kg respectively. These measurements was used as a baseline for the natural radionuclide concentrations of the granites on Baviaansberg.

The theoretical discussion in Chapter 2 on the geology of the research site explained the mineral composition of granites and how said composition influenced the radiation signature of granite areas. The mineral composition of granite contains natural radionuclides with unique radiation signatures. Soil that originates from these granites will then bear a similar mineral composition and the same radiation signature as the parent material. The radioactive nuclides in the mineral composition of the soil also determines the radiation signature of that soil. As soil is transported further away from its parent material, the concentration of these nuclides may become dispersed and diluted. Additional biological matter such as dead organic remains or broken shells can also be added to the soil, which will contribute to the reduction in the concentrations of the radionuclides in the soil. Figure 3.3 shows the various soil types located within the research site.

In Figure 3.3 shows the various soil types found in the research site, it can be seen that, except for the area south east of Baviaansberg, the 'sandy loam soil, granite rocks' soil layer occur only upslope from the 15 meter contour. The areas below the 15 meter contour are dominated by 'fine to course sandy soil, limestone, clayey sand and weathered granite' soil layer. The two main types of soil within the research

site are ‘sandy loam soil with granite rocks’ (SLG) soil type and ‘fine to coarse sandy soil, limestone and clayey sand with weathered granite’ soil type (FCS) (Greyling 2001).



Source: Adapted from South Africa (1997)
and Greyling (2001)

Figure 3.3 Soil type of the research site.

The SLG soil type is situated in the centre and north east corner of the research site with the exception of the small area in the south east corner. The FCS soil type is situated around the SLG soil type downslope of Baviaansberg (Greyling 2001). The ‘fine to coarse sandy soils with coquina and granite outcrops’ soil type (FCQ) is situated in the north-west, south-east and south-west corners of the research site (Greyling 2001). A ‘loamy silt, silty sand with gypsum outcrop’ soil type is situated in the north-west corner and a small area in the middle of the southern boundary of the research site (Greyling 2001).

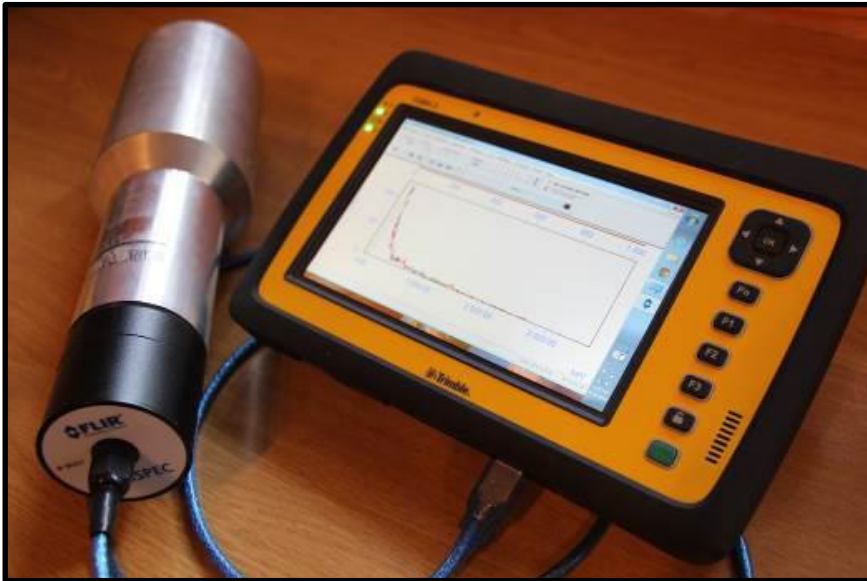
The next section deals with the measurement equipment and techniques used to generate nuclide concentration levels that were used for qualitative data analysis.

3.2 RADIATION MEASUREMENT ON BAVIAANSBERG

Section 3.2 will commence with a description on the device setup and calibration used during research, followed by a discussion on the sampling procedure. The section will conclude by stating the methods and procedures used for data collection.

3.2.1 Device setup and calibration

The system used for *in situ* measurements is the same setup as was used by Bezuidenhout (2012). A Sodium Iodide Thallium Infused (NaI(Tl)) scintillation detector with a 7.62 x 7.62 cm crystal housed in an aluminium casing was used. This was coupled to a scintiSPEC Multi-Channel Analyser (MCA) that is produced by FLIR® (FLIR 2015). The scintiSPEC MCA regulates the detector system operating voltage and signal communication via its USB connection. This setup was connected to a Trimble Yuma Rugged tablet PC (Trimble 2015). The Yuma is equipped with an on-board GPS that provided an output of latitude, longitude and height above mean sea level. The scintiSPEC MCA was connected to a tablet computer via its USB connection in order to provide the operating voltage and signal communication to the NaI(Tl) scintillation detector. WinTMCA32 software with 1024 energy channels, also designed by FLIR®, was installed on the tablet. This software controlled the detector system and the acquisition of γ -ray photon spectra. The WinTMCA 32 software plots the count rate to the energy of the γ radiation counts. The entire detection setup is displayed in Figure 3.4. It will be referred to as “the detector system”. Once the detector system was energy calibrated, the final data of the detector system was stored in the form of an energy spectrum, as discussed in Section 2.3. Energy calibration of a detector is paramount for the detector system to transform channels to energy. Energy calibrations were performed by using radiation sources with known energy peaks, similar to those used by Noncolela (2011). The calibration method will be discussed later in this section.

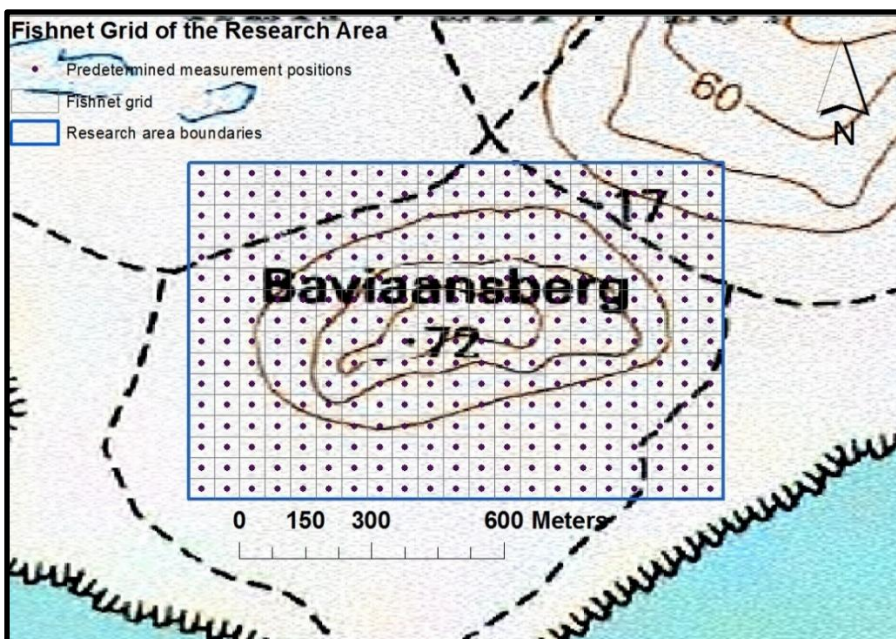


Source: Bezuidenhout (2015b: 2)

Figure 3.4 The detector system, as used by Bezuidenhout (2015b).

3.2.2 Sampling procedure

A systematic sampling design was followed to determine the measurement positions before any field measurements commenced (Congalton & Green 2008). The research site was demarcated by creating a fishnet grid, using ArcMap, over Baviaansberg on a 1:50 000 map with grid reference 3317BB (see Figure 3.5). The latitude and longitude of the four corners of the grid, starting at the south east corner and moving clockwise, are 33.045557° S and 17.907746° E, 33.039116° S and 17.907746° E, 33.039116° S and 17.918142° E, and 33.045557° S and 17.918142° E.



Source: South Africa (n.d.)

Figure 3.5 Fishnet grid and predetermined measurement positions of the research site.

The fishnet grid function in ArcGIS automatically determined the centre of each block in the grid. The grid was divided into sixteen rows and twenty-one columns. Columns ran exactly south to north, and rows west to east. Rows were labeled alphabetically from A to R. However, letters I and O were omitted to avoid ambiguity with numbers one and zero (National Geospatial Intelligence Agency 2016). Columns were numbered in ascending order from one to twenty-one. The size of each square within the grid was 48.6 meters latitudinal, and 47.6 meters longitudinal. The co-ordinate table was numbered in ArcMap, and exported to Microsoft Excel. The co-ordinate table was integrated with the concentration table, as indicated in Appendix A. The co-ordinate table was then amended in Excel to accommodate the actual latitude and longitude of the *in situ* measurement, the height above mean sea level of the measurement, and additional notes.

A specific point with latitude of -33.03257° S and longitude of 17.92154° E was chosen as a GPS control point. This point was surveyed with a differential satellite navigation system that uses GLONASS and GPS satellites for positioning. The reason for creating the GPS control point was to establish the GPS error and drift margins for the duration of research. It was also used as a control measure to establish the accuracy of the measurement positions. The GPS control point was measured with the Trimble tablet PC every day upon entering and exiting the research site. Figure 3.6 provides a plot of the distribution of the GPS control point measurements.

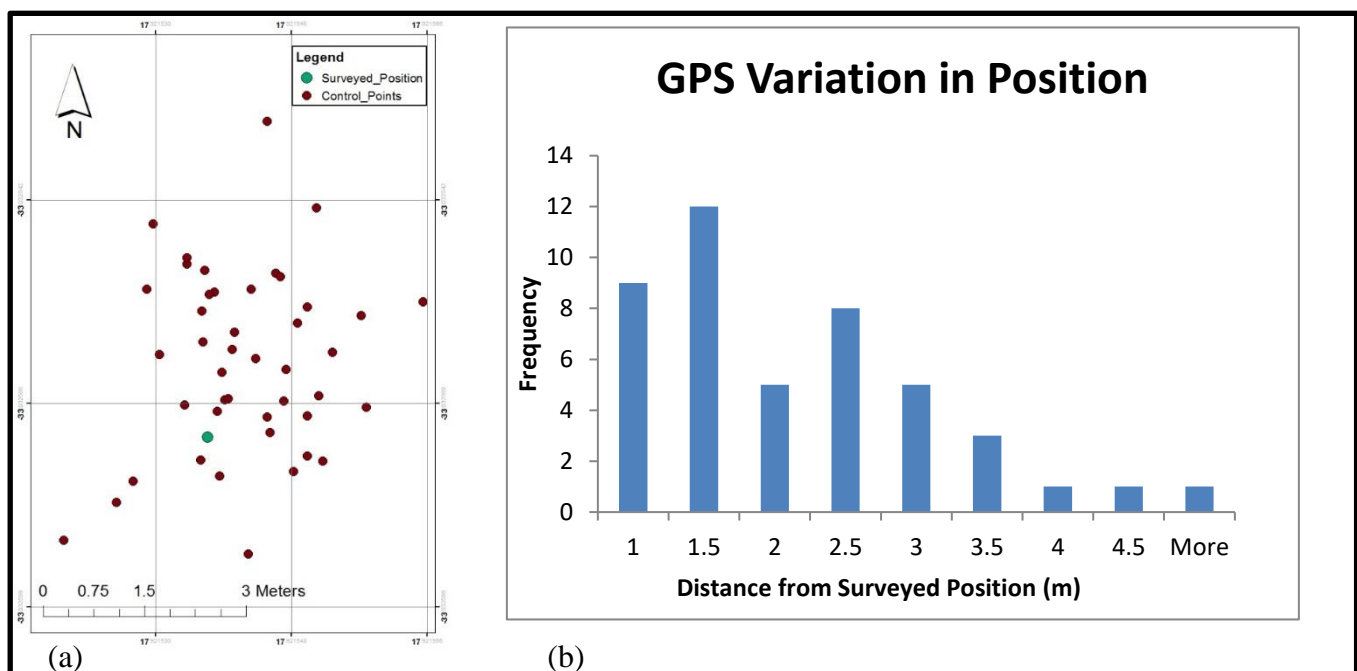


Figure 3.6 The distribution plot of the GPS control point measurements. Figure 3.6 (a) shows the latitudinal and longitudinal plot of the distribution of the GPS control point measurements. Figure 3.6 (b) provides a frequency distribution plot of the GPS error in meters.

From Figure 3.6 it is clear that there is a concentration of GPS control plots to the north of the surveyed position, the furthest point being 4.7 meter north of the surveyed position. The implications of the offset will be explained in the following paragraph. It can also be seen that 76% of control point measurements fall within 2.5 meters from the surveyed position. The grid blocks size in the research site is 48.6 meter by 47.6 meter. A maximum error of 4.7 meter therefore equates to less than 3% to the grid area, and an error of 2.5 meter less than 1% of the grid area. An error of less than 3% per grid area is acceptable in representing the data (Hulbert & French 2001). These plots also do not have to display sub centimetre accuracy as it constitute only a visual aid in the representation of data, and do not serve as maps to be used in navigation or any other spatially accurate exercise (Hulbert & French 2001; IAEA 2003). Control point measurements were taken for at least five minutes to allow for the GPS to obtain all available satellite data and to determine a more accurate fix of the measurement position (Tetley & Calcutt 2001). These control points were plotted and analysed in ArcMap. They are indicated in Figure 3.6 (a) to display visually the errors associated with the GPS.

3.2.3 Data collection

Measurements were taken during the dry summer months as moisture in the soil could affect gamma radiation measurements adversely (Jones & Carroll 1983; IAEA 2003). GPS measurements were determined while the *in situ* γ - ray photon measurements were taken. A time frame of five minutes was allocated for executing in tandem the GPS measurements and γ - ray photon detection. This time was estimated as adequate for the detector system to record an adequate number of γ - ray photon scintillation events (IAEA 2003). It also provided enough time for the GPS receiver to register an accurate latitude and longitude position. A copy of Appendix A was used in the field to identify the specific measurement position. The Trimble tablet PC was then used to find the corresponding measurement position in the field. The final measurement position was then written down in the table. Some of the final measurement positions were plotted in a different position than the predetermined positions, either because it was inaccessible due to dense vegetation, or because there were granite boulders obstructing the measurement position. The predetermined measurement positions were also moved if they were too close to rocks or boulders. The detector system was moved to the nearest viable measuring position at least 10 meters from any outcrop or rock. Radiation from these rocks might influence the detector readings if recorded in too a close proximity to the rocks, which would provide erroneous concentration levels (Sharma 1997; IAEA 2003). The time taken between two measurements was ten minutes, which included the *in situ* measurement and GPS fix, the writing down of the actual GPS position, any additional notes, and walking

time to the next measurement. A soil sample was taken with each of the *in situ* measurements in anticipation of possible future research. Radiation data was then analysed according to the process explained in Section 3.3. Once radiation data analysis was completed, it was ready to be used for qualitative analysis.

3.3 FULL SPECTRUM ANALYSIS OF THE BAVIAANSBERG DATA

WinTMCA32 software was used to perform energy calibrations. Sources used to perform the energy calibrations were ^{137}Cs and ^{60}Co nuclides. The 661.6 keV energy peak of ^{137}Cs and the 1173.2 keV and 1332.5 keV energy peaks of ^{60}Co were utilised to calibrate the system. These energy calibrations were performed every day before commencement of *in situ* measurements. The ^{137}Cs and ^{60}Co sources were placed in front of the detector for five minutes in order to obtain a spectrum. The detector system was then calibrated. The instrument was exposed to a drift error due to exposure to ambient temperatures. All *in situ* energy spectra were again calibrated individually to accommodate for said drift. During post calibration the energy peaks of the primordial radionuclides or a daughter radionuclide thereof were used. The energy peaks used were the 238.63 keV peak of ^{212}Pb , the 352 keV peak of ^{214}Pb , the 1460.75 keV peak of ^{40}K , and the 2614 keV peak of ^{208}Tl . The ^{214}Pb nuclide is a daughter of ^{238}U , whereas the ^{212}Pb and ^{208}Tl peaks are daughters of ^{232}Th . A quadratic relationship was used to relate the channel (Ch) to energy values (E) of each spectrum

$$E = a(Ch)^2 + b(Ch) + c \quad (3.1)$$

where a and b are the energy calibration coefficients and c the offset. The spectra were then converted to the counts per energy bin. In order to extract the radiation concentration levels Full Spectrum Analyses (FSA) were performed on the spectra.

The standard spectra were obtained by a process described by Bezuidenhout (2015a). A standard spectrum is an energy spectrum of one specific source (Noncolea 2011). Radiation calibration pads of the Nuclear Energy Corporation of South Africa (NECSA) were used as standard sources for calibration (Corner 1979). There are eleven circular calibration pads at NECSA with a 2 meter diameter, each consisting of a standard radiation source. Three pads containing mainly ^{40}K , ^{238}U and ^{232}Th were used for the calibration measurements. The first pad contained 4 400 ppm uranium oxide (U_3O_8), the second pad contained 14 200 ppm thorium oxide (ThO_2) and the third pad contained 12.2% potassium oxide

(K_2O). The detector was positioned in the middle of each of the calibration pads to record the calibration spectra. Each calibration spectrum was acquired for a period of ten minutes. The acquired spectra were representative of the counts per minute of the calibration pads. The count rate of the spectra was then converted to activity concentrations in Becquerel per kilogram (Bq/kg). The method to obtain the activity concentration of ^{40}K was slightly different to that of obtaining activity concentrations of ^{238}U and ^{232}Th as the amount of K_2O was provided in percentage, and that of U_3O and ThO_2 in parts per million (ppm) or grams per ton.

To determine the activity concentration of the ^{40}K nuclides in the 12.2% K_2O calibration pad the molar mass of K_2O in the calibration pad first needed to be determined. One mole is equal to Avogadro's number (N_A), which is 6.02214×10^{23} . One mole is based on the fact that 12 grams of Carbon (^{12}C) contains one mole ^{12}C atoms. The mass of a single ^{12}C atom can be calculated by dividing 12 grams of ^{12}C by N_A (Ohanian 1995). The compound concentration values for the calibration pads were provided in the NECSA tables (Corner et al. 1979). The molar mass of the potassium in K_2O was then calculated and converted to percentage of the total molar mass of K_2O in the calibration pad. The molar mass of ^{40}K was then calculated. The gamma emitting ^{40}K nuclide of naturally occurring potassium consists of only 0.0117% of the mass of potassium (CIAAW 2013). By using N_A it was possible to calculate the total number of molecules present in one kilogram of the compound. Because the percentages of potassium and ^{40}K were known, the number of atoms in one kilogram of the compound could be calculated. The decay constant (λ) was then calculated by introducing the half-life $T_{1/2}$ of ^{40}K and by re-writing Equation 2.2 as

$$\lambda = \frac{0.693}{T_{1/2}} \quad (2.2)$$

Then, by using Equation 2.3 for activity (R), the activity of ^{40}K radionuclides in the calibration pad could be calculated in Becquerel. The activity now represents the decays per second of the ^{40}K radionuclides in one kilogram of K_2O , however the concentration of K_2O in the calibration pad was only 12.2%. The activity concentration (A) must now be converted to Becquerel per kilogram by

$$A = \frac{R \times 12.2}{100} \quad (3.2)$$

As for ^{238}U and ^{232}Th , a slightly different procedure was followed. The same process as for ^{40}K was used to determine the percentage of ^{238}U and ^{232}Th in each of the ThO_2 , and U_3O_8 calibration pads. But, because the concentrations of ThO_2 , and U_3O_8 are provided in grams per ton (parts per million), the number of atoms of ^{238}U and ^{232}Th were calculated for one ton of the compound. The half-life of ^{238}U and of ^{232}Th were converted to seconds. Through using Equation 3.2 the decay constant for each was calculated. Equation 2.3 was then used to calculate the activity of ^{238}U and of ^{232}Th radionuclides for each of the specific calibration pads. The calculated activity was then converted from Becquerel per ton to Becquerel per kilogram. The detailed procedure followed for the activity calculations are indicated in Appendices B to D.

The spectra of ^{40}K , ^{238}U and ^{232}Th were now ready to be used in order to obtain standard spectra. The counts per energy bin were already calculated by means of equation 3.1. The next step was to normalise the counts per energy bin (C) to activity and time of the calibration spectra. The corrected count (C') was then determined by

$$C' = \frac{C}{AT_{live}} \quad (3.3)$$

where A is the activity in Bq/kg and T_{live} is the live time. The energy bins of the calibration spectra were then binned in 1 keV per bin starting at 331 keV and ending at 2800 keV by using Excel. An extract of the binned values is displayed in Appendix E. Energy bins below 331 keV demonstrated high levels of Compton scattering and photoelectric absorption and were therefore omitted. The peak with the highest emission energy was ^{232}Th with an energy peak at 2615 keV. Values above 2800 keV were thus not necessary to achieve a fit with the *in situ* spectra. Binning values for the corrected count rate per channel between two energy values were calculated via linear interpolation. Every energy bin between 331 keV and 2800 keV were now allocated a corrected count rate in Bq/s. The calibration spectra of ^{40}K , ^{238}U and ^{232}Th are now referred to as the standard spectra. They were used in FSA to extrapolate the activity concentrations of ^{40}K , ^{238}U and ^{232}Th from the *in situ* spectra.

FSA uses the concept of obtaining standard unitary spectra of ^{40}K , ^{238}U and ^{232}Th respectively. These standard spectra were then fitted to the *in situ* spectrum by adding each standard spectrum respectively. The FSA method described by Hendriks, Limburg & de Meijer (2001) and Newman et al. (2008) was followed. The FSA process follows the principle of producing a combined spectrum from standard

normalised spectra and fitting it to the spectrum of an unknown source. The first step in FSA was to import the data of the *in situ* spectra in the same manner as was done with the standard spectra. The *in situ* spectra were also then calibrated by employing Equation 3.1 in order to determine the count rate per energy bin. The next step was to normalise the counts per energy bin (C) of the *in situ* spectra to time by dividing the counts per energy bin with the live time of the *in situ* spectrum. The *in situ* spectra were also then binned in 1 keV per channel starting at 331 keV and ending at 2800 keV, and the corrected count rate per 1 keV was calculated via linear interpolation. A table was created in Excel with the standard normalised spectra and *in situ* spectrum data (see Appendix F). The standard normalised spectra were now added to form a combined spectrum (S). This combined spectrum was then fitted over the *in situ* spectrum (S'), by means of the following addition,

$$s_n = as_n^K + bs_n^{Th} + cs_n^U \quad (3.4)$$

where n varies from 331 to 2800 corresponding to the number of energy channels in keV, s_n is the n^{th} bin of the combined spectrum, s_n^K is the n^{th} bin standard normalised spectrum of ^{40}K , s_n^{Th} is the n^{th} bin standard normalised spectrum of ^{232}Th , and s_n^U is the n^{th} bin standard normalised spectrum of ^{238}U . The factors a , b , and c are varied in order to minimise the factors used to fit the standard normalised spectra to the *in situ* spectrum. The factors a , b , and c would then represent the concentrations of ^{40}K , ^{238}U and ^{232}Th present in the *in situ* spectrum measured in Bq/kg.

In this analyses a , b and c were manually fitted to achieve the best visual fit. The ^{232}Th peak at the energy of 2615 keV was first visually fitted by adjusting the value b in Equation 3.4. The ^{214}Bi peak, a daughter of ^{238}U , with an energy of 1764 keV was then adjusted by altering the value c in Equation 3.6. Once these two peaks were accepted as a good visual fit, value a in Equation 3.4 were altered to fit the ^{40}K peak at 1460 keV. Once an overall good visual fit was achieved, a mathematical minimum summed error (ϵ) was calculated by

$$\epsilon = \sum_{n=331}^{2800} \frac{(s'_n - s_n)^2}{s_n} \quad (3.5)$$

where n is the number of energy channels, s'_n is the *in situ* spectrum, and s_n is the combined spectrum. The smallest ϵ value was accepted as indication of the best fit. The values for a , b , and c were then taken

as the concentrations of ^{40}K , ^{238}U and ^{232}Th present in the *in situ* spectrum. An example of the procedure to obtain the best fit via FSA for one of the measurement positions is shown in Appendices G and H.

Radioactive decay is a stochastic process and all data will consequently have an associated statistical uncertainty. The statistical uncertainty was calculated by using the Poisson distribution statistical model as discussed in Section 2.3.2. Errors were estimated from 40 sample points that were systematically chosen from the measurement positions. Table 3.1 shows the chosen measurement positions with the errors in percentage, and live time that associated with each.

Table 3.1 An index of the selected measurement positions for error calculation, together with their error percentage and live time.

Measuremet Position	Error Percentage (%)	Live Time (s)
A01	18.86	724.53
A10	23.48	605.98
A19	23.11	756.03
B06	26.64	338.49
B15	26.13	354.37
C03	27.17	326.31
C12	25.66	332.04
D01	30.39	312.12
D10	22.89	320.12
D19	24.53	337.25
E06	18.80	339.91
E15	20.83	312.78
F03	26.39	331.12
F12	20.65	307.45
G02	24.52	360.85
G11	22.72	346.26
G20	21.22	332.25
H08	21.70	300.51
H17	18.43	374.29
J05	23.27	310.97
J14	19.37	325.40
K05	26.15	332.69
K14	22.82	295.76
L02	25.34	315.89
L11	18.38	351.56
L20	24.54	304.77
M08	21.17	323.62
M17	22.83	316.23
N05	27.70	388.39
N13	22.57	358.51
P01	22.25	338.11
P10	26.70	316.98
P19	24.53	307.23
Q07	30.37	316.38
Q16	23.62	310.97
R04	26.25	337.77
R13	29.32	313.65
R21	27.42	357.07
Average	23.91	

At first the standard deviation for the counts per spectrum channel (σ^{ch}) was calculated for ^{40}K , ^{238}U , ^{232}Th standard spectra. The energy bins per spectrum channel were already calculated using Equation 3.1. The standard deviations per channel of activity spectra (s^ε) were then calculated per energy bin, and normalised to activity and time by

$$s^\varepsilon = \frac{\sigma^{ch}}{AT_{live}} \quad (3.6)$$

where A is the activity in Bq/kg, T_{live} is the live time and σ^{ch} the standard deviation for the counts per spectrum channel. The same was done to calculate the standard deviation for the *in situ* spectrum (s'^ε) however activity was omitted from the equation. The standard deviations per 1 keV energy channel were also calculated from 331 keV to 2800 keV using linear interpolation between the energy bins from the activity spectra and *in situ* spectrum. The activity spectra are now referred to as the standard spectra.

The statistical uncertainty (A_i) per energy channel was then calculated by

$$A_i = \frac{s'^\varepsilon_n + s^\varepsilon_n}{s_n} \quad (3.7)$$

where s'^ε_n is the standard deviation of the *in situ* spectrum for energy channel n , s^ε_n is the standard deviation of the combined spectrum for energy channel n and s_n is the activity of the combined spectrum for energy channel n . The statistical uncertainty per energy channel was then converted to percentage (P) by

$$P = \frac{\sum A_i}{2470} \times 100 \quad (3.8)$$

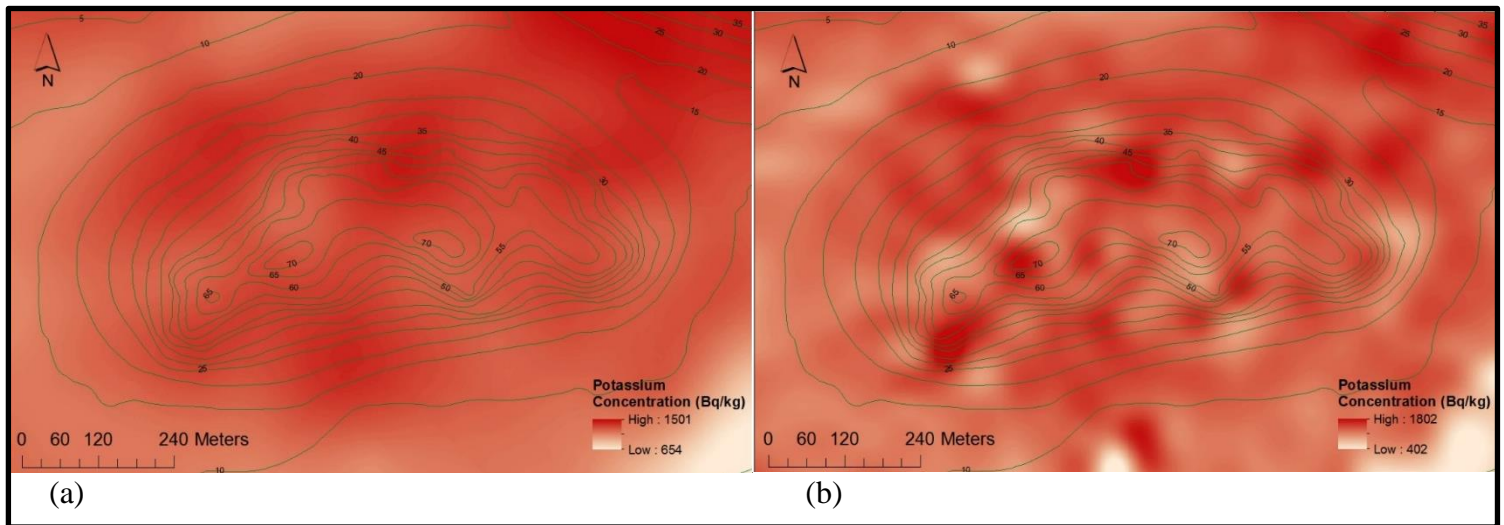
where 2470 is the number of energy channels used to plot the *in situ* and combined spectra. The average calculated statistical uncertainty for the 40 selected *in situ* spectra was 23.91%, as indicated in Table 3.1.

3.4 TECHNIQUES USED TO PREPARE DATA FOR QUALITATIVE ANALYSIS

The concentrations of the natural radionuclides in the soil were measured and mapped by means of *in situ* γ - ray photon measurements. The activity concentrations and actual positions of the measurements

were read into an Excel table once all measurements and calculations were completed. The table of the actual positions and activity concentrations is presented in Appendix A. This table was imported into ArcMap and was used to create radioelement maps for qualitative analysis. These radioelement maps will be presented and discussed in Chapter 4.

Once the table of activity concentrations was imported, the actual measurement positions were plotted. Each measurement position had associated ^{40}K , ^{238}U and ^{232}Th concentrations. Separate radioelement maps for ^{40}K , ^{238}U and ^{232}Th were constructed in ArcMap by using the activity concentrations associated with each measurement position. These radioelement maps were constructed in ArcMap through ordinary Kriging and thin plate splines, shown in Figures 3.7 (a) and (b).



Adapted from South Africa (1997)

Figure 3.7 A comparison between (a) ordinary Kriging and (b) thin plate splines of the ^{40}K concentration levels.

When Figures 3.7 (a) and (b) are compared, it can be seen that the ordinary Kriging image produces a smoother surface than that of thin plate splines. From Figure 3.7 (b) it can be seen that thin plate splines produces an image that displays the actual concentrations of the measurements. This provides a good indication of the outlying high and lower measurements, which potentially points to an existing anomaly. However, in terms of the research, ordinary Kriging was chosen as the interpolation method for creating radioelement maps as suggested by the IAEA (2003). Ordinary Kriging also provides a visual ‘smoothness’ of the image. The main reason for using ordinary Kriging is that it takes into account the stochastic nature of radioactive decay, superimposes it on the spatially dependent signal in the measurements during interpolation, and calculates new values for the measurement positions of which

thin plate splines are incapable of doing (IAEA 2003). The radioelement maps for ^{40}K , ^{238}U and ^{232}Th were then constructed by means of Kriging. These radioelement maps were then analysed using various GIS techniques. Qualitative data analysis of concentration levels of natural radiation and geographic factors were then used to research the influence of geographic factors on the distribution of natural radiation.

The raster calculator function in ArcMap was used to create a new raster layer as an experiment in order to identify areas where the predicted data differs from the actual data. This layer was created by subtracting the ordinary Kriging results from the thin plate splines. This process produced a raster that highlighted the areas that displayed some form of spatial irregularity with regards to respective data points. Once the raster results were calculated a standard descriptive statistics calculation was performed, in Excel, on each of the final concentrations of ^{40}K , ^{232}Th and ^{238}U . The standard deviation of each of ^{40}K , ^{232}Th and ^{238}U concentrations was then used as a standard statistical error in the data. Another raster was produced where the cells in the Kriging vs thin plate splines raster with the values equal to the standard deviation and less were assigned a null value. The remaining cells were allocated a specific colour. This procedure was done for ^{40}K , ^{232}Th and ^{238}U respectively. The final raster was produced in which the separate rasters of ^{40}K , ^{232}Th and ^{238}U were combined to form one raster.

Another method used to analyse the data was to compile rasters that indicated the ratio in concentrations between the three radionuclides. This was done with the raster calculator in ArcMap. The three ratios used in creating the new rasters were $^{232}\text{Th}/^{40}\text{K}$, $^{238}\text{U}/^{40}\text{K}$ and $^{238}\text{U}/^{232}\text{Th}$. The resultant layers and radioelement maps were used for further qualitative analysis.

A 5 meter contour map was also imported into ArcMap and then georeferenced (South Africa 1997). The contours and coastline of the research site were digitized and a digital elevation model (DEM) was created. The DEM was used to create a flow accumulation raster and a slope raster. The DEM was then imported into ArcScene to create a three-dimensional model of the area and, in conjunction with the radioelement maps, flow accumulation raster and slope DEM were used for further qualitative analysis. The 5 meter contour map was also used as an overlay on the radioelement maps to create new rasters. Experimental layers were created by clipping the data points above the 25 meter contour and running interpolation below that. These rasters were then compared to the original rasters for qualitative analysis. The 25 meter contour was chosen, as the majority of the granite outcrops were above the 25 meter contour line. This was done to remove the influence of the granite outcrops on the readings below the 25 meter

contour. This method did not render any notable differences from the original raster. All rasters created were also imported to Google earth for further qualitative analysis. A slope profile for the northern and southern slopes of Baviaansberg was also created. A total of five north-south transects were drawn across Baviaansberg. A north-south transect line was drawn through the middle of Baviaansberg from the position 33.03931°S and 17.91404°E to 33.0457°S and 17.91404°E. Two equally spaced north-south transects were drawn to the east and two to the west of the middle transect line. The distance between each line was 105.8 meters. Slope profiles of Baviaansberg were then created in ArcMap using the plotted transects. Data from the profile graphs were also exported to Microsoft Excel for better manipulation of the data. The northern and southern slope angles were then drawn from the 20 meter contour to the highest point closest to the edge of the crest of the hill profile. Respective slope angles were then calculated using trigonometry. An additional layer was created for human activities in order to compare the influence of human activities of the area to the various rasters. The human activity layer was created by means of identifying during fieldwork the areas of human influence, and by identifying those same areas on Google Earth. The types of human activity identified for the layer were roads, WWII buildings, a man-made platform and agricultural area. These activities were created as various layers in Google Earth. These layers were then exported to ArcMap and used for qualitative analysis of the research site.

3.5 RADIATION MEASUREMENT AND ANALYSIS ON BAVIAANSBERG

The research site, Baviaansberg, is a uniquely positioned area in terms of the impact of local geographic factors on this site. Its geographic position makes it possible for the researcher to focus mainly on the local geographic factors that influenced its rate of denudation and related soil formation and distribution. Soil formed from granite carries the same concentration of natural radionuclides. The γ - ray photon radiation signature from these natural radionuclides was measured by using a NaI(Tl) scintillation detector with a 7.62 x 7.62 cm crystal coupled to a scintiSPEC Multi-Channel Analyser (MCA). The detector and MCA was connected to a Trimble Yuma Rugged Tablet PC with WinTMCA32 software via USB connection. This detector system was used to collect radiation data from the research site. Data underwent radiation data analysis and were converted to activity concentrations of ^{40}K , ^{238}U , and ^{232}Th . These activity concentrations were then used to create radioelement maps, various rasters and GIS models for further qualitative analysis. Chapter 4 constitutes a discussion of the results of the data collection and analysis, with particular focus on how local geographic factors influence the distribution of concentrations of various natural radionuclides.

CHAPTER 4: THE INFLUENCE OF GEOGRAPHIC FACTORS ON THE DISTRIBUTION OF NATURAL RADIONUCLIDES

Radiation detection and mapping, as discussed in Chapter 3, constitute a useful method to measure the influence of geographic factors on the distribution of concentrations of natural radionuclides. This chapter will present the natural radionuclide concentration results as radioelement maps of ^{40}K , ^{232}Th and ^{238}U and variations thereof. These results will then be compared to the various geographic factors that impact the weathering and erosion of the research site. Comparisons will be done by utilising a slope raster, slope profiles, a flow accumulation raster, wind data, Google Earth images, a human activities map, a soil type map, a Spline vs Kriging raster, a Th vs K raster, a U vs K raster, and a U vs Th raster. The chapter will conclude with the analysis of alternative rasters created by subtracting the thin plate splines results from the Kriging results, as was discussed in Section 3.4.

4.1 DISTRIBUTION OF THE CONCENTRATION OF NATURALLY OCCURRING RADIONUCLIDES

A total of 336 measurements were recorded in the research site. The following section will discuss the results of these measurements in terms of the distribution patterns of ^{40}K , ^{232}Th and ^{238}U radionuclides in the research site.

4.1.1 Potassium distribution

^{40}K in its natural chemical arrangement is the most soluble of the three natural radionuclides, as deliberated in Section 1.3. Figure 4.1 is a histogram of the ^{40}K measurements collected in the research site. It is important to note the difference in the highest values and the lowest values between radioelement maps and histograms (Figures 4.1 to 4.6) for all three natural radionuclides. The reason for the difference in these values is that the values in the histogram represent the *in situ* readings, whereas the values in the radioelement map represent the Kriging interpolated data. It was decided that, according to Figure 4.1, low concentrations of ^{40}K would be values from the 25th percentile and lower, intermediate ^{40}K concentrations would range between the 25th and 75th percentile and high ^{40}K concentrations from the 75th percentile and higher. The values for low ^{40}K concentrations are from 1170 Bq/kg and lower, 1171 Bq/kg to 1366 Bq/kg for intermediate ^{40}K , and 1367 Bq/kg and higher for high ^{40}K concentrations.

The method for determining the high, intermediate and low values is the same as those described by Stanford School of Medicine (2004).

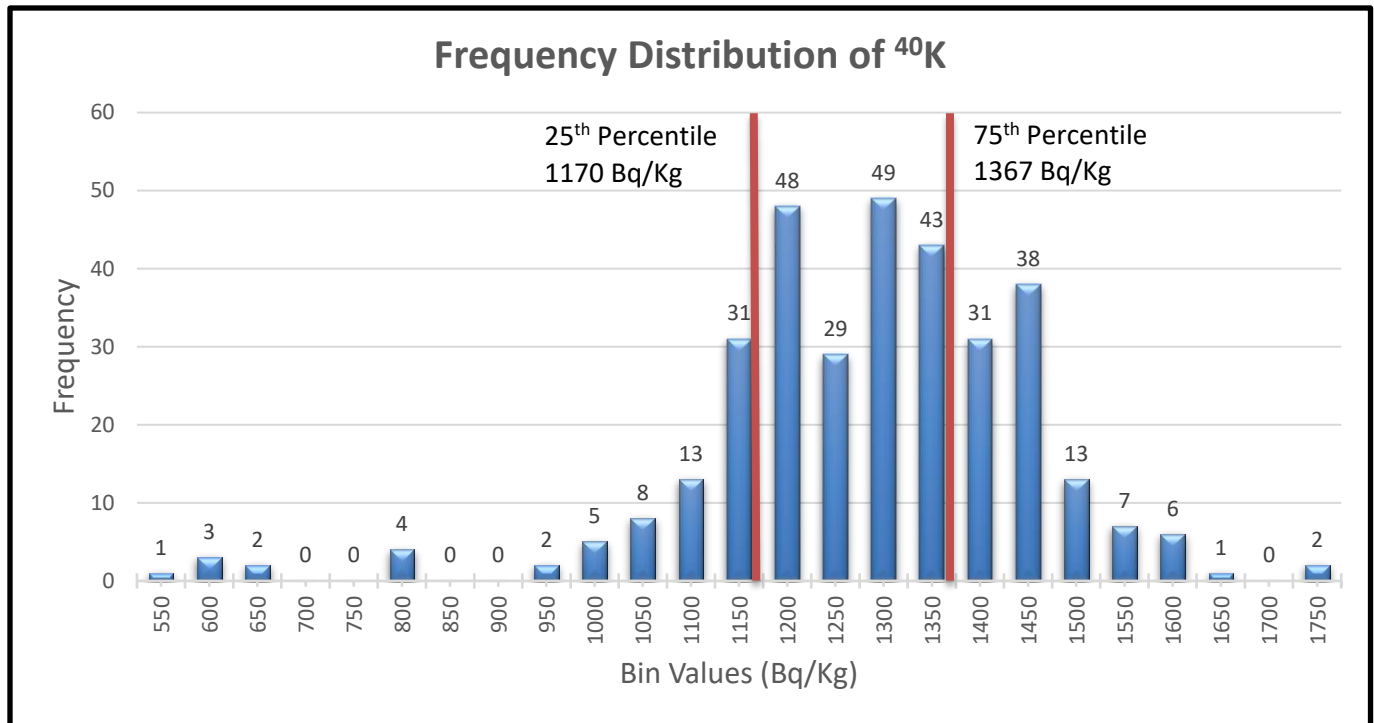
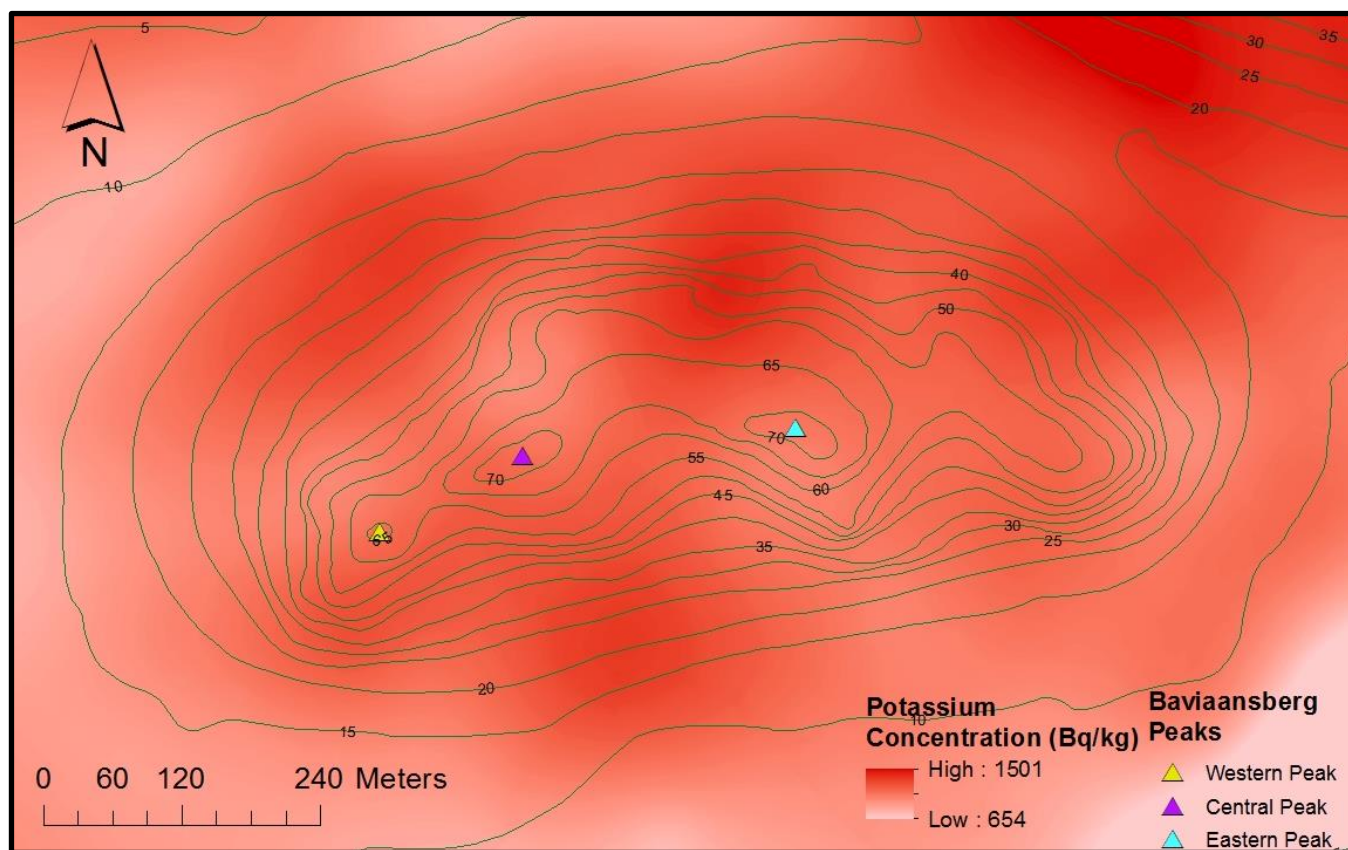


Figure 4.1 The ^{40}K concentration measurements. Red lines indicate the positions of the 25th and 75th percentiles.

Figure 4.2 illustrates the distribution of concentrations of ^{40}K in the research site. According to Figure 4.2, the highest ^{40}K concentrations of 1400 – 1501 Bq/kg are found in the north-eastern corner of the research site, north-east of the eastern peak of Baviaansberg. This area is situated between Baviaansberg and neighbouring Malgaskop. The lowest ^{40}K concentrations of 653.85 – 1030 Bq/kg are situated in the south-eastern corner of the research site, south-east of the eastern peak. There are also two areas on the northern slope of Baviaansberg that display higher ^{40}K concentrations of 1350 – 1450 Bq/Kg. One area is north north-east of the eastern peak and the other area north of the western peak. There is one area of higher ^{40}K concentrations of 1340 – 1400 Bq/kg, situated on the southern slope of Baviaansberg, south-east of the central peak. It is important to note the areas of lower ^{40}K concentrations. One area is situated on top of Baviaansberg between the three areas of higher concentrations, north of the western peak to north of the central peak. This area exhibits ^{40}K concentrations of 1199 – 1280 Bq/kg, which measures in the lower margins of the intermediate concentrations.



Adapted from South Africa (1997)

Figure 4.2 The distribution of ^{40}K concentrations as an overlay on the contour map of Baviaansberg. The ^{40}K concentrations differ between 654 Bq/kg and 1501 Bq/kg.

The cliff situated south south-east of the eastern peak exhibits ^{40}K concentrations of 1224 – 1266 Bq/kg. There is also an area exhibiting ^{40}K concentrations in the lower margins of the intermediate measurements of 1199 – 1235 Bq/kg on the eastern slope of Baviaansberg, east of the eastern peak. The area on the southern boundary of the research site, south south-west of the eastern peak, also shows lower ^{40}K concentrations of 1086 – 1184 Bq/kg. The area north west of the western peak on the north western boundary of the research site exhibits ^{40}K concentrations of 1134 – 1294 Bq/kg. It is important to note the general trend in distribution of ^{40}K concentrations on Baviaansberg, with the northern slope exhibiting more areas with higher ^{40}K concentrations, as well as generally higher ^{40}K concentrations than on the southern slope. There is also a gradual decrease in ^{40}K concentrations downslope from areas that exhibit higher ^{40}K concentrations. The differences in ^{40}K concentrations are attributed to the various geographic factors, which will be explained in Section 4.2.

4.1.2 Thorium distribution

According to Table 1.1, granite has higher concentrations of ^{232}Th in its natural chemical arrangement than most types of rock. ^{232}Th is also the least soluble of the three natural radionuclides (Al-Hilal & Al-Ali 2016), as was discussed in Section 1.3. Figure 4.3 indicates percentiles of ^{232}Th concentration measurements. The values in Figure 4.3 are also grouped into high, intermediate and low values. The exact same method was used as that discussed in Section 4.1, through which measured values were plotted in a histogram and then divided into percentiles. According to Figure 4.3 low ^{232}Th concentrations are from the 25th percentile and lower, 43 Bq/kg and lower. Intermediate ^{232}Th concentrations range between the 25th and 75th percentiles, 44 – 73 Bq/kg. High ^{232}Th concentrations are from the 75th percentile and higher, that is 74 Bq/kg and higher.

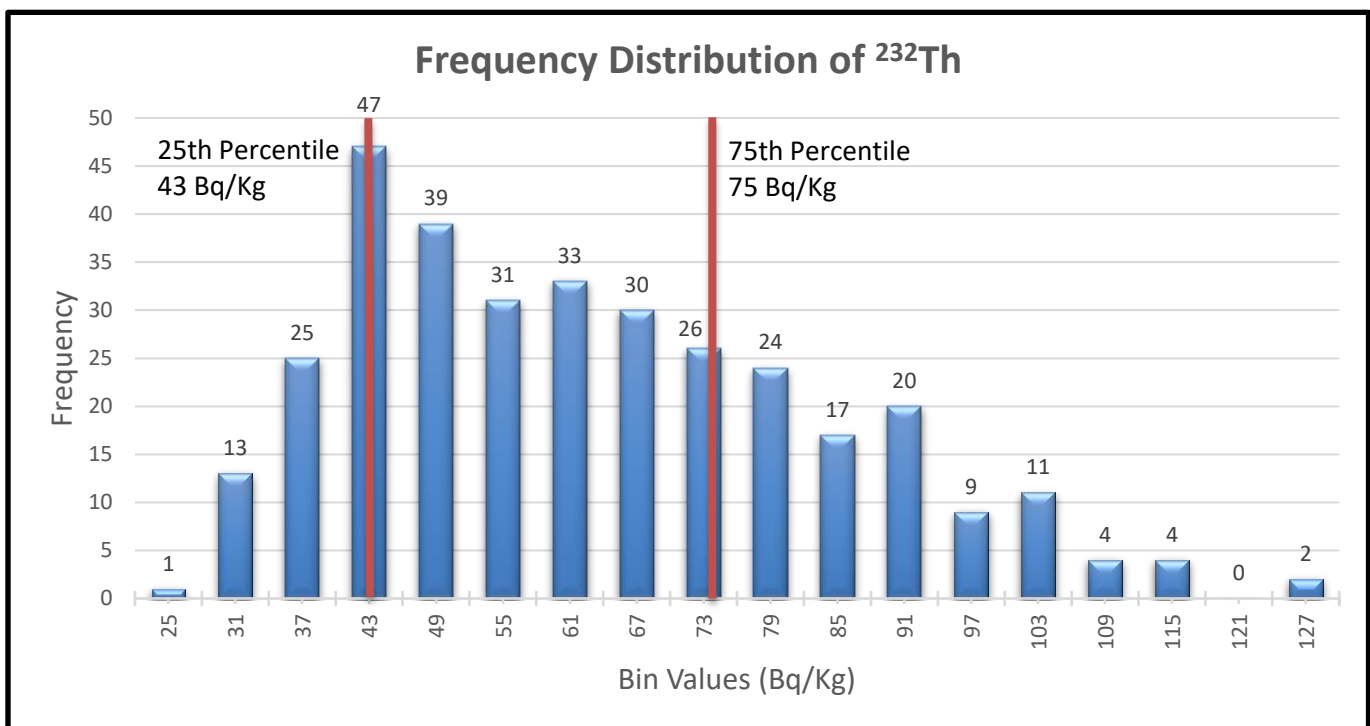
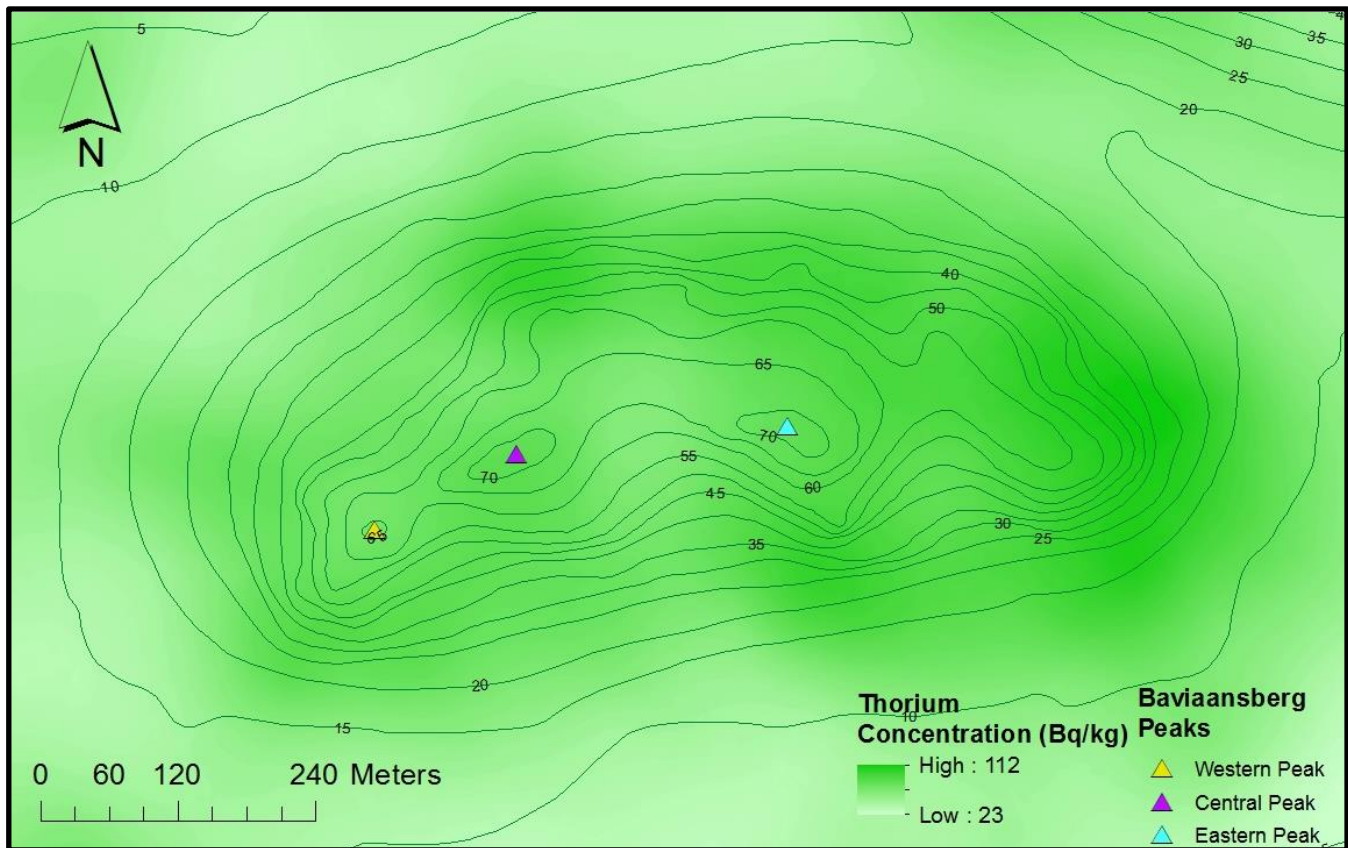


Figure 4.3 The ^{232}Th concentration measurements. Red lines indicate the positions of the 25th and 75th percentiles.

Figure 4.4 is a radioelement map that indicates the spread of concentrations of ^{232}Th across the research site. In Figure 4.4 the areas of high ^{232}Th concentrations (80 – 112 Bq/kg) are situated on the northern, eastern and north-eastern slopes of Baviaansberg. These areas are north of the central peak, from directly north of the eastern peak to east south-east of the eastern peak, and south south-east of the eastern peak.

There are areas of intermediate to high ^{232}Th concentrations, 71 – 81 Bq/kg, on the south-western and western slope, that is south of the central peak to west north-west of the western peak. Lower concentrations, 23 – 63 Bq/kg, are all situated downslope from the 15 meter contour.



Adapted from South Africa (1997)

Figure 4.4 The distribution of ^{232}Th concentrations as an overlay on the contour map of Baviaansberg. The ^{232}Th concentrations differ between 23 Bq/kg and 112 Bq/kg.

Two areas on Baviaansberg exhibit intermediate ^{232}Th concentrations that are lower than the surrounding ^{232}Th concentrations. The first area is the valley in the centre of the southern slope, south east of the central peak, with concentrations of 59 – 70 Bq/kg. The second area is situated on the north western slope, north north-west of the western peak, with concentrations of 43 – 72 Bq/kg. Differences in ^{232}Th concentrations are attributed to various geographic factors that will be explained in Section 4.2.

4.1.3 Uranium distribution

The distribution patterns of the ^{238}U concentrations show similar trends to the distribution pattern of ^{232}Th concentrations. However, there are some differences; ^{238}U is slightly more soluble in its natural chemical arrangement than ^{232}Th (Van der Graaf et al. 2007; Al-Hilal & Al-Ali 2016). Figure 4.5 is a histogram that indicates the percentiles of ^{238}U concentration measurements. The same method was used as that described in Section 4.1 to determine the range in values of high, intermediate and low ^{238}U concentrations.

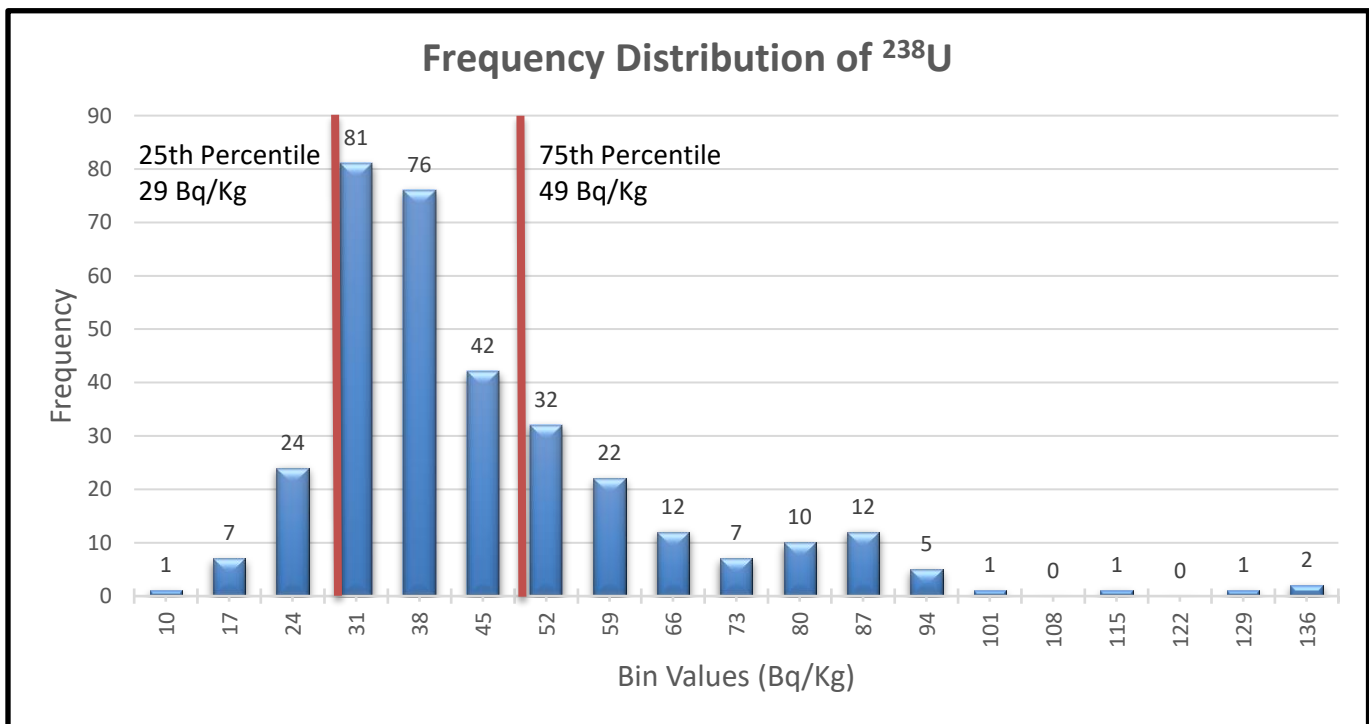
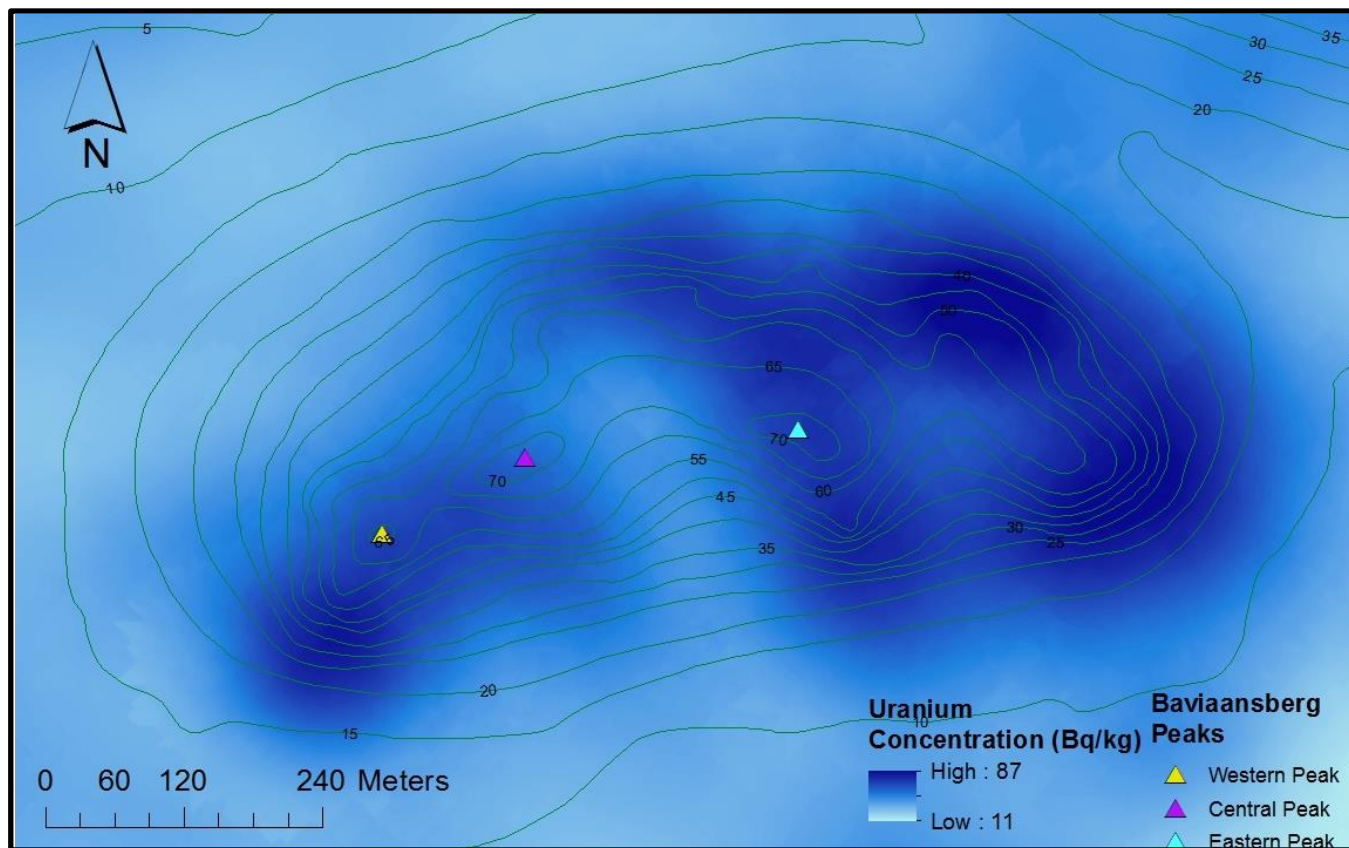


Figure 4.5 The ^{238}U concentration measurements. Red lines indicate the positions of the 25th and 75th percentiles.

According to Figure 4.5, low ^{238}U concentrations are from the 25th percentile and lower, 29 Bq/kg and lower. Intermediate ^{238}U concentrations range between the 25th and 75th percentiles, 30 – 48 Bq/kg. High ^{238}U concentrations are from the 75th percentile and higher, that is 49 Bq/kg and higher. Figure 4.6 portrays the radioelement map of the research site that indicates the spread of concentration of ^{238}U radionuclides across the research site. The higher ^{238}U concentrations, 53 – 87 Bq/kg, are situated on the northern, eastern, south-eastern and south-western slopes of Baviaansberg. These areas are from north north-west to south south-east of the eastern peak, as well as south south-west of the western peak.



Adapted from South Africa (1997)

Figure 4.6 The distribution of ^{238}U concentrations as an overlay on the contour map of Baviaansberg. ^{238}U concentrations differ between 11 Bq/kg and 87 Bq/kg.

The lower to intermediate ^{238}U concentrations, 11 – 33 Bq/kg, are all situated around Baviaansberg from the 15 meter contour downslope. There are two exceptions. The first exception is in the north-east corner of the research site, north-east of the eastern peak. This area is situated between Baviaansberg and the neighbouring Malgaskop and exhibits intermediate ^{238}U concentrations of 35 – 44 Bq/kg. The second exception is the valley in the middle of the southern slope, east to south-east of the central peak, and exhibits intermediate ^{238}U concentrations of 37 – 43 Bq/kg. The differences in ^{238}U concentrations are attributed to the various geographic factors, which will be explained in Section 4.2.

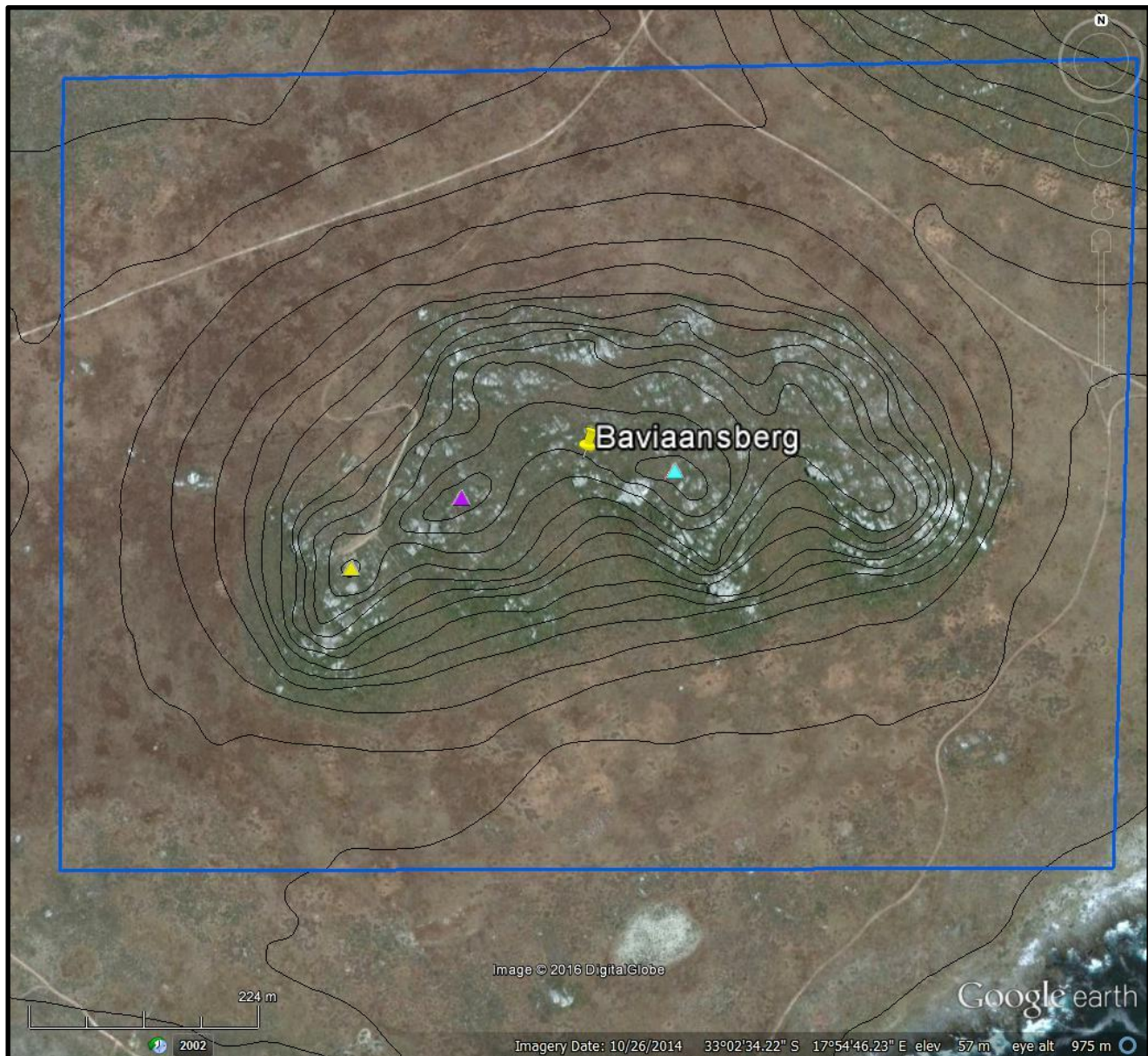
4.2 RELATIONSHIP BETWEEN NATURAL RADIONUCLIDE CONCENTRATIONS AND PHYSICAL GEOGRAPHIC FACTORS

Geology, climate, topography, biology, time and human impact were the factors identified as having a potential influence on the distribution of the natural radionuclide concentrations in a specific area. For

this study, the factors reported on were geology, slope, soil type, hydrological impact, aeolian impact and human impact. These factors are discussed as such in the following sections.

4.2.1 Geology

Granite outcrops on Baviaansberg are concentrated upslope from the 15 meter contour. Figure 4.7 indicates the positions of all the granite outcrops within the research site.



Source: Adapted from South Africa (1997)

Google Earth (2016)

Figure 4.7 A Google Earth image of the research site. The blue rectangle demarcates the research site and the black lines are the contour lines. The yellow triangle identifies the western peak, the pink triangle

the central peak and the turquoise triangle the eastern peak of Baviaansberg. The white to light grey markings on Baviaansberg upward from the 15meter contour and upslope thereof indicate granite outcrops.

Granite, in general, bears the highest concentrations of natural radionuclides of most rocks, as indicated in Table 1.1. Figure 4.8 (a) to (d) is a comparison of ^{40}K , ^{232}Th and ^{238}U to the location of the granite outcrops of Baviaansberg whereby the higher concentrations of ^{40}K , ^{232}Th and ^{238}U are revealed as situated on and around the areas with the greater concentrations of granite outcrops.

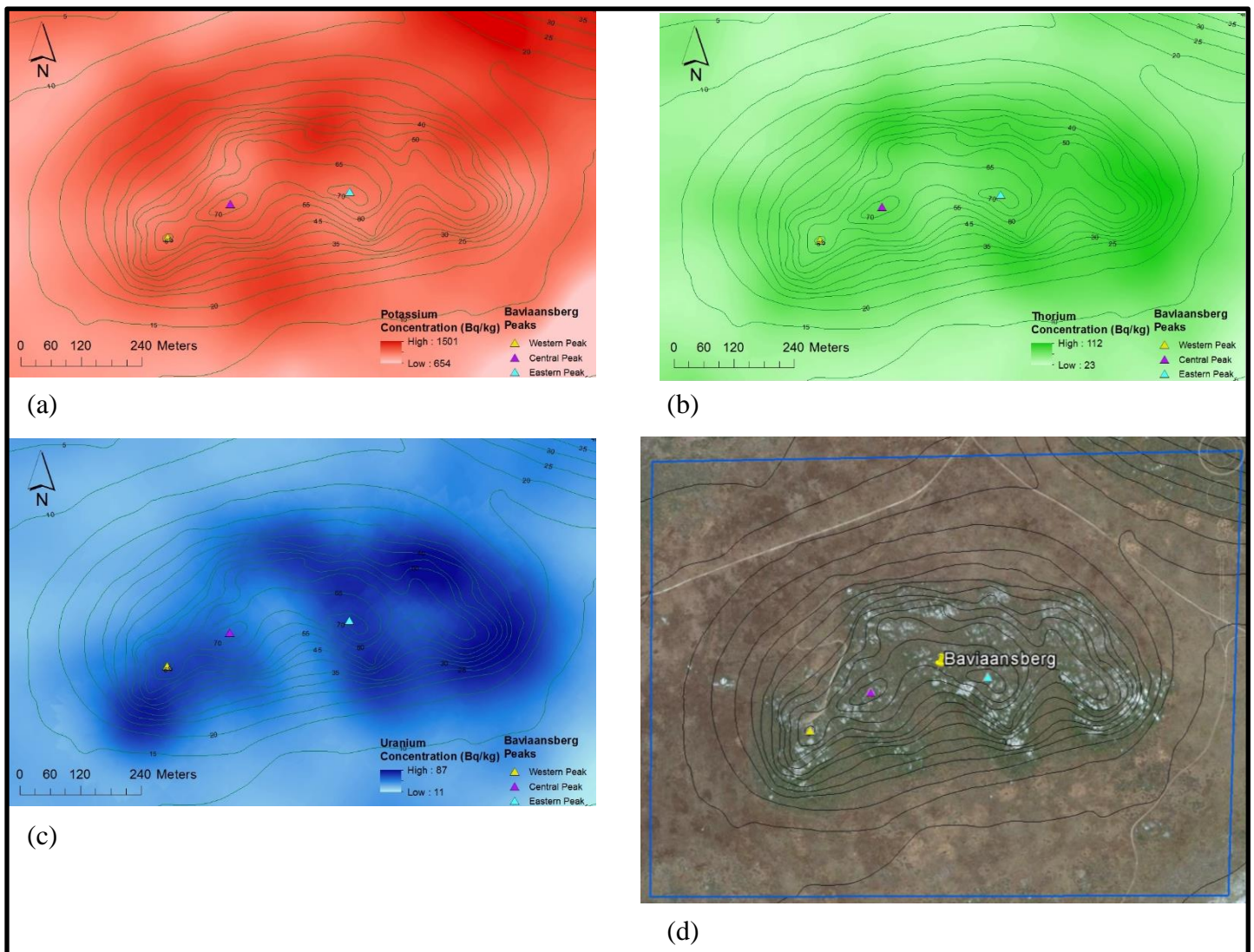


Figure 4.8 (a) – (d) A comparison between the (a) ^{40}K , (b) ^{232}Th and (c) ^{238}U concentrations and (d) the granite outcrops of Baviaansberg.

Soil originating from these granite outcrops should also then bear a radiation signature of similar concentrations as the granite outcrops (Ramli 1997) from Baviaansberg, as was discussed in Section 2.2.3. Results from this research indicate that the highest concentrations of ^{40}K , ^{232}Th and ^{238}U are measured on and around the granite outcrops, which supports the research of Ramli (1997). This supports the proposition that the geology of an area influences the radiation signature of the parent material directly, which again affects the natural radionuclide concentrations of the soil.

4.2.2 Slope

For the purpose of this study, slope was the main topographic factor that was considered as a potential influence on the distribution of natural radionuclides. Slope influences the movement of water and the movement of particles under the influence of gravity. Thus, the discussion of slope will incorporate these influences. Other influential factors, such as drainage patterns and aspect, which also form part of topography were incorporated under the discussions on hydrological and aeolian impacts. Slope of a terrain influences the rate of erosion and mass wasting (Hess 2014), which then influences the distribution patterns of soil that in turn influences the distribution patterns of the concentrations of natural radionuclides. The steep slopes of Baviaansberg are the areas where the granite outcrops occur. This can be seen when Figure 4.9 (b) and (c) are compared.

In Figure 4.9 (b) it can be seen that the slopes of Baviaansberg range from 0 to 50 degrees. The range of the slopes was divided into three equal zones: steep slope, intermediate slope and gentle slope. This was done to facilitate discussion in terms of the influence of the type of slope on the distribution of natural radionuclides. The demarcation of the zones was performed by dividing the range of the slopes into three areas equal in steepness. The areas represented by dark to light green in Figure 4.9 (b) indicate areas of gentle slope of $0^{\circ} - 16^{\circ}$, the yellow to orange sections indicate areas of intermediate slope $17^{\circ} - 33^{\circ}$ and the red sections indicate areas of steep slope of $34^{\circ} - 50^{\circ}$. The specific raster has a spatial resolution of 8.5 meters.

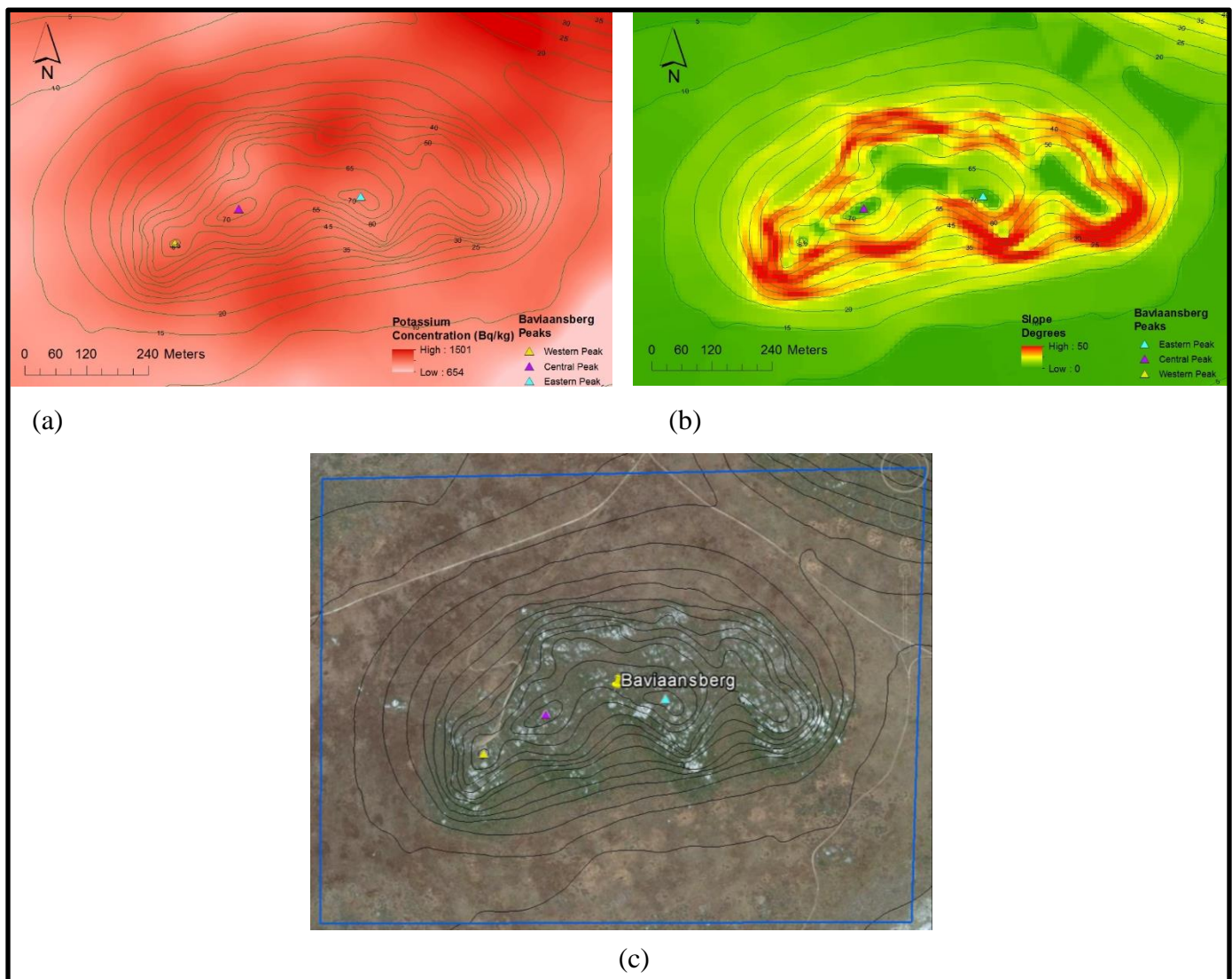


Figure 4.9 (a) – (c) A comparison between the (a) ^{40}K concentrations, (b) slope raster and (c) granite outcrops of Baviaansberg.

When comparing the ^{40}K concentrations in Figure 4.9 (a) to the slope raster of Figure 4.9 (b), it is seen that the areas of higher ^{40}K concentration are situated directly below the areas of steep slope. These areas coincide with areas directly below the granite outcrops, as seen in Figure 4.9 (c). The reason for the higher ^{40}K concentrations in these areas is the fact that the weathered granite particles concentrate directly below the granite outcrops (Hess 2014). These weathered particles contain ^{40}K radionuclides, and accumulate at the bottom of the granite outcrops. The accumulation of particles around granites increases the amount of ^{40}K radionuclides in the surrounding soils. This accumulation in turn increases the concentrations of ^{40}K . The larger weathered particles will be situated close to their parent material, thus

providing the soil closer to the parent material with virtually the same radiation signature as the parent material.

As the distance away from parent material increases, the size of the weathered particles decreases. Once water is added by means of overland flow, the smallest weathered particles will end up in solution and suspension and will be transported further away, hence the gradual decrease of ^{40}K concentrations downslope from the granite outcrops (Marshak 2001). As smaller weathered particles containing ^{40}K radionuclides are removed by overland flow, they become more dispersed, thus leading to a further decrease in ^{40}K concentrations. The northern slope of Baviaansberg shows a greater number of areas of high ^{40}K concentrations in comparison to the southern slope, as supported by data in Figure 4.9 (a). The southern slope is steeper than the northern slope (see Figure 4.9 (b)). Overland flow on the southern slope will thus occur faster than on the northern slope due to the difference in steepness. Slower overland flow causes the deposition of particles from the overland flow to occur closer to the parent material (Hess 2014), and at a more regular rate on the northern slope than on the southern slope. Deposition of particles containing ^{40}K radionuclides on the northern slope will occur closer to the parent material and at more regular intervals, as is shown in Figure 4.9 (a). Results from this research indicate a possible relationship between slope and the spread of ^{40}K concentrations. This relationship corroborates the work done by Marshak (2001) and Hess (2014)

Granite naturally has higher concentrations of ^{232}Th (Sharma 1997), which in turn causes the soil surrounding the granite to bear the same level of ^{232}Th concentrations. This can be seen where the steep slopes of Baviaansberg correspond to the areas of higher ^{232}Th concentrations as compared in Figures 4.10 (a) and (b).

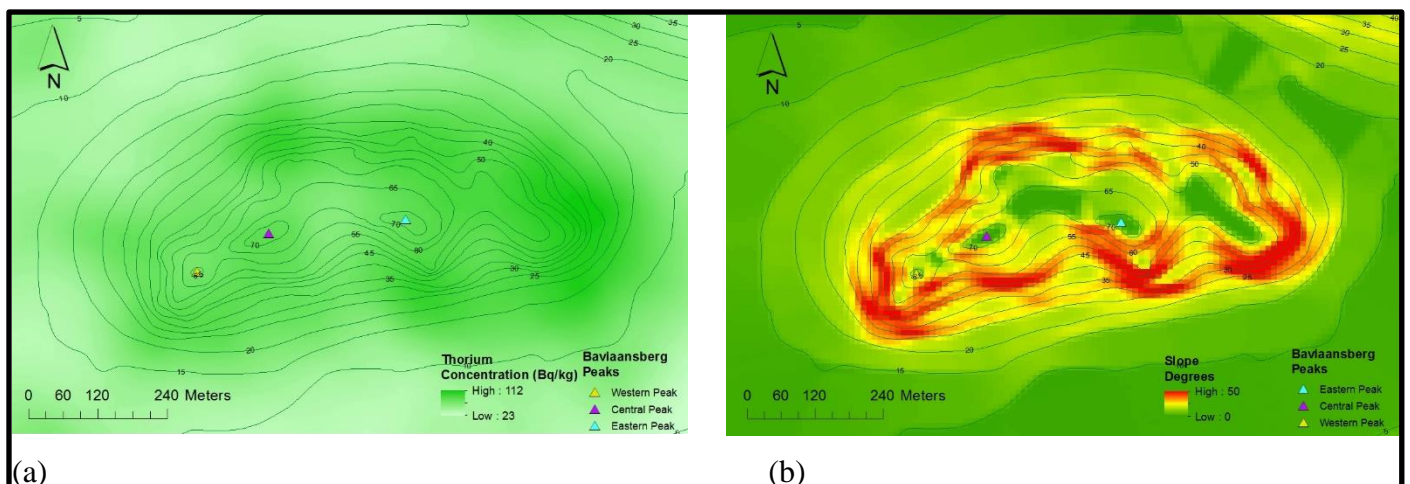


Figure 4.10 (a) – (b) A comparison between the (a) ^{232}Th concentrations and (b) slope raster.

As mentioned earlier, the areas of steep slope are associated with granite outcrops. From these outcrops the granites are weathered and eroded and the smaller pieces of granite containing ^{232}Th radionuclides are removed from the parent material. As these weathered particles are removed from the parent material they are dispersed over a greater area. This in turn causes a decrease in the ^{232}Th concentrations, as shown in Figure 4.4.

The ^{238}U concentration distribution pattern is similar to the distribution pattern of ^{232}Th concentrations. Figures 4.11 (a) and (b) is a comparison between ^{238}U concentrations and slope, it points to the areas of higher ^{238}U concentrations also correspond to the areas of steep slope and granite outcrops.

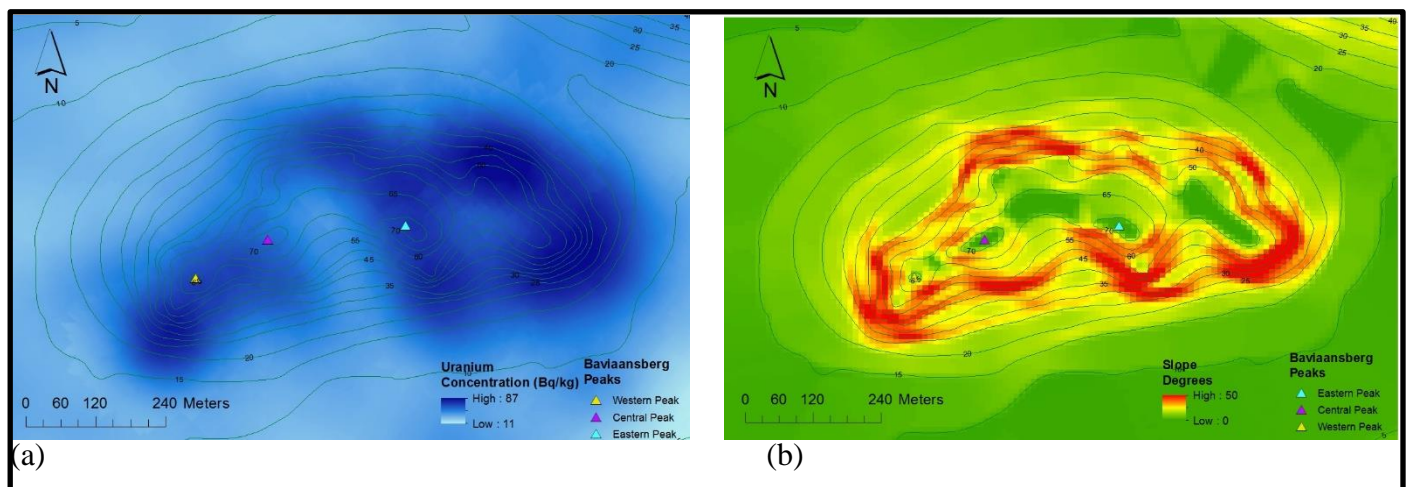
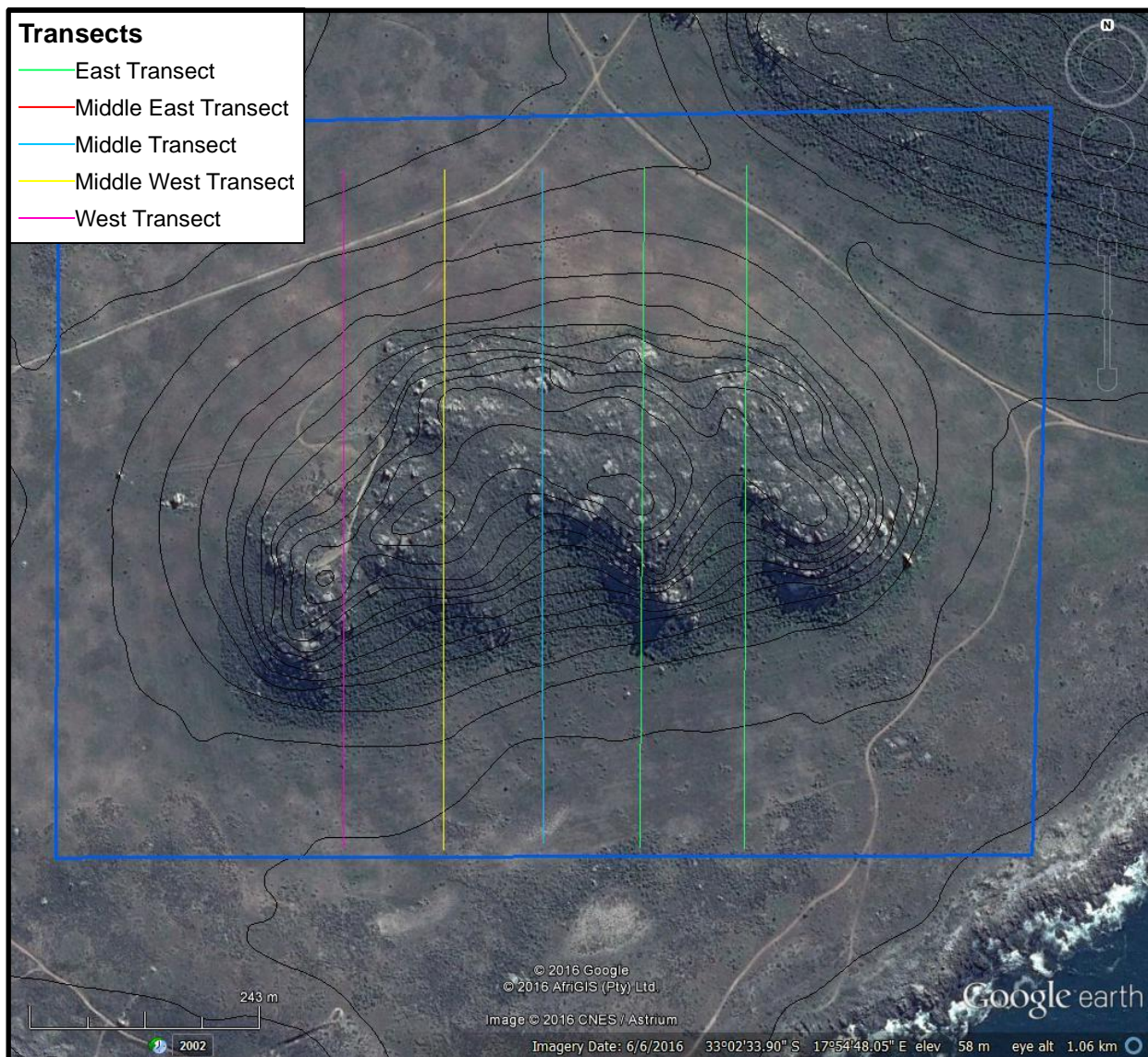


Figure 4.11 (a) – (b) A comparison between the (a) ^{238}U concentrations and (b) slope raster.

The distribution pattern of ^{238}U concentrations also follow the same principles as that of ^{232}Th concentrations. Granite outcrops are weathered and eroded and the larger pieces of weathered material stays the closest to these granite outcrops, whereas smaller granite particles containing ^{238}U radionuclides are removed further away from their parent material. Smaller particles containing ^{238}U radionuclides are dispersed over a greater area, thus decreasing the ^{238}U concentrations downslope away from the parent material. The only notable difference in the distribution patterns of ^{238}U and ^{232}Th is in the valley of the southern slope of Baviaansberg, east to south-east of the central peak. The valley portrayed in Figure 4.11 (a) shows a greater decrease in ^{238}U concentrations than that of ^{232}Th concentrations. This means that ^{238}U radionuclides are removed from the soil easier than ^{232}Th radionuclides, as supported by Ruffel et al. (2006) and Al-Hilal & Al-Ali (2016). The slope raster also reveals that the southern slope contains the majority steep slope areas, as confirmed by slope profiles created from the five transects drawn across Baviaansberg (Figure 4.12).



Source: Adapted from South Africa (1997)
Google Earth (2016)

Figure 4.12 A Google Earth image of the study area that indicates the positions of the transects used to determine the slope profile of Baviaansberg

Figure 4.13 (a) to (e) are the resultant slope profiles from the transects of Figure 4.12. The southern slope of Baviaansberg has an overall steeper profile than the northern slope. This is noticeable when comparing the various slope profiles of Baviaansberg in Figure 4.13 (a) to (e).

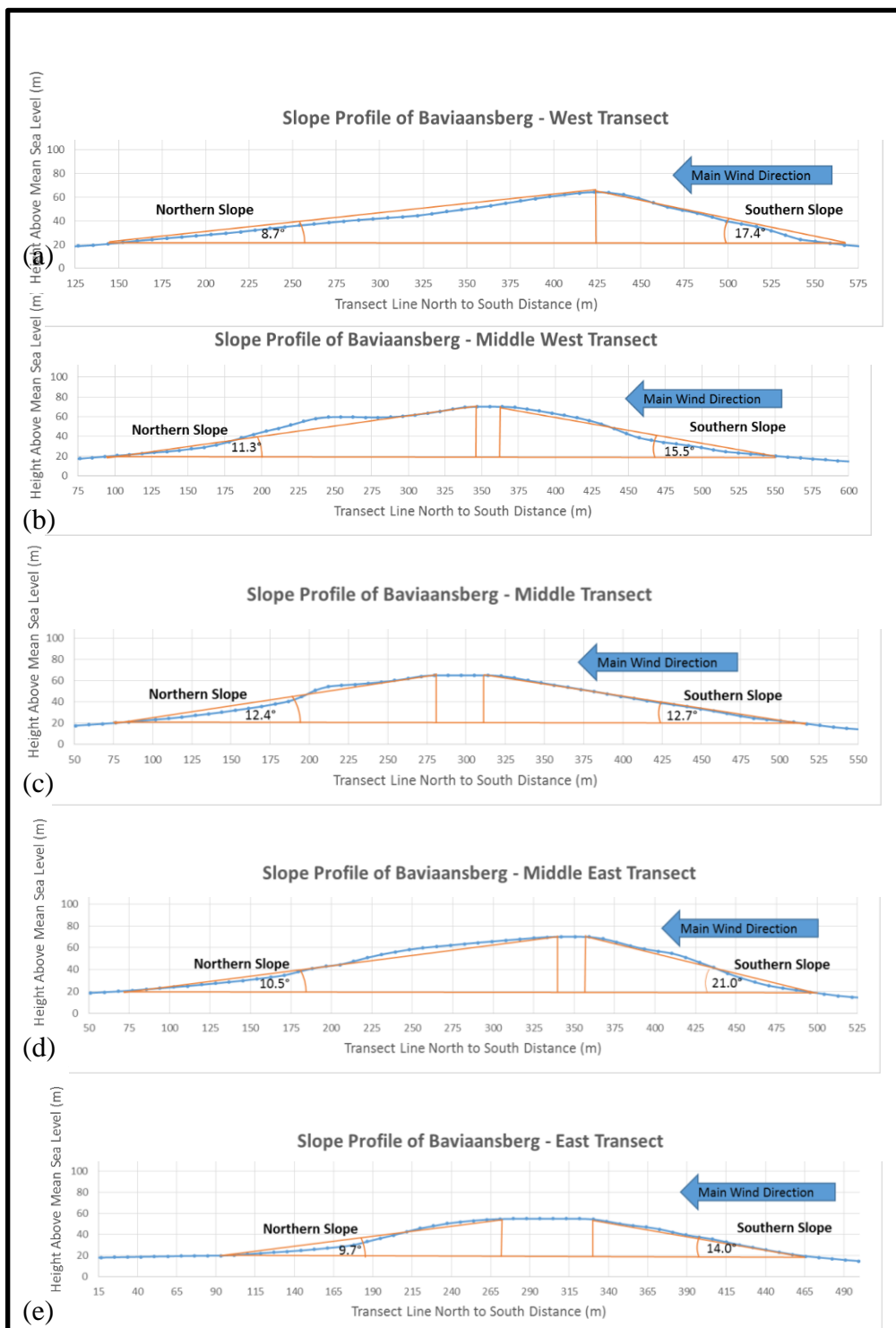


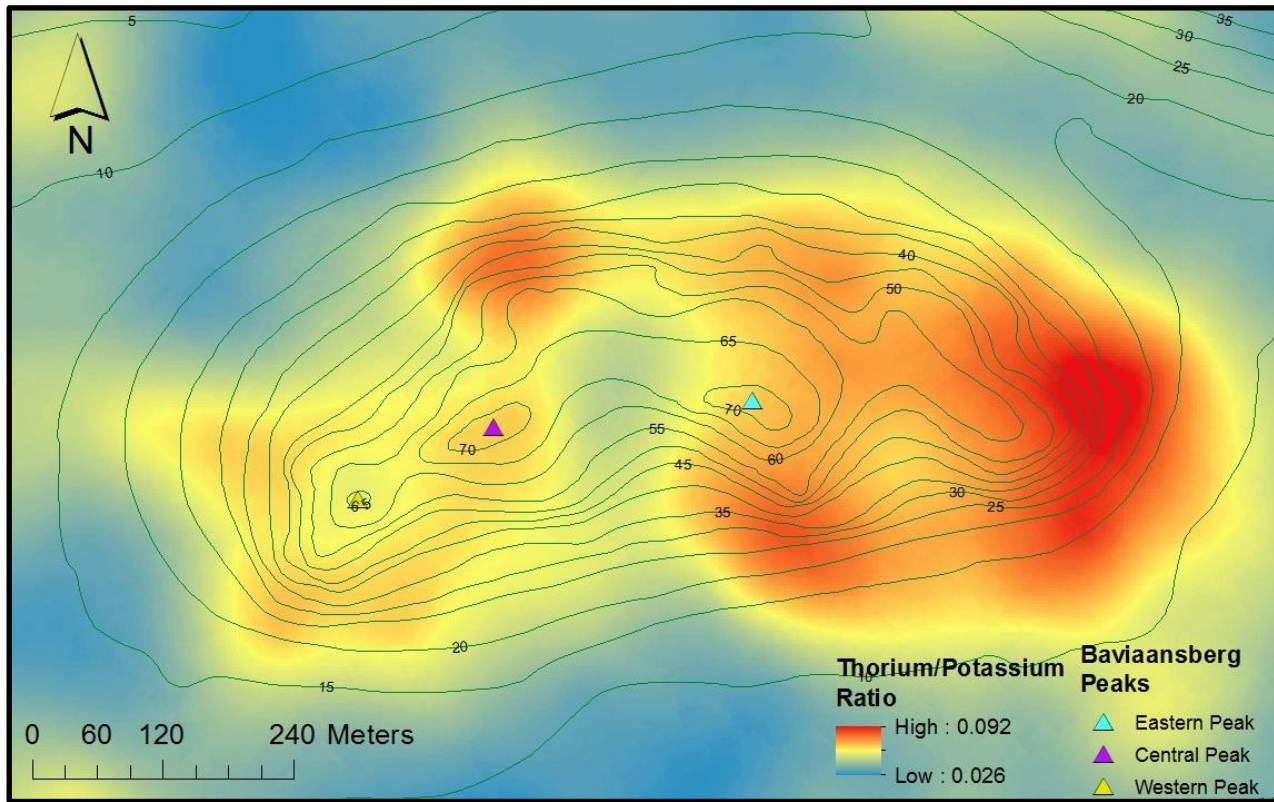
Figure 4.13 The slope profile of Baviaansberg.

Figure 4.13 (a) profiles the slope of the western transect. It shows a northern slope angle of 8.7° and a southern slope angle of 17.4° . Figure 4.13 (b) shows the profile of the transect between the middle and western transect, and displays a northern slope angle of 11.3° and southern slope angle of 15.5° . Figure

4.13 (c) is the profile of the middle transect and shows a northern slope angle of 12.4° and a southern slope angle of 12.7° . Figure 4.13 (d) is the profile of the transect between the middle and eastern transect and shows a northern slope angle of 10.5° and southern slope angle of 21° . Figure 4.13 (e) is the profile of the eastern transect and shows a northern slope angle of 9.7° and a southern slope angle of 14° .

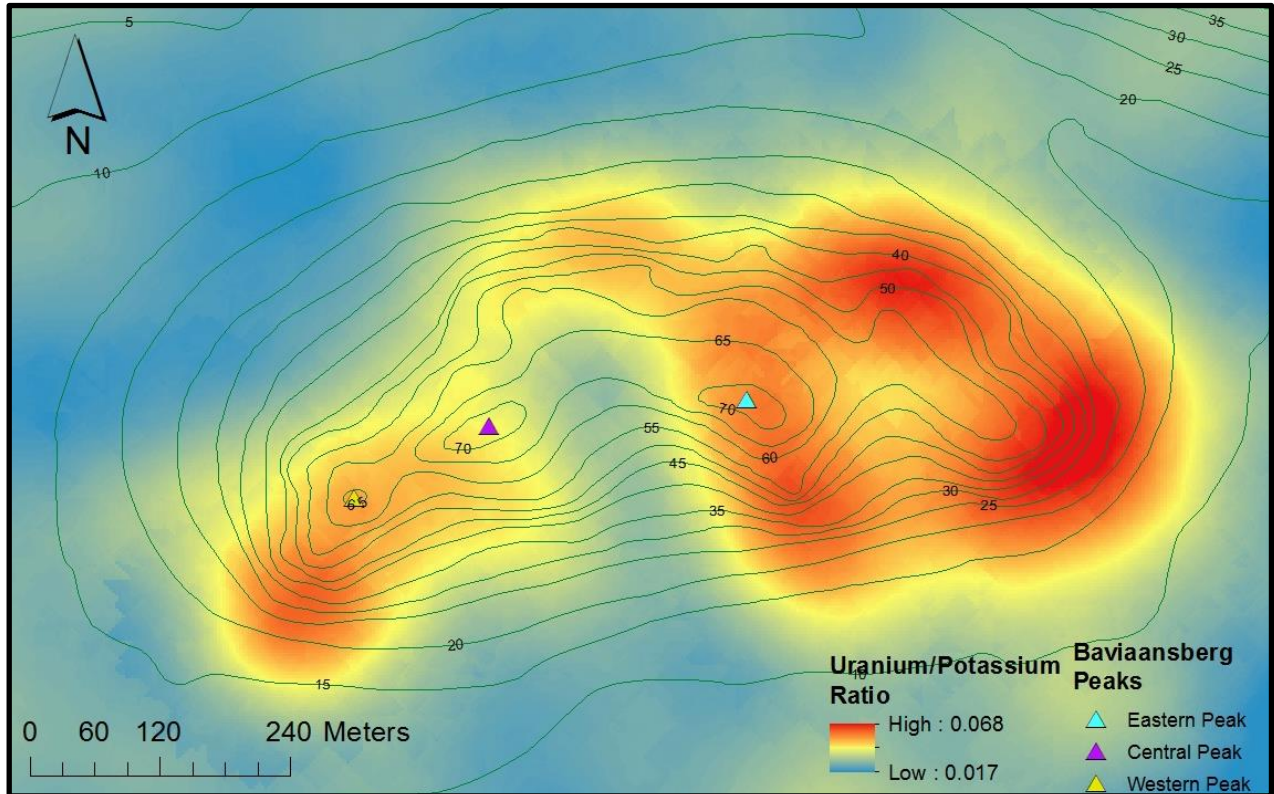
From Figure 4.7 it can be seen that the southern slope houses more granite outcrops than the northern slope. This explains the relationship between the highest ^{40}K , ^{238}U and ^{232}Th concentrations and granite outcrops as per the comparison of Figure 4.8 (a) – (d). In Figure 4.8 (a) the southern slope shows greater ^{40}K concentrations than the northern slope. This is probably due to slope steepness, as Figure 4.13 illustrates that the southern slope is steeper than the northern slope. The northern slope that is less steep than the southern slope causes any overland flow to slow down quicker. This causes greater deposition of ^{40}K particles in suspension, in turn leading to more areas of higher ^{40}K concentrations closer to the parent material, as is evidenced in Figure 4.8 (a). This again is an indication that ^{40}K is the most soluble of the three natural radionuclides.

The southern slope of Baviaansberg houses more areas of high ^{232}Th and ^{238}U concentrations than the northern slope (Figures 4.8 (b) and (c)). It indicates once more that ^{232}Th and ^{238}U are less soluble than ^{40}K . In this case the ^{40}K radionuclides are removed more readily from the steeper southern slope than from the northern slope, leaving behind more ^{232}Th and ^{238}U radionuclides. These findings are verified by Figures 4.14 and 4.15. Figure 4.14 shows the ratio of ^{232}Th to ^{40}K in the research site, and Figure 4.15 the ratio of ^{238}U to ^{40}K . When these two figures are compared, it appears that the high ratios of ^{232}Th to ^{40}K are spread over a larger surface area than the ratio of ^{238}U to ^{40}K as ^{238}U will be removed more regularly from granite outcrops. This causes the ^{238}U to be spread over a larger area than ^{232}Th . This in turn causes a greater concentration of ^{232}Th radionuclides around the granite outcrops compared to ^{238}U radionuclides. These results also support the work of Ruffel et al. (2006) and Al-Hilal & Al-Ali (2016) through which ^{238}U is reported to be more soluble than ^{232}Th .



Adapted from South Africa (1997)

Figure 4.14 An illustration of the ratio of the distribution of ^{232}Th to ^{40}K concentrations as an overlay on the contour map of Baviaansberg.

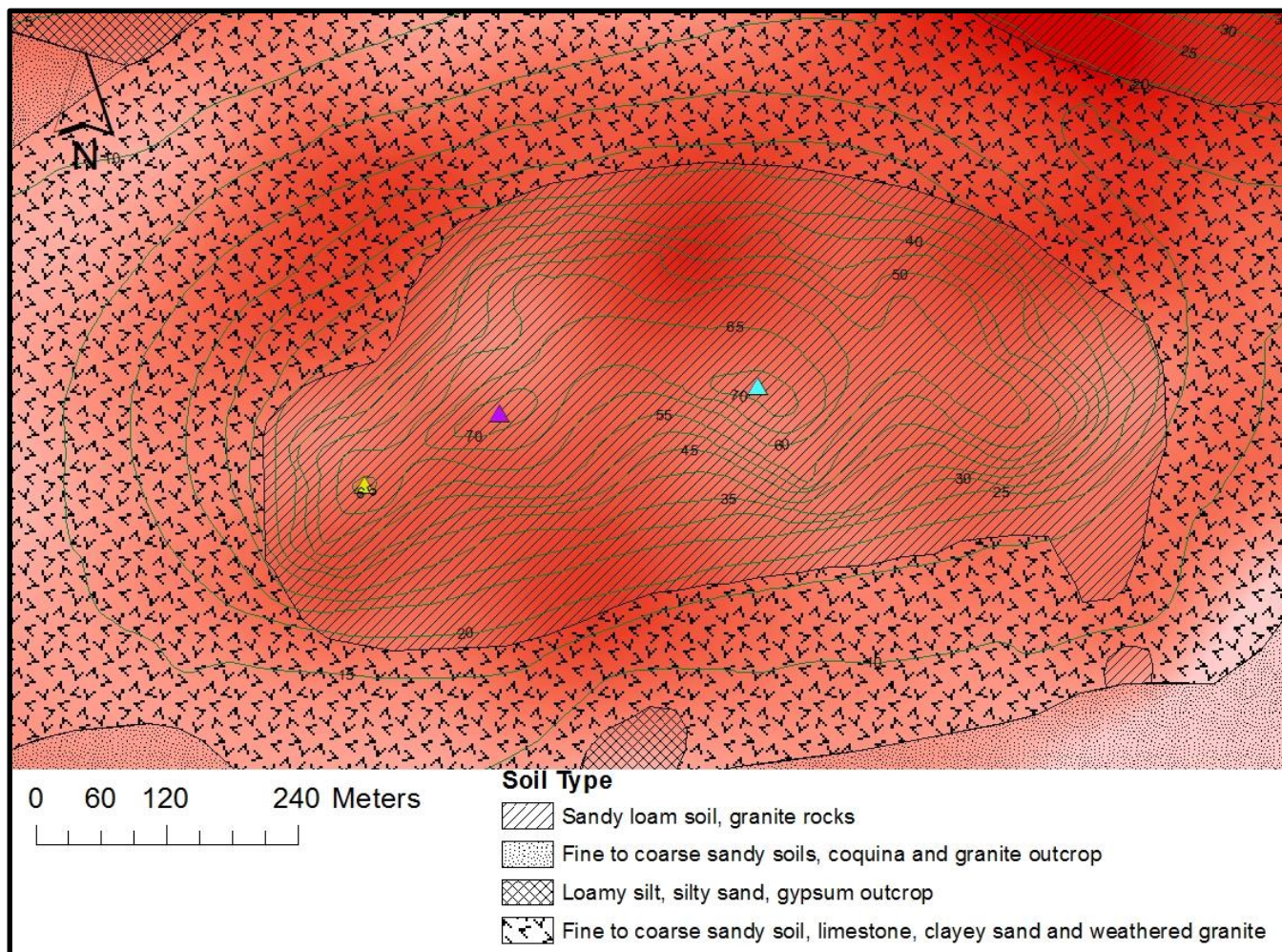


Adapted from South Africa (1997)

Figure 4.15 An illustration of the ratio of the distribution of ^{238}U to ^{40}K concentrations as an overlay on the contour map of Baviaansberg.

4.2.3 Soil type

Ramli (1997) found that soil type determines the level of natural radionuclide concentrations present in soil. The soil layer classified as ‘fine to coarse sandy soils, coquina and granite outcrop’ is associated with lower concentrations of ^{40}K , ^{232}Th and ^{238}U , as seen in Figure 4.16.

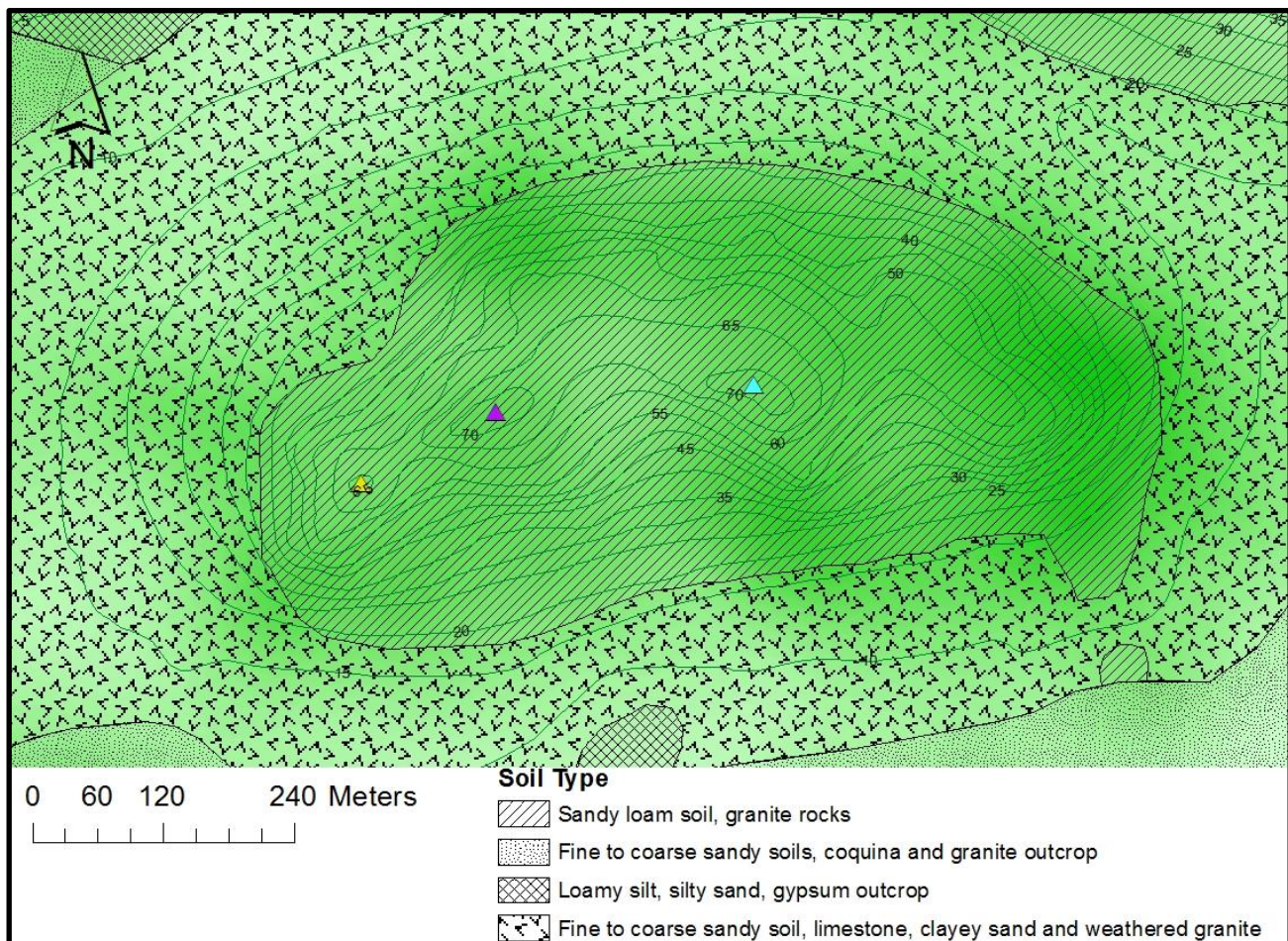


Source: Adapted from South Africa (1997)
Greyling (2001)

Figure 4.16 Soil types as an overlay on the radioelement map of ^{40}K .

The reason for the lower concentrations of ^{40}K in the ‘fine to coarse sandy soils, coquina and granite outcrop’ soil layer is its physical structure and composition. Coquina is an indication of the presence of broken shell and limestone. Even though granite outcrop is part of the soil layer name, there are no granite outcrops within this soil layer of the research site. This soil layer is also the furthest away from its parent material - the granite outcrops on Baviaansberg. This means that the further the soil particles are

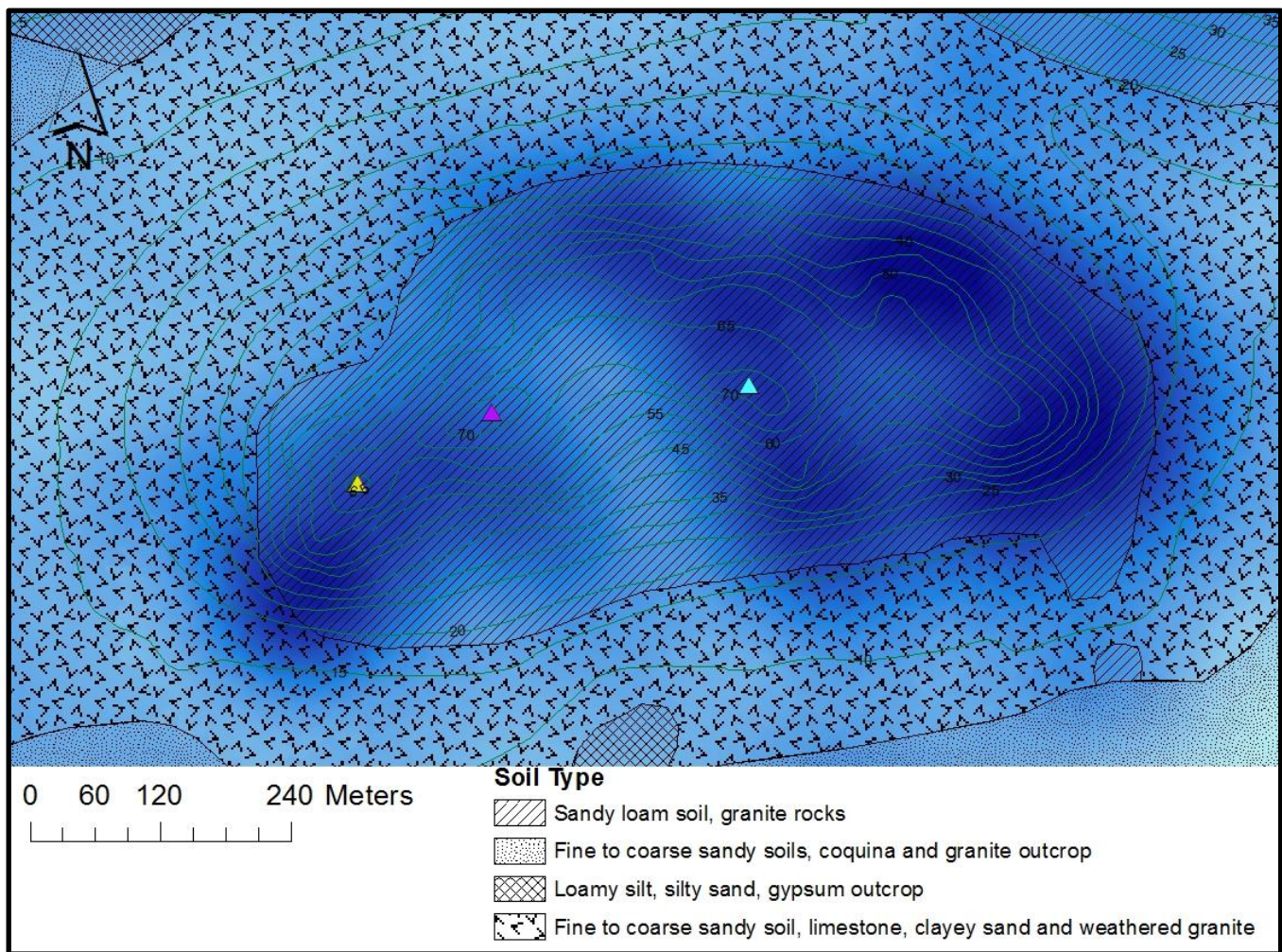
transported away from the parent material, the more they disperse and the more local external materials are attributed. During field measurements the presence of marine deposits in this soil layer was noted as confirmation of the addition of external material. The addition of such external materials further decreases the ^{40}K , ^{232}Th and ^{238}U concentrations. Soil in this area also contains more biological components in its composition as was recorded during field measurements. An addition of biological matter to soil will further decrease the concentrations of ^{40}K , ^{232}Th and ^{238}U . Soil with a higher quantity biological matter present is also generally associated with lower concentrations of ^{40}K (Ahmad 1997). The coarse sandy structure of this soil layer also attributes to the lower concentrations of ^{40}K , ^{232}Th and ^{238}U . The particles containing ^{40}K , ^{232}Th and ^{238}U radionuclides that reach these sandy areas by way of solution in overland flow will not be deposited, but will filter away through soil due to high infiltration rates associated with coarse sandy soils. There is also a relationship between high concentrations of ^{232}Th and ^{238}U that are associated with the ‘sandy loam soil, granite rocks’ soil layer (see Figures 4.17 and 4.18).



Source: Adapted from South Africa (1997)

Greyling (2001)

Figure 4.17 Soil Type as an overlay on the radioelement map of ^{232}Th .



Source: Adapted from South Africa (1997)

Greyling (2001)

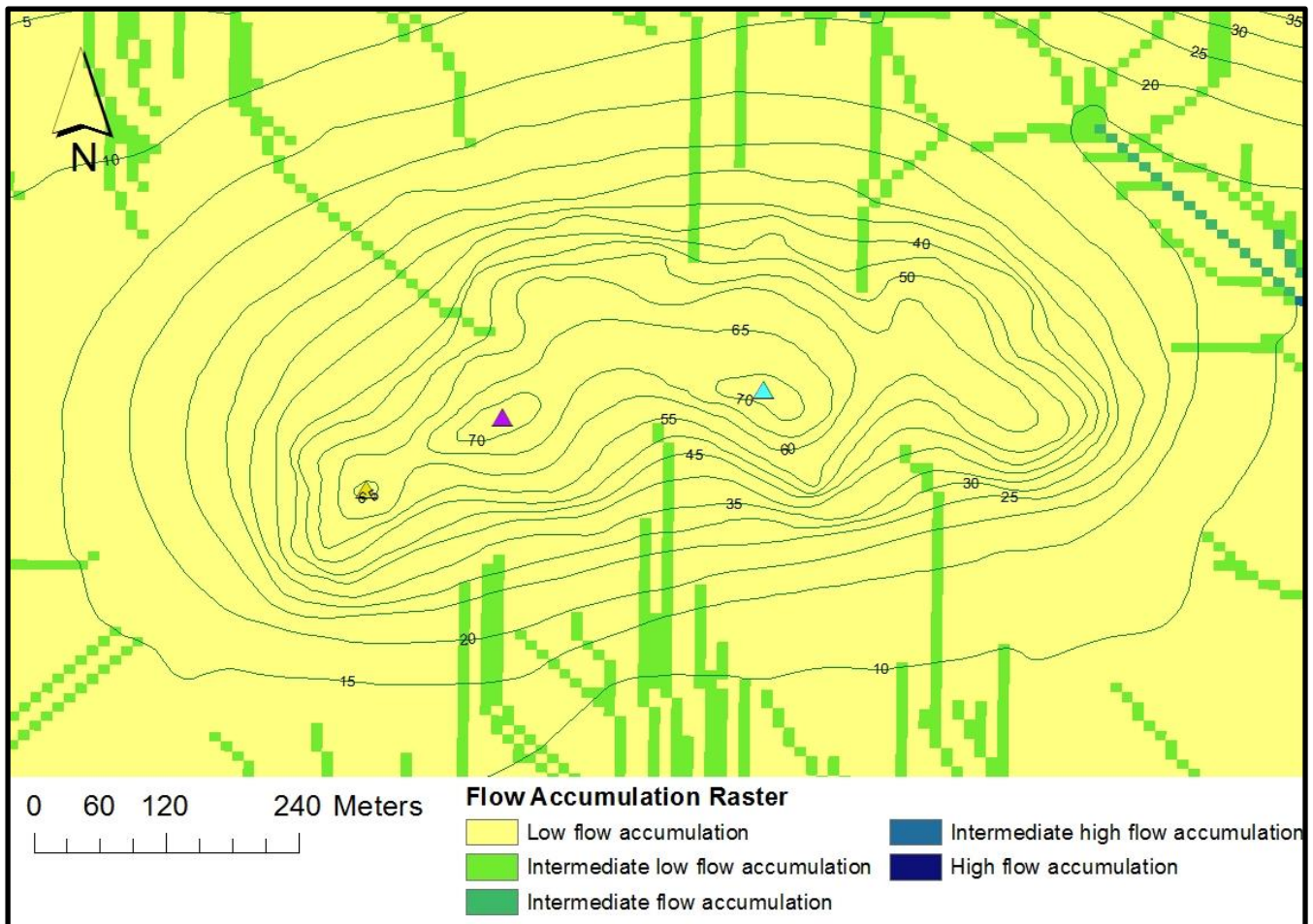
Figure 4.18 Soil Type as an over lay on the radioelement map of ^{238}U .

This relationship between the high concentrations of ^{232}Th and ^{238}U and ‘sandy loam soil, granite rocks’ soil layer is due to high levels of ^{232}Th and ^{238}U associated with granite outcrops and soil formed from these outcrops. Figures 4.16 to 4.18 support the work of Ramli (1997).

4.2.4 Hydrological impact

Water is the factor that has the largest influence on the physical landscape development on Earth (Strahler & Strahler 1992). Soil and weathered particle distribution are mostly dependent on the water flow over an area (Marshak 2001). Figure 4.19 is a flow accumulation raster of the research site. The flow accumulation is an indication of the amount of cells in the raster image that will flow into it. In this case the values of each cell is associated with the height above mean sea level according to the DEM. The

flow accumulation raster calculates the number of upstream cells that will account for the drainage into each cell (Chang 2012).



Adapted from South Africa (1997)

Figure 4.19 The flow accumulation raster as an overlay on the contour map of Baviaansberg. The flow accumulation raster was generated from a DEM created by digitizing the contours from an orthophoto series map of the research site.

In Figure 4.19 yellow pixels in the flow accumulation raster indicate an accumulated flow of 0.00 – 40.00 cells, light green pixels indicate an accumulated flow of 40.01 – 500.00 cells, darker green pixels, an accumulated flow of 500.01 – 1 000.00 cells, lighter blue pixels, an accumulated flow of 1 000.01 – 2 000.00 cells, and darker blue pixels an accumulated flow of 2 000.01 to 4 328 cells. Figure 4.19 indicates that the highest accumulated flow in terms of this research site is 2 000.01 to 4 328 cells, which is defined as high flow accumulation. Intermediate high flow accumulation is 1 000.01 to 2 000.00 cells, intermediate flow accumulation 500.01 to 1000.00, intermediate low flow accumulation 40.01 to 500.00 cells and low flow accumulation 0.00 – 40.00 cells. The grouping of the accumulation flow was tested

until the flow accumulation raster indicated adequate detail for analysis. The high to low flow accumulation rates were defined in terms of this research site, and do not relate to any other flow accumulation rates. The flow accumulation raster has a spatial resolution of 8.5 meters.

The flow accumulation raster can be considered as an indication of where deposition is more likely to occur during overland flow, because overland flow is the main method of water flow within the research site, as discussed in Section 3.1. There are no pertinent streams and rivers in the research site as the surface water flow over the research site is classified as overland flow. Overland flow becomes stagnant quicker than streamflow. It is worth noting that the majority of the intermediate to high flow accumulation areas lie below the 20 meter contour. These lower lying areas also correlate with the areas of gentle slope. This is an indication that these lower lying areas are the areas where the overland flow accumulate and where flow is likely to stagnate. These are the areas most likely for deposition to occur. The flow accumulation raster can thus be viewed as a proxy deposition raster. The areas that indicate intermediate low to high flow accumulation are also the areas in which deposition is most likely to occur.

Upon comparison of Figures 4.9 (a) and (b), the hydrological impact on the distribution of ^{40}K concentrations becomes noticeable. The spread of concentrations of ^{40}K on Baviaansberg shows an inversely proportional relationship to the degree of slope. The areas with a steep slope coincide with concentrations of ^{40}K of 1211 – 1351 Bq/kg, whereas the concentrations of ^{40}K of 1400 – 1501 Bq/kg coincide with areas of an intermediate and gentle slope. This is because ^{40}K is highly soluble. Any overland flow will remove the ^{40}K radionuclides, in solution, from the location over which the flow occurs. Soil particles will also be removed via suspension during overland flow. The overland flow from the higher lying surrounding areas will culminate in larger flow volumes that will slow down quickly and cause deposition of the particles in suspension (Hess 2014). This is supported by comparing the ^{40}K concentrations with the slope raster as done in Figure 4.20 (a) and (b). The comparison in Figure 4.20 (a) and (b) points to areas of intermediate low to high flow accumulation coinciding with the areas of higher concentrations of ^{40}K . The high flow accumulation coinciding with the areas of higher concentrations is especially prominent in the area between Baviaansberg and the neighbouring Malgaskop. The area between Baviaansberg and Malgaskop indicates the highest ^{40}K concentrations of 1400 – 1501 Bq/kg. This is caused by accumulation of particles in suspension from Baviaansberg and neighbouring Malgaskop.

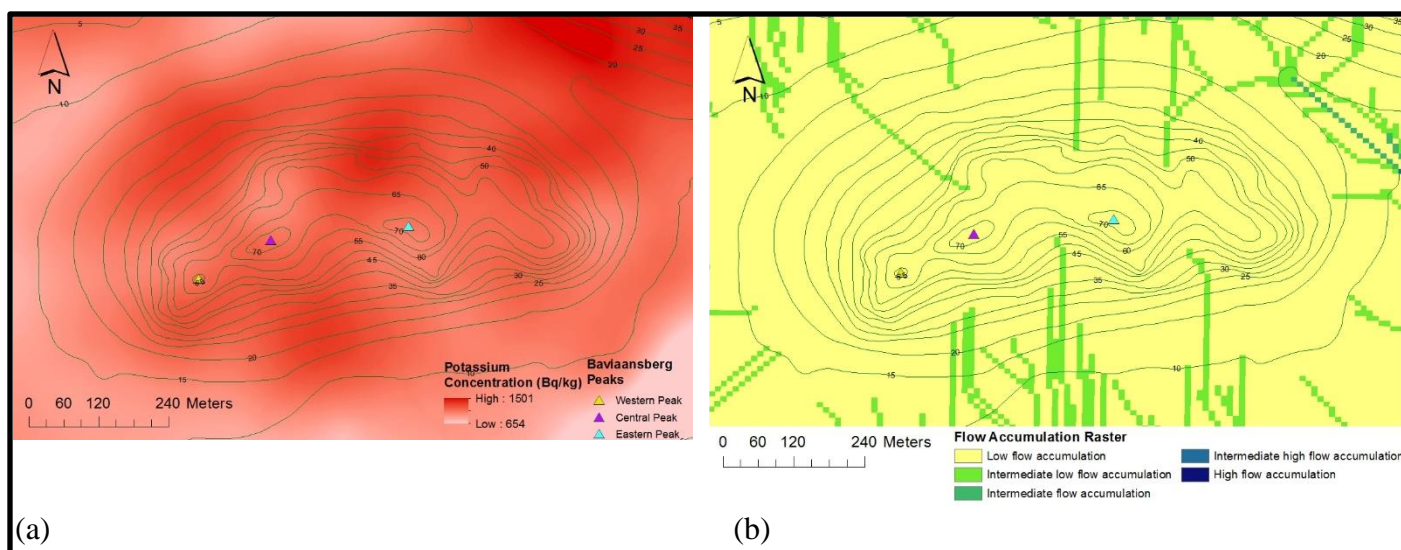


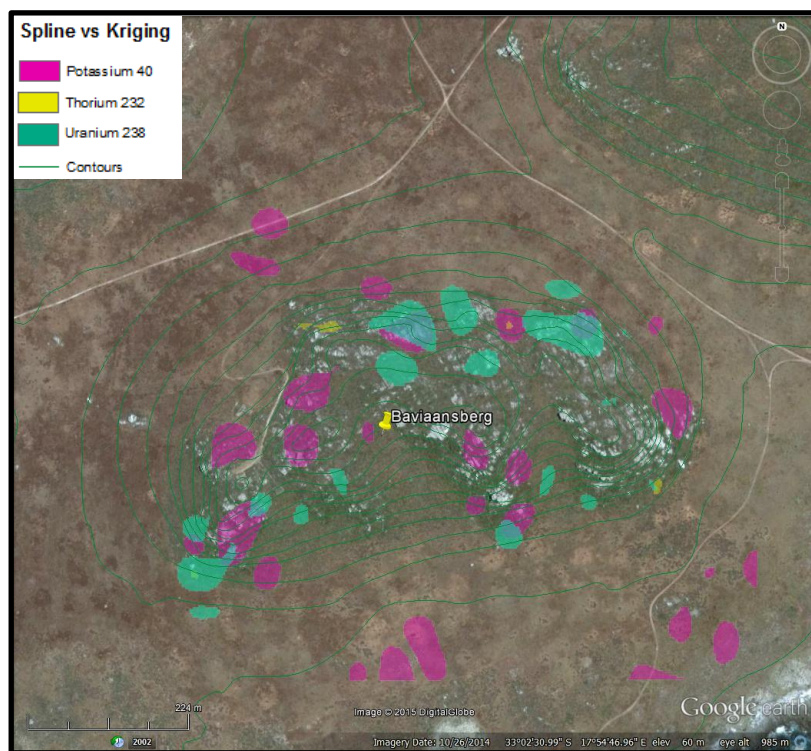
Figure 4.20 (a) – (b) A comparison between the (a) ^{40}K concentrations and (b) flow accumulation raster.

The accumulation of particles in suspension increases the number of weathered particles containing ^{40}K radionuclides that in turn increase the ^{40}K concentrations. The area between Baviaansberg and Malgaskop is also associated with a gentle slope, high flow accumulation, and soil type described as ‘fine to coarse sandy soil, limestone, clayey sand and weathered granite’. The combination of gentle slope, high flow accumulation close to the foot of Baviaansberg and Malgaskop as well as the ‘clayey sand’ contributes to higher ^{40}K radionuclide concentrations. These factors indicate that the surrounding water will settle in this area and evaporate, thus depositing the particles in solution containing ^{40}K radionuclides. However, there are areas of high flow accumulation that coincide with areas of low ^{40}K concentrations. These areas also coincide with areas of gentle slope. These are areas removed from the granite outcrops where the water comes to rest after overland flow. The majority of particles in suspension would have been deposited before reaching these areas, leaving only very small particles in suspension and particles in solution present in the water. Any ^{40}K radionuclides that are in solution will be lost due to the high infiltration rates of the sandy soils of the area, hence contributing to a decrease in ^{40}K concentrations.

The hydrological impact on ^{232}Th and ^{238}U are visible in Figures 4.8 (b) and (c). The impact on the distribution of the concentrations of ^{232}Th and ^{238}U is not as great as that of ^{40}K due to the fact that ^{40}K is much more soluble than ^{232}Th and ^{238}U . This can be observed whereby the higher concentrations of ^{232}Th and ^{238}U are focused around the granite outcrops, and it shows a gradual decrease in ^{232}Th and ^{238}U concentrations downslope. This is due to the overland flow in the research site that gradually removes

the ^{232}Th and ^{238}U radionuclides from the parent material. Figures 4.8 (b) and (c) also show that ^{232}Th and ^{238}U are less soluble than ^{40}K . Figure 4.13 shows that higher ratios of ^{232}Th to ^{40}K are concentrated around the areas of steep slope (granite outcrops), and the ratio decreases downslope away from Baviaansberg. The same scenario is reflected in Figure 4.15 where higher ratios of ^{238}U to ^{40}K are concentrated around the granite outcrops and decrease downslope. This is due to the overland flow of water that accumulates sediment with ^{40}K radionuclides in suspension and in solution and deposits it further downslope from the granite outcrops. The hydrological impact on the spread of concentrations of natural radionuclides is influenced by their solubility, as was demonstrated by Ruffel et al. (2006) and Al-Hilal & Al-Ali (2016). This effect is highlighted in Figure 4.20, and supports the fact that ^{40}K is the least soluble of the three radionuclides.

Figure 4.21 is a raster image that indicates areas of spatial irregularities. This means that the areas indicated in Figure 4.21 represent areas where the Kriging interpolated values differs significantly from the measured values.

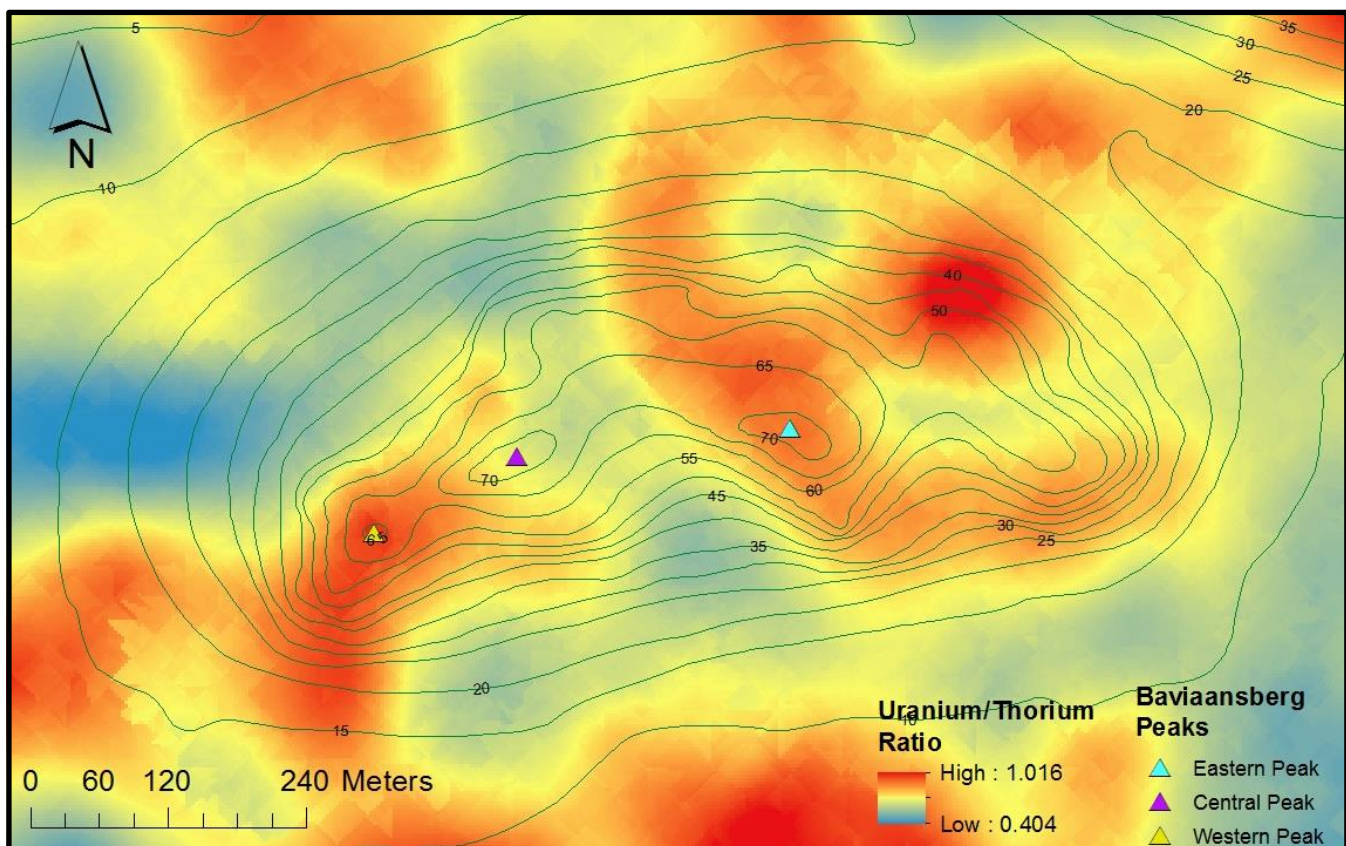


Source: Adapted from South Africa (1997)
Google Earth (2016)

Figure 4.21 A Google Earth image of the research site indicating the areas with differences in values between Kriging and thin plate splines. When the spline and Kriging results are compared, it is clear that ^{232}Th measurements show the least discrepancies.

From Figure 4.21 it is clear that the ^{232}Th results show the least discrepancies between the interpolated values and the measured values. This means that the interpolated values from Kriging fall within one standard deviation from the measured values, thus the predicted values are similar to the actual measured values. The reason for this is that ^{232}Th is the least soluble of the three natural radionuclides and will not be removed from its geographic position as easily as ^{40}K and ^{238}U . This supports the findings by Ruffel et al. (2006) and Al-Hilal & Al-Ali (2016).

There is also an occurrence where the ratio of the concentrations of ^{238}U to ^{232}Th in the areas of deposition are the same as that of the granite outcrops, as seen in Figure 4.22. The deposition that occur in these areas are from particles containing ^{238}U and ^{232}Th natural radionuclides in suspension (Michel 1984), because particles in solution will be lost due to drainage. Particles in suspension originate from granites with a ratio of one to one ^{238}U to ^{232}Th , thus the areas where these particles are deposited will show the same ratio of one to one ^{238}U to ^{232}Th .



Adapted from South Africa (1997)

Figure 4.22 An illustration of the ratio of distribution of ^{238}U to ^{232}Th as an overlay on the contour map of Baviaansberg.

Figure 4.23 is a comparison of the (a) flow accumulation raster, (b) the granite outcrops and (c) the ratio of ^{238}U to ^{232}Th . In Figure 4.23 (a) – (c) it can be seen that the areas of a ratio of one to one of ^{238}U to ^{232}Th correlate with the granite outcrops and with the areas of high deposition. In Figure 4.23 (c) the valley on the southern slope between the eastern and central peak shows a ratio of ^{238}U to ^{232}Th of 0.54 to 0.66. This result supports the work of Ruffel et al. (2006) and Al-Hilal & Al-Ali (2016). It indicates that the ^{238}U radionuclides are removed first and are leaving the less soluble ^{232}Th radionuclides behind.

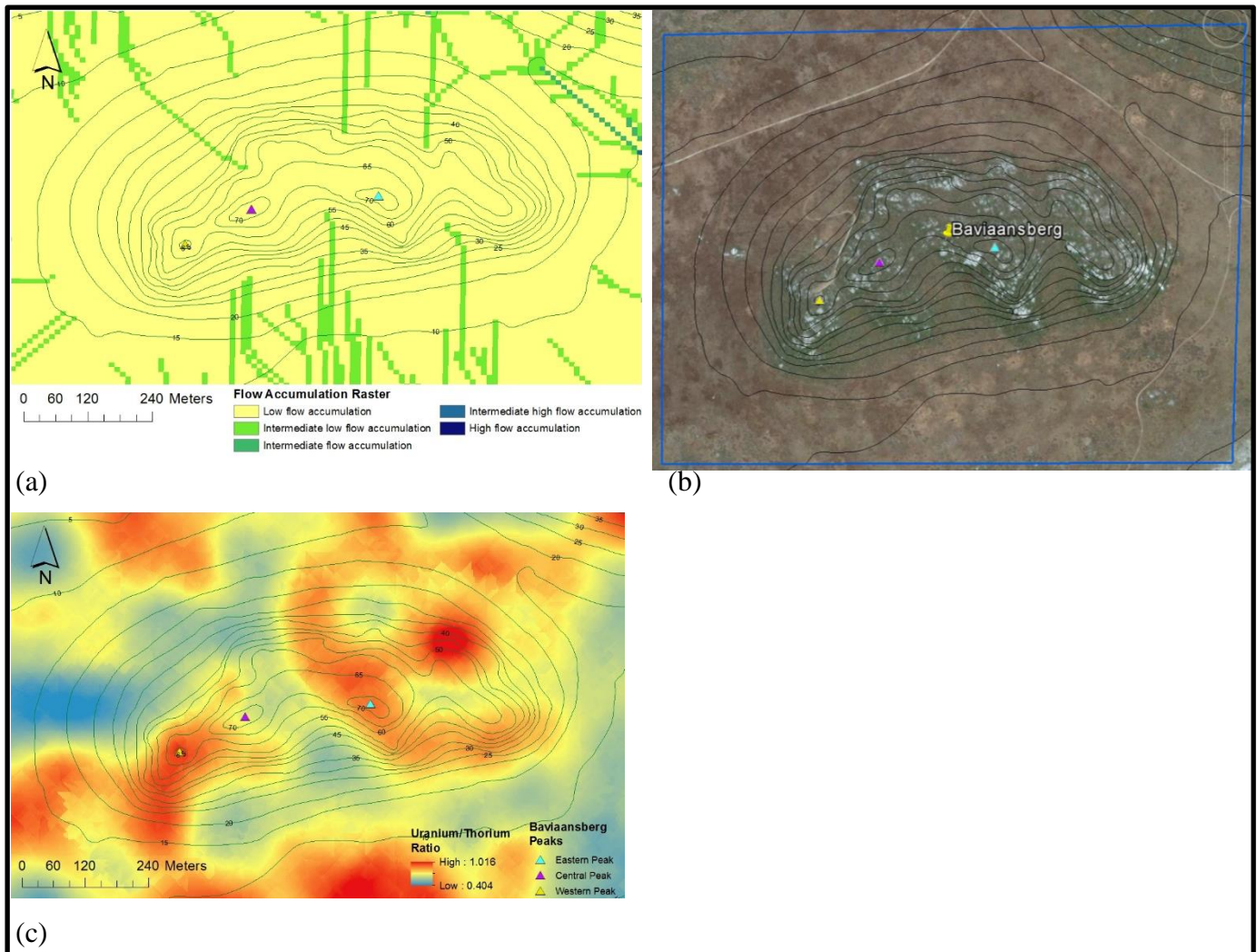


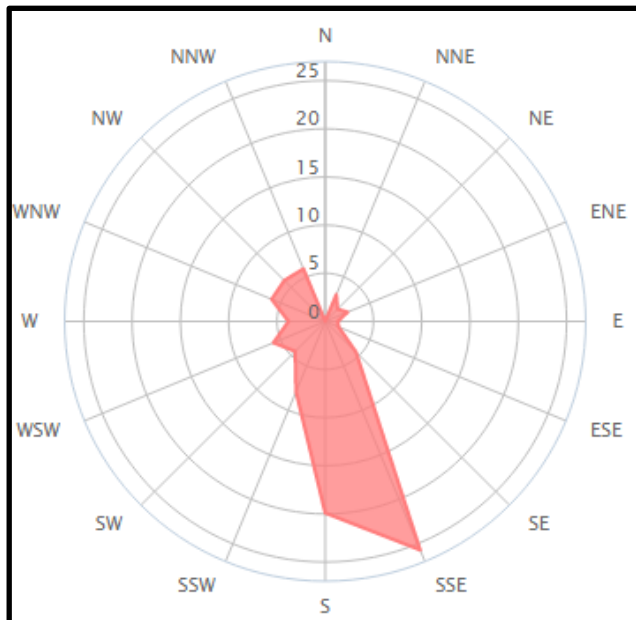
Figure 4.23 A comparison of the (a) flow accumulation raster, (b) the granite outcrops and (c) the ratio of ^{238}U to ^{232}Th .

4.2.5 Aeolian impact

Over time the impact of aeolian erosion becomes more prevalent in soil formation (Hess 2014). The impact of the aeolian erosion can be seen in Figure 4.13 (a) to (e) which shows the southern slope as

steeper than the northern slope. What might have occurred over time is that the dry southerly winds deposited fine particles on the leeward side of Baviaansberg to produce the less steeper northern slope (Goossens 2006). From Figure 4.24 it can be seen that the wind direction is south-east to south-west 62.4% of the time and prevail in the warm and dry months of the year. A mere 27.5% of the year the wind direction is west south-west to northerly.

The significance of the west south-westerly and northerly wind directions is the fact that these winds are associated with winter and the rainy season, as was discussed in Section 3.1. The aeolian influence of these winds will thus be less prominent because of the fairly frequent wet conditions. Goossens (2006) showed that maximum deposition of small particles occurs on the leeward side. Goossens (2006) also determined that the windward side of a hill has a steeper profile than the leeward side, due to the deposition that occurs on the leeward slopes of a hill. Figure 4.13 (a) to (e) supports the findings of Goossens (2006).



Source: www.windfinder.com

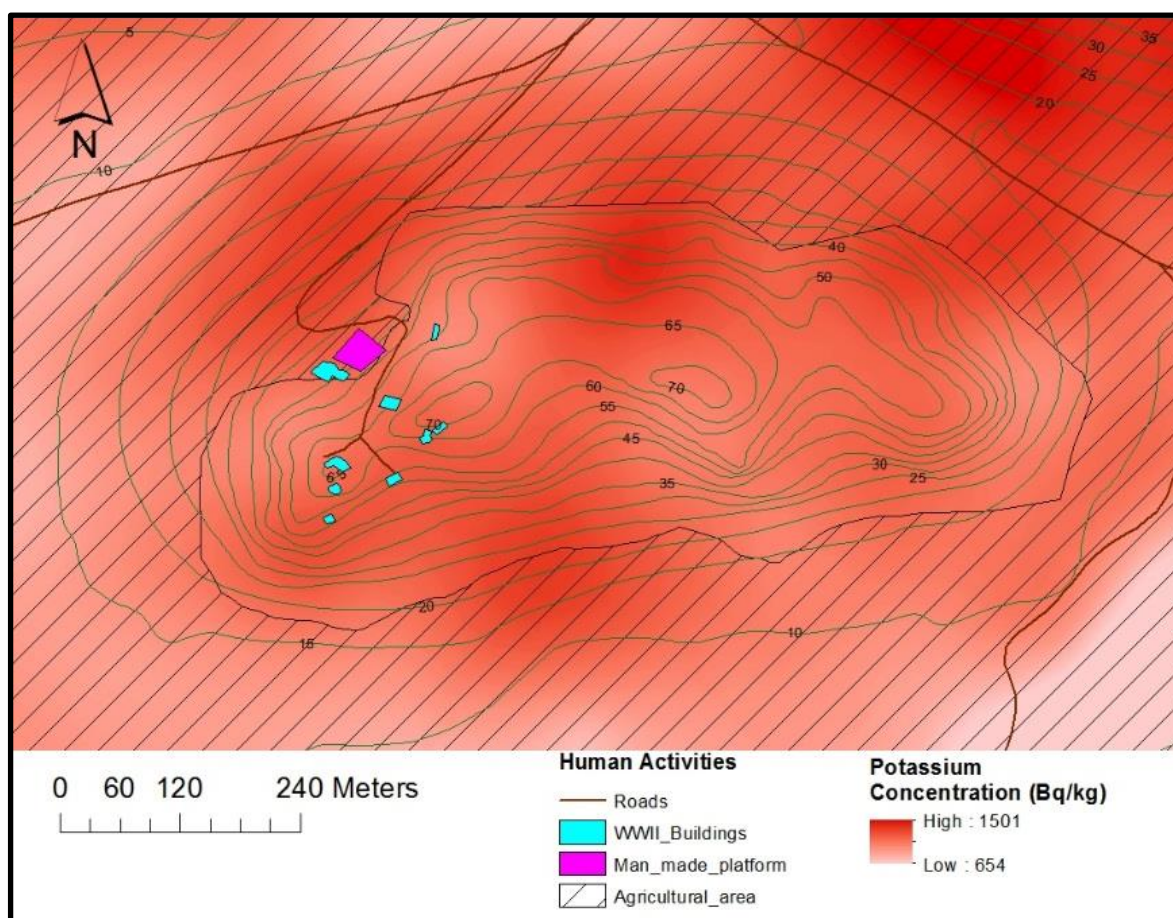
Figure 4.24 Wind direction distribution of the Saldanha area. Data for the observations were taken from December 2003 to February 2008 daily from 07:00 to 19:00 local time and are represented in percentages per annum.

The impact of aeolian erosion and deposition on the ^{40}K concentrations can be seen in Figure 4.2. The concentrations of ^{40}K is higher on the northern slope of Baviaansberg than on the southern slope. The summer winds cause aeolian erosion of the southern slope, the windward slope, and deposits the aeolian eroded particles on the northern slope, the leeward slope. These deposited particles containing ^{40}K

radionuclides increase the amount of ^{40}K radionuclides already in the soil; they in turn increase the ^{40}K concentrations. The distribution of the concentrations of ^{40}K supports the research done by Goossens (2006). By studying the concentration distribution of ^{40}K it is possible to predict the influence of aeolian erosion around hills. ^{232}Th and ^{238}U showed no noticeable correlation in terms of its concentration levels and aeolian impact.

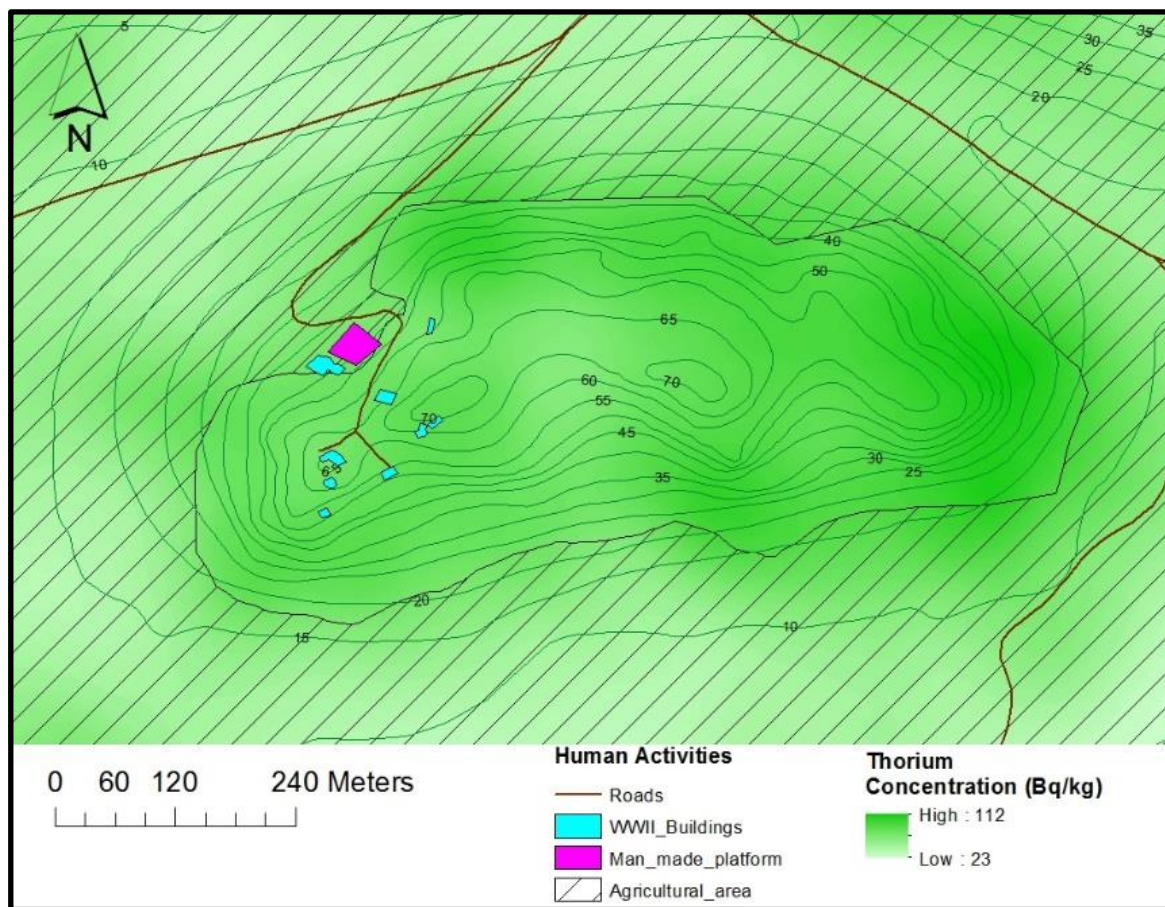
4.2.6 Human impact

Bezuidenhout (2012) has shown that historical human activities decrease the radiation concentrations of ^{40}K . His findings, on the influence of human activities on ^{232}Th and ^{238}U , were inconclusive. Figures 4.25 to 4.27 display the human activities overlay on the radioelement maps of ^{40}K , ^{232}Th and ^{238}U .



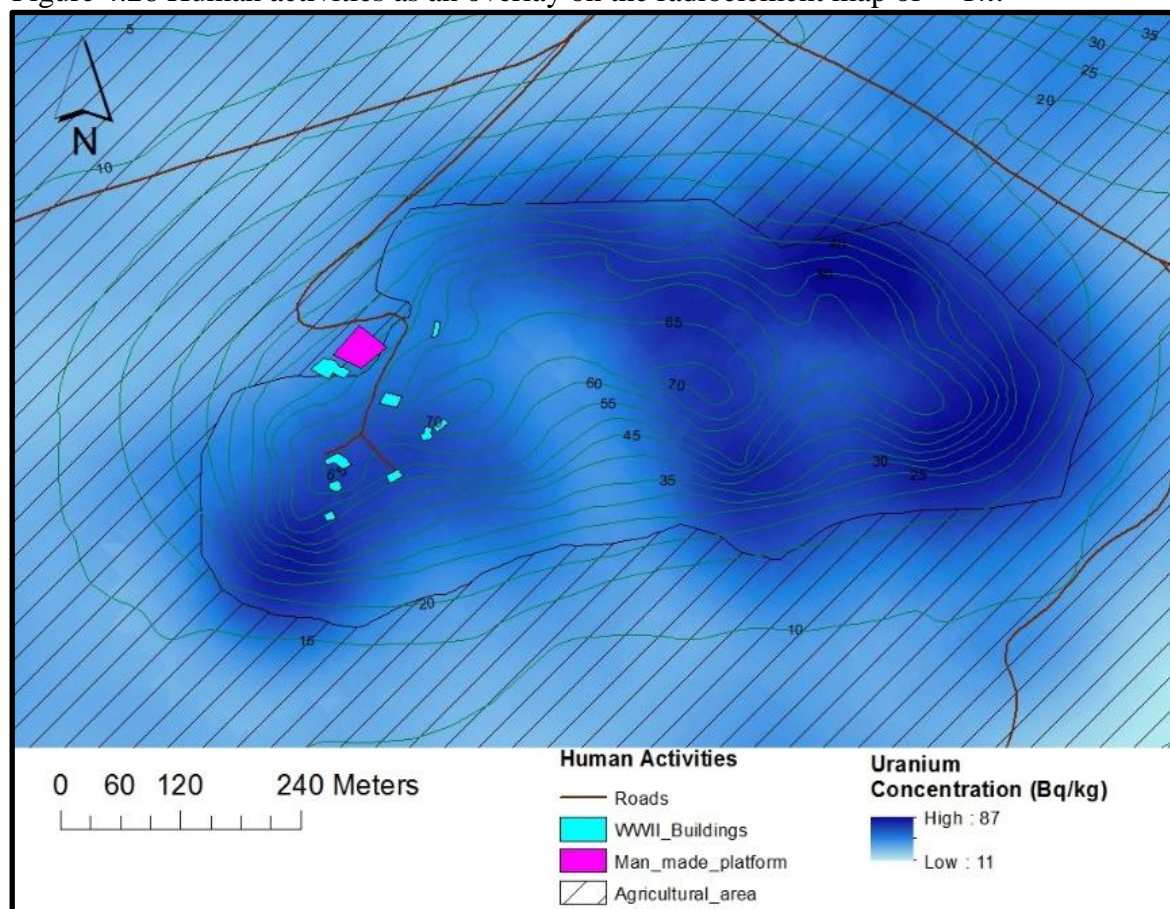
Adapted from South Africa (1997)

Figure 4.25 Human activities as an overlay on the radioelement map of ^{40}K .



Adapted from South Africa (1997)

Figure 4.26 Human activities as an overlay on the radioelement map of ^{232}Th .

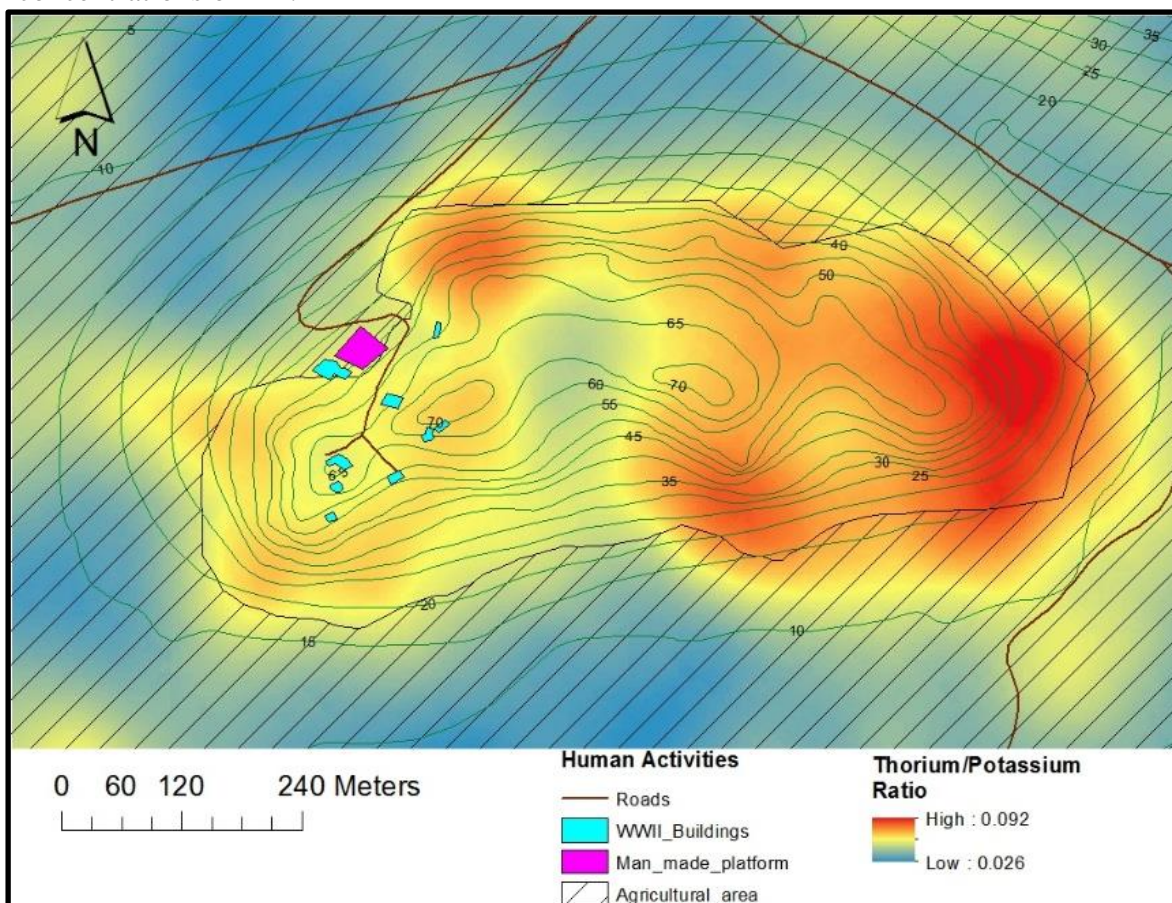


Adapted from South Africa (1997)

Figure 4.27 Human activities as an overlay on the radioelement map of ^{238}U .

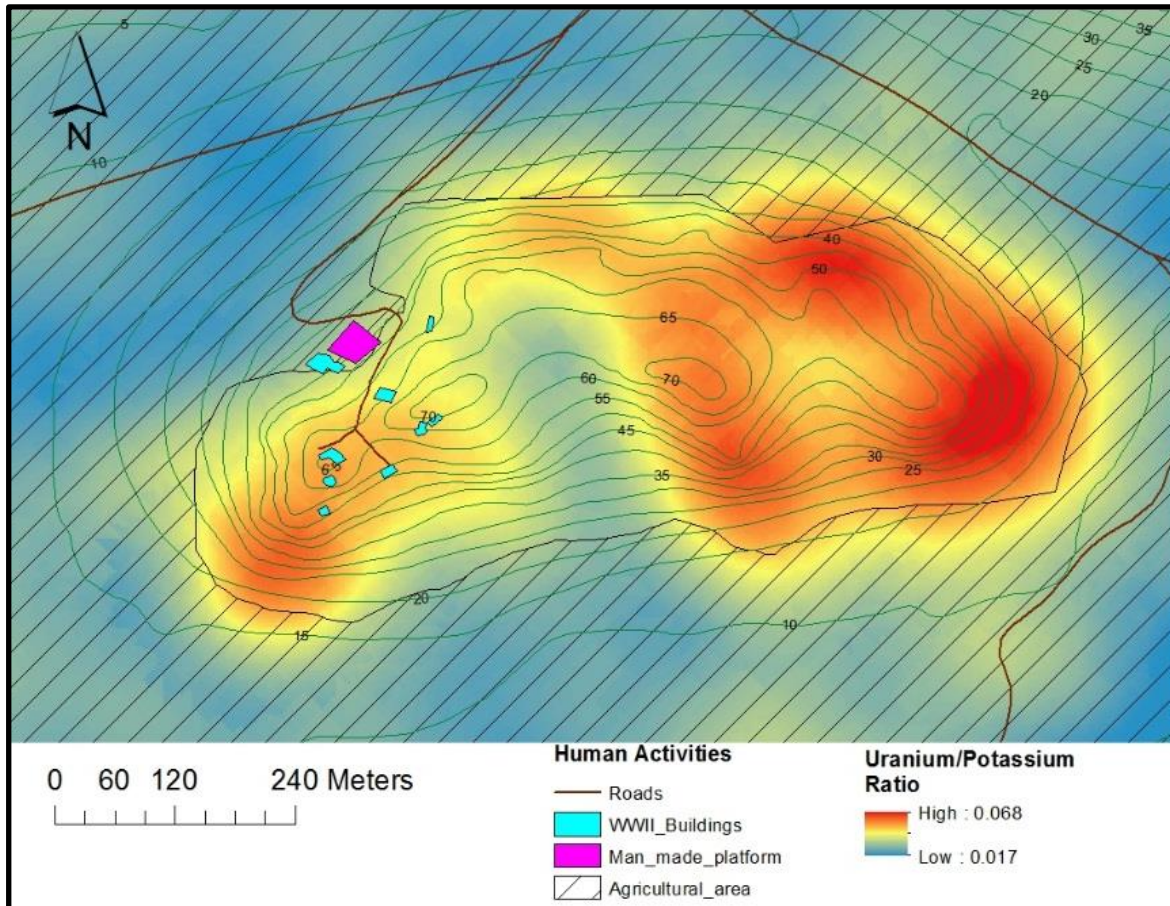
In Figure 4.25 the areas around the WWII buildings and man-made platform shows lower ^{40}K concentrations than their surrounding areas. This might be due to the human activities in and around these areas. However, there is not conclusive evidence of this proposition. More measurements of this specific areas need to be taken to confirm or negate a possible relationship between human activities and potassium levels. Figures 4.26 and 4.27 also show no conclusive evidence of a positive relation between the WWII buildings and man-made platform, and the concentrations of ^{232}Th and ^{238}U . These results corroborate the findings of Bezuidenhout (2012) but should be studied further in order to firmly establish further relationships or the absence thereof.

There is, however, an established relationship between human agricultural activities and the concentrations of ^{232}Th and ^{238}U , according to Figures 4.24 and 4.26. The concentrations of ^{232}Th and ^{238}U decrease downslope from the boundaries of the agricultural areas. This is not conclusive, as the areas above the agricultural boundaries are also the areas that were not conducive to agriculture, *i.e.*, rocky areas with granite outcrops. These rocky outcrops also influence the concentrations of ^{232}Th and ^{238}U . However, Figures 4.28 and 4.29 support the theory that human activities influence the concentrations of ^{40}K .



Adapted from South Africa (1997)

Figure 4.28 Human activities as an overlay on the map that indicates the ratio of $^{232}\text{Th}/^{40}\text{K}$.



Adapted from South Africa (1997)

Figure 4.29 Human activities as an overlay on the map that indicates the ratio of $^{238}\text{U}/^{40}\text{K}$.

The areas on and surrounding the WWII buildings and man-made platform show a lower ratio, 0.050 – 0.057, of ^{232}Th to ^{40}K in comparison to the areas on the same contours with the same slope profile, 0.070 – 0.092. There is also a similar relationship between the WWII buildings and man-made platform to the ratio of ^{40}K to ^{238}U , as seen in Figure 4.29. However, this relationship is not as prominent as the relationship between human activities and the ratio of ^{232}Th to ^{40}K as shown in Figure 4.28. Blue tinted areas in Figures 4.28 and 4.29 are areas where the ratio of ^{232}Th and ^{238}U to ^{40}K are lowest, thus indicating lower concentrations of ^{40}K in comparison to ^{232}Th and ^{238}U . This is another indication that the ^{40}K radionuclides are removed easier than the less soluble ^{232}Th and ^{238}U radionuclides, which supports the work of Ruffel et al. (2006) and Al-Hilal & Al-Ali (2016)

4.3 NATURAL RADIATION AND GEOGRAPHIC FACTORS

The natural radionuclides ^{40}K , ^{232}Th and ^{238}U are ever present in the natural environment. However, the concentrations differ measurably between different rock and soil types. Granites have high

concentrations of natural radiation. This applies to soil originating from these granites as well, as was discussed in Chapter 1. The distribution of soil and therefore natural radiation is highly dependent on the geographic factors of an area. Chapter 4 has shown that the geology of an area influences the distribution of ^{40}K , ^{232}Th and ^{238}U concentrations where high concentration levels were measured close to and on top of granite outcrops on Baviaansberg in Saldanha Bay. The slope of a hill influences the distribution of ^{40}K to a greater extent than ^{232}Th and ^{238}U because ^{40}K is more soluble than ^{232}Th and ^{238}U . The steeper, southern, slope of Baviaansberg has shown lower concentration levels than the less steep northern slope.

Soil composition contributes to the distribution of the concentrations of natural radiation where soil closer to granite outcrops have higher concentrations of ^{40}K , ^{232}Th and ^{238}U . Finer grained sandy soils further from granite outcrops also show a drop in concentrations of ^{40}K , ^{232}Th and ^{238}U due to its high infiltration rates. The further soil is transported away from its parent material, the more dispersed the soil becomes. More external materials, such as dead organic materials or marine deposits, are also added to its composition as the distance away from the parent material increases. This changes the composition of the soil as well as the natural radiation signature of the soil. The hydrology of an area influences the distribution of ^{40}K to a greater extent than that of ^{232}Th and ^{238}U due to ^{40}K being more soluble than ^{232}Th and ^{238}U . Wind also plays a role in the general distribution patterns of natural radionuclides. It is particularly visible in the distribution of ^{40}K concentrations where the leeward side of Baviaansberg hosts a greater number of areas of high ^{40}K concentrations than its windward side. The results of this study revealed that human activities also play a role in determining the distribution of natural radiation, again to a greater extent in the distribution of ^{40}K . However, these relationships could not be established beyond doubt and will have to be studied further. All relevant geographic factors have a collective impact on the spread of natural radiation within an area. In Chapter 5 a summary and a conclusion of the results of this study are presented.

CHAPTER 5: CONCLUSION AND RECOMMENDATION

The results of the research indicated that the concentration of the natural radionuclides are influenced by local geographic factors within an area. Geology, topography, soil type, hydrology, wind and humans were the factors that displayed a possible influence on the spread of ^{40}K , ^{232}Th , and ^{238}U concentrations within the research site. This concluding chapter provides an overview of the research by revisiting the aim and objectives, summarising and discussing the conclusions, discussing the implications, applications and limitations of the research, and providing possible improvements on the research. Chapter 5 concludes with unanswered questions and new directions for further research.

5.1 BACKGROUND, AIM AND OBJECTIVES OF THE STUDY

Soil is a dynamic feature of Earth's terrain that is constantly changing over time. Geographic factors such as geology, topography, soil type, hydrology, wind and humans are responsible for the ever evolving landscapes of Earth. These factors also influence the distribution of soil from its origin at the parent material. Parent material of soils is an important factor in determining the type of soil. Natural radionuclides are part of the composition of parent materials. Natural radionuclides ^{40}K , ^{232}Th , and ^{238}U are present in various concentration levels in the parent materials. Soil that stems directly from these parent materials then should logically bear the same natural radionuclide concentration levels. These natural radionuclides emit γ - ray photons, and are responsible for the natural radiation of an area. By plotting the spread in concentrations of natural radionuclides it is possible to determine the effect of various geographic factors on the distribution of natural radionuclide concentrations.

Baviaansberg within the Saldanha Bay Military Area on the West Coast of South Africa was identified as the research site. This area is very unique as it is situated such that aeolian and alluvial depositions occur mainly from within the area. This provided the perfect opportunity to study the effects of the above-mentioned geographic factors on the distribution of natural radionuclide concentrations. Due to the lack of aeolian and alluvial deposition from outside sources the soils within the research site are all formed from the weathering and erosion of the granite outcrops within the area.

The aim of the research was to measure the variation in the concentrations of the natural radionuclides of Baviaansberg, to create radioelement maps from the measured data, and to use these maps to determine

the influence of geographic factors on the distribution of radionuclides. This aim was achieved by completing the research objectives revisited below.

First, a thorough literature review of similar studies was conducted as per Objective 1. Various methodologies and equipment were researched and experimented with. It was decided, as per Objective 2, that the best measurement technique for the research would be *in situ* measurements by means of a Sodium Iodide Thallium Infused (NaI(Tl)) scintillation detector with a 7.62 x 7.62 cm crystal coupled to a scintiSPEC Multi-Channel Analyser. This setup was then connected via a USB connection to a Trimble Yuma Rugged Tablet PC with WinTMCA32 software.

Before the *in situ* measurements of the research site could commence Objective 3 needed to be finalised by means of demarcating the study area. This was done by means of creating a fishnet grid on a 1:50 000 topographic map of the research site using ArcMap. The grid consisted of three hundred and thirty-six blocks of 48.6 meters by 47.6 meters. The GPS positions of the centre of these blocks were demarcated as the measurement positions. These positions were tabled and used to structure the field work.

An initial efficiency calibration was done on the detector system at NECSA and the system was energy calibrated prior to each set of *in situ* measurements. As per Objective 4 a total of 336 *in situ* γ - ray measurements were taken in predetermined locations within the research site. Every energy peak was then recalibrated after each measurement in order to negate the drift error induced by the ambient temperature fluctuations.

After post measurement calibrations were completed, the measurement data were analysed in order to extract the concentrations of each of the ^{40}K , ^{232}Th , and ^{238}U radionuclides in order to conclude Objective 5. The concentrations of the natural radionuclides were then used during qualitative analysis in order to generate radioelement maps as required by Objective 6. These radioelement maps were utilized in conjunction with various other maps, such as a slope and flow accumulation rasters, to determine the influence of geographic factors on the distribution of natural radionuclide concentrations in order to finalise Objective 7.

5.2 GEOGRAPHIC FACTORS AND THEIR INFLUENCE ON NATURAL RADIONUCLIDE CONCENTRATIONS

The analysis of the results showed that the geographic factors of an area influence the distribution of concentrations of the natural radionuclides, ^{40}K , ^{232}Th and ^{238}U , the main premise of the research. It was found that the **geology** of the area influences the distribution of the concentration of natural radionuclides within that area. Granite outcrops and soil directly beside these outcrops displayed the highest concentrations of natural radionuclides. These natural radionuclide concentrations generally decreased downslope from the granite outcrops, with the exception of ^{40}K radionuclides where the concentrations increased in areas where deposition from accumulated flow over the area occurred.

The **topography** of the research site was discussed under the influence of slope. Factors such as drainage patterns and aspect were incorporated under hydrological and aeolian impacts on the research site. Slope was found to bear a greater influence on the spread of ^{40}K concentrations than on ^{232}Th and ^{238}U concentrations, mainly due to ^{40}K being more soluble than ^{232}Th and ^{238}U . Steeper slopes cause less deposition to occur as the overland flow of water does not have time to settle, which again causes a greater decrease in ^{40}K concentrations as the distance from parent materials increased. Once slope becomes less steep and the water flow is sufficiently slow, smaller particles as well as those in suspension are deposited. Less steep slopes cause a more gradual decrease in ^{40}K concentrations. The spread of ^{40}K concentrations on Baviaansberg in the research site shows an inversely proportional relationship to the degree of slope.

Soil type has shown that it influences the concentration distribution of ^{40}K , ^{232}Th and ^{238}U . The various soil layers within the research site indicated different concentrations of natural radionuclides. This is explained where the physical structure and composition of soil changes the further it is moved from the parent material. External biotic elements, such as marine deposits and dead vegetation, are added to the soil the further it is moved from the parent material, which in turn decreases the concentration of natural radionuclides within that soil.

The **hydrology** of an area is another factor that influences the spread of ^{40}K , ^{232}Th and ^{238}U concentrations. The influence of the hydrology of the research site becomes apparent in the distribution of ^{40}K concentrations especially, as it is the most soluble of the natural radionuclides. ^{40}K radionuclide particles are removed via solution from their origin. Once water becomes stagnant these particles in

solution are removed due to the drainage of the soil type. Should the soil be such that no drainage occurs then these particles in solution would be deposited once the water has evaporated, leading to an increase in ^{40}K radionuclide concentrations.

The research results also indicated that there is an **aeolian impact** on the distribution of natural radionuclides. In the research site a generally higher concentration of natural radionuclides was recorded on the northern slope, the leeward side of Baviaansberg. This is an indication of the aeolian influence of the dry southerly winds where small particles are removed from the southern slope and deposited on the northern slope, thus leading to a general increase in natural radionuclide concentrations on the northern slope of Baviaansberg.

Human activities also impacts the distribution of natural radiation. The results indicated a relationship between agricultural (human) activities and the concentrations of ^{232}Th and ^{238}U . The concentrations of ^{232}Th and ^{238}U decrease downslope from the boundaries of the agricultural areas. Human activities also seem to influence the ^{40}K concentrations where the areas on and surrounding the WWII buildings and human-made platform on Baviaansberg showed lower ratios of ^{232}Th to ^{40}K in comparison to the areas on the same contours with the same slope profile. There also seems to be a similar relationship between the WWII buildings and man-made platform to the ratio of ^{40}K to ^{238}U . However, the results were inconclusive and more data need to be collected of these specific areas of human activities.

5.3 THEORETICAL AND PRACTICAL IMPLICATIONS AND APPLICATIONS OF THE RESEARCH

This research has shown that by analysing the concentration levels of natural radionuclides it is possible to establish the influence of geology, topography, soil type, hydrology, wind and human activity on a specific area. The opposite of the previous statement is also possible, by studying the various geographic factors geology, topography, soil type, hydrology, wind and human activity, it is possible to predict areas of high and low natural radionuclide concentrations. It will also be possible to predict areas of high and low natural radionuclide concentrations by analysing only the slope and flow accumulation rasters of an area.

The study showed that radioelement maps provide insight into the geology of an area. It allows for the identification of anomalies within an area that in turn can point to shallow geological features such as

underlying granite outcrops. By using the results from this study it is possible to identify various soil types by means of radioelement mapping. It will also be possible to describe soil movement within that area. Linking the natural radionuclide concentration signatures to soil types will enhance soil mapping techniques. The study has shown that it might be possible to identify areas of human activity using radioelement mapping. The study has confirmed by means of qualitative analysis that ^{232}Th is the least soluble and mobile of the natural radionuclides.

5.4 LIMITATIONS AND POSSIBLE IMPROVEMENTS OF THE RESEARCH

The biggest limitation in terms of this research was the allocated time for field measurements. In order for the measurements to portray the natural radionuclide concentrations accurately, the soil needed to be dry. Thus the measurements could only take place in the dry summer months. During the period of field measurements there were unseasonal summer showers which further interrupted the time available for measurements.

Access to the area also proved to be a research limitation as the research site was located within military grounds. Measurement time was lost due to military exercises that took place within the research site, effectively preventing access to Baviaansberg. The physical terrain of the research site also delayed measurement time. Although the areas below the 20 meter contour in the research site provided no challenges in terms of access, areas above the twenty meter contour proved challenging to access. The areas above the twenty meter contour became steep. These are also the areas where granite outcrops are located. Some predetermined measurement positions were located on these boulders. Measurements were taken on accessible boulders, however some measurement positions were moved due to the inaccessibility there of. The vegetation cover above the 20 meter contour also became denser. The dense vegetation together with the slope steepness and granite outcrops inhibited movement between measurement positions. This in turn caused a decrease in the number of measurements completed per day. Due to the time constraints only one area could be measured which did not allow for a comparison with another set of measurements.

The *in situ* measurement equipment functioned well in general, with the exception of the GPS. The GPS introduced a delay in updating the GPS position on certain days. This caused an overshoot in determining the measurement position, thus instead of moving directly to the pre-determined measurement position additional time was required to settle on the final pre-determined measurement position. This in turn

allowed for only four to six measurements instead of fifteen to twenty measurements to be completed per day.

The available topographical data on the research site is also limited. In order to increase the accuracy of the topographical data a drone mapping system can be used in conjunction with remote sensing software. This will provide topographical data with centimetre accuracy.

To improve on the accuracy of the radioelement maps, more measurements can be taken. Instead of producing a grid of 48.6 meter by 47.6 meter blocks, a 10 meter by 10 meter block grid can be generated and used. A grid with smaller block sizes will increase the accuracy of the radioelement maps significantly, permit more accurate interpolation, and highlight more anomalies within the research site. It will also provide easier identification of anomalies within the research site that can be linked to the influence of specific geographic factors. An alternative site with similar physical characteristics could also be used for measurements. Data collection in an alternative or control site would allow the comparison of results to strengthen findings.

Soil samples could be taken at measurement positions and be compared to *in situ* measurements. Such a comparison could result in a study on its own, or it might be used as a tool to check the accuracy of measurements. The difference in the sample concentrations and the *in situ* measurements can also be used to identify areas where an anomaly exists. This information can also be incorporated in the results to gain a better understanding of the influence geography of an area has on the distribution of natural radiation.

5.5 UNANSWERED QUESTIONS AND NEW DIRECTIONS FOR FURTHER RESEARCH

The research has confirmed that geographic factors influence the distribution of natural radionuclides within an area. However, the extent to which each of the geographic factors influence the spread of natural radionuclides was not determined.

Human activities also play a role in determining the distribution of natural radiation, and then to a greater extent in the distribution of ^{40}K . However, these relationships could not be proven beyond doubt and will have to be exposed to further scientific investigation.

Data collected from this research site was not compared to data from another area with similar physical geographic characteristics. Further research could entail identifying an area with similar physical geographic characteristics and comparing the results to the current research. Such comparison would afford the opportunity to confirm the influence of specific geographic factors on the distribution of natural radionuclides.

Pervious research on the influence of geographic factors on the distribution of natural radionuclides is limited. There is thus limiting data available with which any current results may be compared. Further research in this research site and direction will add to the relevant body of knowledge, increase the size of available data, invite further discussions and again offer new voids for further research within the broad field of the relationship between geographic factors and the distribution of natural radionuclides.

LIST OF REFERENCES

- Abbadly AGE 2010. Evaluation of heat generation by radioactive decay of sedimentary rocks in Eastern Desert and Nile Valley, Egypt. *Applied Radiation and Isotopes* 68: 2020-2024.
- Aboelkhair H & Rabei M 2012. Radioelement mapping and environmental monitoring of surface deposits using ground γ - ray photon spectrometry of the area adjacent to El-Ramlah Village, southwestern Sinai, Egypt. *Resource Geology* 62, 2: 215-224.
- Abusini M, Al-ayasreh K & Al-Jundi J 2008. Determination of Uranium, thorium and potassium activity concentrations in soil cores in Araba Valley, Jordan. *Radiation Protection Dosimetry* 128, 2: 213-216.
- Agbalagba EO & Onoja R.A 2011. Evaluation of natural radioactivity in soil, sediment and water samples of Niger Delta (Biseni) flood plain lakes, Nigeria. *Journal of Environmental Radioactivity* 102: 667-671.
- Ahmad TR 1997. Environmental terrestrial gamma radiation dose and its relationship with soil type and underlying geological formations in Pontian District, Malaysia. *Applied Radiation and Isotopes* 48, 3: 407-417.
- Ahnert F 1996. *Introduction to geomorphology*. London: Arnold Publishers.
- Al-Hilal M & Al-Ali A 2016. Investigation for uranium dispersion adjacent to cretaceous phosphatic outcrops in Al-Nassrieh Basin, Southern Pamyrides, Syria. *Journal of Earth Science* 27, 5: 786-794.
- Allsopp HL & Kolbe P 1965. Isotopic age determinations on the Cape Granite and intruded Malmesbury sediments, Cape Peninsula, South Africa. *Geochimica et Cosmochimica Acta* 29: 1115-1130.
- Al-Sharkawy A, Hiekal MTh, Sherif MI & Badran HM 2012. Environmental assessment of gamma-radiation levels in stream sediments around Sharm El-Sheikh, South Sinai, Egypt. *Journal of Environmental Radioactivity* 112: 76-82.
- Arafa W 2004. Specific activity and hazards of granite samples collected from the Eastern Desert of Egypt. *Journal of Environmental Radioactivity* 75: 315-327.
- Attix G.H. 2004. *Introduction to radiological physics and radiation dosimetry*. Wiley-VCH.

- Baranwal VC, Sharma SP, Sengupta D, Sandilya MK, Bhaumik BK, Guin R & Saha SK 2006. A new background radiation area in the geothermal region of Eastern Ghats Mobile Belt (EGMB) of Orissa, India. *Radiation Measurements* 41: 602-610
- Barbarin B 1999. A review of the relationships between granitoid types, their origins and their geodynamic environments. *Lithos* 46: 605-626.
- Baré J & Tondeur F 2011. Gamma spectrum unfolding for a NaI monitor of radioactivity in aquatic systems: Experimental evaluations of the minimal detectable activity. *Applied Radiation and Isotopes* 69: 1121-1124.
- Beamish D 2013. γ - ray photon attenuation in the soils of Northern Ireland, with special reference to peat. *Journal of Environmental Radioactivity* 115: 13-27.
- Beamish D 2014. Environmental radioactivity in the UK: the airborne geophysical view of dose rate estimates. *Journal of Environmental Radioactivity* 138: 249-263.
- Bezuidenhout J 2012. Mapping of historical human activities in the Saldanha Bay Military Area by using *In Situ* γ - ray photon Measurements. *Scientia Militaria* 40, 2: 1-24.
- Bezuidenhout J 2015a. In situ γ - ray photon measurements of radionuclides at a disused phosphate mine on the West Coast of South Africa. *Journal of Environmental Radioactivity* 150: 1-8.
- Bezuidenhout J 2015b. Testing and implementation of a transportable and robust radio-element mapping system. *South African Journal of Science* 111, 9/10: 153-159.
- Böhlke JK, De Laeter JR, De Bièvre P, Hidaka H, Peiser HS, Rosman KJR & Taylor PDP 2005. Isotopic compositions of the elements, 2001. *Journal of Physical and Chemical Reference Data* 34, 1: 57-67.
- Briggs D & Smithson P 1985. *Fundamentals of physical geography*. London: Century Hutchinson.
- Chang K 2012. Introduction to Geographic Information Systems. 6th ed. New York: McGraw-Hill.
- Chappel BW & White AJR 1974. Two contrasting granite types. *Pacific Geology* 8: 173-174.
- Chiozzi P, Pasquale V, Verdoya M & De Felice P 2000. Practical applicability of field γ -ray scintillation spectrometry in geophysical surveys. *Applied Radiation and Isotopes* 53: 215-220.
- CIAAW 2013. Isotopic abundances [online]. Available from <http://www.ciaaw.org/isotopic-abundances.htm> [Accessed 11 November 2015].
- Congalton RG & Green K 2008. *Assessing the Accuracy of Remotely Sensed Data: Principles and*

Practices. 2nd ed. Boca Raton: CRC Press.

- Corner B, Toens PD, Richards DJ, Van As D & Vleggaar CM 1979. *The Pelindaba facilities for calibrating radiometric field instruments. No PEL-268*. Pretoria: Publication of Atomic Energy Board.
- Corner B, Toens PD, Richards DJ, Van As D & Vleggaar CM 1979. The Pelindaba facilities for calibrating radiometric field instruments. Publication of Atomic Energy Board, No. PEL-268, Pretoria.
- Croft S & Hutchinson IG 1999. The measurement of U, Th and K concentrations in building materials. *Applied Radiation and Isotopes* 51: 483-492.
- CSIR 2014. *Environmental screening study for a proposed LNG terminal at Saldanha an associated pipeline infrastructure to Atlantis and Cape Town, Western Cape, South Africa*. Prepared for the Western Cape Government, Department of Economic Development and Tourism. Report Number CSIR/CAS/EMS/ER/2014/0012/B. Stellenbosch: Council for Scientific and Industrial Research.
- De Blij HJ 1980. *The earth: A topical geography*. 2nd ed. New York: John Wiley & Sons.
- De La Roche H, Leterrier J, Grandclaude P & Marchal M 1980. A classification of volcanic and plutonic rocks using R₁R₂-diagram and major element analysis – its relationships with current nomenclature. *Chemical Geology* 29: 183-210.
- De Meijer RD 1998. Heavy minerals: from ‘Edelstein’ to Einstein. *Journal of Geochemical Exploration* 62: 81-103.
- De Villiers D 2011. Characterisation of heavy mineral sands and soils by radiometry and its use in mineral beneficiation and agriculture. PhD Dissertation. Stellenbosch: University of Stellenbosch.
- Din KS 2009. Estimation of heat generation by radioactive decay of some phosphate rocks in Egypt. *Applied Radiation and Isotopes* 67: 2033-2036.
- Dobos E, Micheli E, Baumgardner MF, Biehl L & Helt T 2000. Use of combined digital elevation model and satellite radiometric data for regional soil mapping. *Geoderma* 97: 367-391.
- El-Taher A & Madkour HA 2011. Distribution and environmental impacts of metals and natural radionuclides in marine sediments in-front of different wadies mouth along the Egyptian Red

- Sea Coast. *Applied Radiation and Isotopes* 69: 550-558.
- Etienne S 2002. The role of biological weathering in periglacial areas: a study of weathering rinds in south Iceland. *Geomorphology* 47: 75-86.
- FLIR 2015. Available from <http://www.flir.com/threatdetection/display/?id=65349>. [Accessed 1 December 2015].
- Franceschini G & Compton JS 2004. Aeolian and marine deposits of the Tabakbaai Quarry area, Western Cape, South Africa. *South African Journal of Geology* 107: 619-632.
- Franke R 1982. Smooth interpolation of scattered data by local thin plate splines. *Computers and Mathematics with Applications* 8, 4: 273-281.
- Frost RB, Barnes CG, Collins WJ, Arculus RJ, Ellis DJ & Frost DC 2001. A geochemical classification for granitic rocks. *Journal of Petrology*. 42, 11: 2033-2048.
- Ghiassi-nejad M, Mortazavi SMJ, Cameron JR, Niroomand-rad A & Karam PA 2001. Very high background radiation areas of Ramsar, Iran: Preliminary Biological Studies. *Health Physics* 82, 1: 87-93.
- Google Earth 2016. *Saldanha 33°02'31.28''S and 17°54'47.14''E*. [Accessed 3 November 2016].
- Goossens D 2006. Aeolian deposition of dust over hills: The effect of dust grain size on the deposition pattern. *Earth Surface Processes and Landforms* 31: 762-776.
- Greyling AW 2001. 'n Geografiese inligtingstelsel as bestuurhulpmiddel vir die SAS SALDANHA natuureservaat. Honours research report. Saldanha: Stellenbosch University, Faculty Military Science, School for Geospatial Studies and Information Systems, Department of Military Geography.
- Hall K, Joselito MA, Boelhouwers J & Liping Z 2005. The influence of aspect on the biological weathering of granites: observations from the Kunlun Mountains, China. *Geomorphology* 67: 171-188.
- Harden CP 2006. Human impacts on headwater fluvial systems in the northern and central Andes. *Geomorphology* 79: 249-263.
- Hendriks PHGM 2003. In-depth γ - ray photon studies: Borehole measurements. Doctoral dissertation. Groningen: University of Groningen, Faculty of Mathematics and Natural Sciences.

- Hendriks PHGM, Limburg J & de Meijer RJ 2001. Full-spectrum analysis of natural gamma-ray spectra. *Journal of Environmental Radioactivity* 53: 365-380.
- Hess D 2014. *Mcknight's Physical Geography: A Landscape Appreciation*. 11th ed. New Jersey: Pearson Education, Inc.
- Hulbert IAR & French J 2001. The accuracy of GPS for wildlife telemetry and habitat mapping. *Journal of Applied Ecology* 38: 869-878.
- IAEA (International Atomic Energy Agency) 2003. *Guidelines for radioelement mapping using γ -ray photon spectrometry data*. Vienna: International Atomic Energy Agency (IAEA-TECDOC-1363).
- Ishihara S 1977. The magnetite-series and ilmenite-series granitic rocks. *Mining Geology* 27: 293-305.
- Jibiri NN & Farai IP 2005. Application of in-situ gamma-ray spectrometry in the determination of activity concentrations of ^{40}K , ^{238}U and ^{232}Th and mean annual effective dose rate levels in southeastern cities in Nigeria. *Radioprotection* 40, 4: 489-501.
- Jones WK & Carroll TR 1983. Error analysis of airborne gamma radiation soil moisture measurements. *Agricultural Meteorology* 28: 19-30.
- Karam PA 2002. *The high background radiation area in Ramsar Iran: Geology, NORM, Biology, LNT, and possible regulatory fun*. Paper (delivered) at the WM'02 Conference, Tucson.
- Kilpatrick JA & Ellis DJ 1992. C-type magmas: Igneous charnockites and their extrusive equivalents. *Transactions of the Royal Society of Edinburgh: Earth Sciences* 83: 155-164.
- Knoll GF 2000. *Radiation detection and measurement*. 3rd ed. Hoboken: John Wiley & Sons.
- Kostitsyn YA, Volkov VN & Zhuravlev DZ 2007. Trace elements and evolution of granite melt as exemplified by the raumid pluton, southern pamirs. *Geochemistry International* 45, 10: 971-982.
- Lahham A, Hussein A & Judeh A 2009. Study of environmental radioactivity in Palestine by in situ gamma-ray spectroscopy. *Radiation Protection Dosimetry* 135, 1: 43-46.
- Le Bas MJ & Streckeisen AL 1991. The IUGS systematics of igneous rocks. *Journal of the Geological Society*. 148: 825-833.
- Li J, Li Y, Wang Y & Wu J 2010. Applicability study of using in-situ gamma-ray spectrometry

- technique for ^{137}Cs and $^{210}\text{Pb}_{\text{ex}}$ inventories measurement in grassland environments. *Applied Radiation and Isotopes* 68: 1143-1149.
- Llope WJ 2011. Activity concentrations and dose rates from decorative granite countertops. *Journal of Environmental Radioactivity* 102: 620-629.
- Loiselle MC & Wones DS 1979. Characteristics and origin of anorogenic granites. *Geological Society of America, Abstracts with Programs*. 11: 468.
- Macdonald WG, Rozendaal A & de Meijer RJ 1997. Radiometric characteristics of heavy mineral deposits along the west coast of South Africa. *Mineralium Deposita* 32: 371-381.
- Maphoto KP 2004. Determination of natural radioactivity concentrations in soil: A comparative study of windows and full spectrum analysis. Master's thesis. Cape Town: University of the Western Cape, Department of Physics.
- Marshak S 2001. *Earth: Portrait of a planet*. New York: W. W. Norton & Company.
- Michel J 1984. Redistribution of uranium and thorium series isotopes during isovolumetric weathering of granite. *Geochimica et Cosmochimica Acta* 48: 1249-1255.
- Monkhouse FJ & Small J 1978. *A dictionary of the natural environment*. London: Edward Arnold.
- Montes ML, Mercader RC, Taylor MA, Runco J & Desimoni J 2012. Assessment of natural radioactivity levels and their relationship with soil characteristics in undisturbed soils of the northeast of Buenos Aires province, Argentina. *Journal of Environmental Radioactivity* 105: 30-39.
- Moses C, Robinson D & Barlow J 2014. Methods for measuring rock surface weathering and erosion: A critical review. *Earth-Science Reviews* 135: 141-161.
- Moussa M 2001. Gamma-ray spectrometry: a new tool for exploring archaeological sites; a case study from East Sinai, Egypt. *Journal of Applied Geophysics* 48: 137-142.
- National Geospatial Intelligence Agency 2016. Defense Mapping Agency Technical Manual 8358.1 Datums, Ellipsoids, Grids, and Grid Reference Systems. Online: <http://earth-info.nga.mil/GandG/publications/tm8358.1/tr83581b.html#ZZ26> [Accessed 24 October 2016].
- Newman RT, Lindsay R, Maphoto KP, Mlwilo NA, Mohanty A.K, Roux DG, de Meijer RJ & Hlatshwayo IN 2008. Determination of soil, sand and ore primordial radionuclide concentrations by full-spectrum analysis of high purity germanium detector spectra. *Applied*

Radiation and Isotopes 66: 855-859.

Noncolela SP 2011. Calibration of a NaI(Tl) detector for low level counting of naturally occurring radionuclides in soil. Master's thesis. University of the Western Cape, Physics Department.

Obhodaš J, Valković V 2010. Contamination of the coastal sea sediments by heavy metals. *Applied Radiation and Isotopes* 67: 807-811.

Ohanian HC 1995. *Modern Physics*. 2nd ed. Englewood Cliffs: Prentice Hall.

Pearce JA, Harris NBW & Tindle AG 1984. Trace element discrimination diagrams for the tectonic interpretation of granitic rocks. *Journal of Petrology* 25: 956-983.

Phillips DJ 2005. Weathering instability and landscape evolution. *Geomorphology* 67: 255-272.

Provincial Government of the Western Cape 2005. *Western Cape provincial spatial development framework: The Western Cape province today and tomorrow*. Cape Town: Department of Environmental Affairs and Development Planning (Statutory report).

Ramli AT 1997. Environmental terrestrial gamma radiation dose and its relationship with soil type and underlying geological formations in Pontian district, Malaysia. *Applied Radiation and Isotopes* 48, 3: 407-412.

Reynolds JM 2011. *An introduction to applied and environmental geophysics*. 2nd ed. Chichester: Wiley-Blackwell.

Roberts DL & Brink JS 2002. Dating and correlation of Neogene coastal deposits in the Western Cape (South Africa): Implications for Neotectonism. *South African Journal of Geology* 105: 337-352.

Rodrigues-Navarro C & Doehne E 1999. Salt weathering: influence of evaporation rate, supersaturation and crystallization pattern. *Earth Surface Processes and Landforms* 24: 191-209.

Rozendaal A, Philander C & De Meijer RJ 1999. *Mineralogy of heavy mineral placers along the West Coast of South Africa*. Johannesburg: The South African Institute of Mining and Metallurgy, Symposium Series S23.

Ruffel A, McKinley JM, Lloyd CD & Graham C 2006. Th/K and T/U ratios from spectral gamma-ray surveys improve the mapped definition of subsurface structures. *Journal of Environmental & Engineering Geophysics* 11, 1: 53-61.

- Ruxton BP & Berry L 1957. Weathering of granite and associated erosional features in Hong Kong. *Geological Society of America Bulletin* 68, 10: 1263-1292.
- Scheepers R & Armstrong R. 2002. NewU-PB SHRIMP zircon ages of the Cape Granite Suite: Implications for the magmatic evolution of the Saldania Belt. *South African Journal of Geology* 105, 3: 241-256.
- Scheepers R 1995. Geology, geochemistry and petrogenesis of Late Precambrian S-, I- and A-type granitoids in the Saldania belt, Western Cape Province, South Africa. *Journal of African Earth Sciences* 21, 1: 35-58.
- Sharma PV 1997. *Environmental and engineering geophysics*. Cambridge: Cambridge University Press.
- Sorrel CA & Sandstorm GF 1982. *The rocks and minerals of the world*. Glasgow: William Collins Sons & Co.
- South Africa 1987. *South Africa 1:50 000 sheet 3219CA Citrusdal*. Second edition. (Map). Cape Town: Chief Directorate of Surveys and Mapping.
- South Africa 1997. *South Africa 1:10 000 orthophoto map series 3317BB 3 & 4 & 9 Saldanha*. Third edition. (Map). Cape Town: Chief Directorate of Surveys and Mapping.
- South Africa n.d. *South Africa 1:50 000 sheet 3317BB & 3318AA Saldanha*. Cape Town: Chief Directorate of Surveys and Mapping.
- Sowa W, Martini W, Gehrcke K, Marschner P & Naziry MJ 1989. Uncertainties of in situ gamma spectrometry for environmental monitoring. *Radiation Protection Dosimetry* 27, 2: 93-101.
- Stanford School of Medicine 2004. Changing variables from continuous to categorical. Stanford University. Available from <http://cliomods.stanford.edu/trailmaps/sample/cohort/changingVariables/index.html> [Accessed 01 November 2016].
- Strahler AH & Strahler AN 1992. *Modern physical geography*. 4th ed. New York: John Wiley & Sons.
- Syvitski PPM, Vörösmarty CJ, Kettner AJ & Green P 2005. Impact of humans on the flux of terrestrial sediment to the global coastal ocean. *Science* 308: 376-380.
- Tetley L & Calcutt D 2001. *Electronic Navigation Systems*. London: Routledge.

Trimble 2015. Available from

http://www.trimble.com/mappingGIS/yuma2_rugged_tablet.aspx?tab=Technical_Support.

[Accessed 1 December 2015].

Turkington AV, Phillips JD & Campbell SW 2005. Weathering and landscape evolution.

Geomorphology 67: 1-6.

Tyler AN 1999. Monitoring anthropogenic radioactivity in salt marsh environments through in situ

gamma-ray spectrometry. *Journal of Environmental Radioactivity* 45: 235-252.

Tyler AN 2004. High accuracy in situ radiometric mapping. *Journal of Environmental Radioactivity*

72: 195-202.

Tyler AN, Davidson DA & Grieve IC 2001. In situ radiometric mapping of soil erosion and field-

moist bulk density on cultivated fields. *Soil Use and Management* 17: 88-96.

Tzortzis M, Svoukis E & Tsetos H 2004. A comprehensive study of natural gamma radioactivity

levels and associated dose rates from surface soils in Cyprus. *Radiation Protection Dosimetry* 109, 3: 217-224.

Tzortzis M, Tsertos H, Christofides S & Christodoulides D 2003. Gamma-ray measurements of

naturally occurring radioactive samples from Cyprus characteristic geological rocks. *Radiation Measurements* 37: 221-229.

UNSCEAR 2000. *Sources and effects of ionizing radiation. United Nations scientific committee on*

the effects of atomic radiation. Report to the General Assembly on the Effects of Atomic Radiation. United Nations, New York.

UNSCEAR 2008. *Sources and effects of ionizing radiation. United Nations scientific committee on*

the effects of atomic radiation. Report to the General Assembly with Scientific Annexes. Volume 1. United Nations, New York.

Van der Graaf ER, Koomans RL, Limburg J & De Vries K 2007. In situ radiometric mapping as a

proxy of sediment contamination: Assessment of the underlying geochemical and –physical principles. *Applied Radiation and Isotopes* 65: 619-633.

Van Wijngaarden M, Venema LB & De Meijer RJ 2002a. Radiometric sand-mud characterization

in the Rhine-Meuse estuary Part B. In situ mapping. *Geomorphology* 43: 103-116.

Van Wijngaarden M, Venema LB, De Meijer RJ, Zwolsman JJG, Van Os B & Gieske JMJ 2002b.

- Radiometric sand-mud characterization in the Rhine-Meuse estuary Part A. Fingerprinting. *Geomorphology* 43: 87-101.
- Villaros A, Stevens G, Moyon J & Buick IS 2009. The trace element compositions of S-type granites: evidence for disequilibrium melting and accessory phase entrainment in the source. *Contributions to Mineralogy and Petrology* 158, 4: 543-561.
- Von Blanckenburg F 2005. The control mechanisms of erosion and weathering at basin scale from cosmogenic nuclides in river sediment. *Earth and Planetary Science Letters* 237: 462-479.
- Wang Z 2002. Natural radiation environment in China. *International Congress Series* 1225: 39-46.
- Welch SA & McPhail DC 2003. Mobility of major and trace elements during biologically mediated weathering of granite. In Roach IC (ed) *Advances in Regolith: Proceedings of the Cooperative Research Centre for Landscape Environments and Mineral Exploration (CRC LEME) Regional Regolith Symposia*, 437-440. CRC LEME.
- White AJR 1979. Sources of granite magmas. *Geological Society of America, Abstracts with Programs* 11: 539.
- Wilford J 2002. Airborne Gamma-Ray Spectrometry. In Papp, E. (ed.) *Geophysical and Remote Sensing Methods for Regolith Exploration*, pp 46-52. Canberra: Cooperative Research Centre for Landscape Environments and Mineral Exploration.
- Williams RBG & Robinson DA 2000. Effects of aspect on weathering: Anomalous behavior of sandstone gravestones in southeast England. *Earth Surface Processes and Landforms* 25: 135-144.
- Wilson RJ 2010. *Mineral and rocks*. n.p. Richard Wilson & Ventus Publishing & bookboon.com.
- Windfinder. Windstats [Online]. Available from http://www.windfinder.com/windstats/windstatistic_langebaan.htm&fspt=saldanha. [Accessed 7 February 2013].
- Woo M & Luk S 1990. Vegetation effects on soil and water losses on weathered granitic hillslopes, south China. *Physical Geography* 11, 1: 1-16.

PERSONAL COMMUNICATIONS

Schloms B 2012. Information shared with A.P. Geysler during a personal conversation on 16 February 2012.

Flügel T 2013. Information shared with A.P. Geysler during a personal conversation on 4 February 2013.

APPENDICES**APPENDIX A: COORDINATE AND CONCENTRATIONS TABLE**

Name	POINT_Y Dec Deg	POINT_X Dec Deg	True Y Dec Deg	True X Dec Deg	⁴⁰ K Bq/kg	²³² Th Bq/kg	²³⁸ U Bq/kg	Notes
A01	-33.04555722760	17.90774582080	-33.04558700000	17.90779000000	1266	54	31	
A02	-33.04555722760	17.90826563030	-33.04564900000	17.90825500000	1148	77	22	
A03	-33.04555722760	17.90878543980	-33.04557250000	17.90876717000	1136	48	39	
A04	-33.04555722760	17.90930524940	-33.04551367000	17.90931367000	1196	40	30	
A05	-33.04555722760	17.90982505890	-33.04550300000	17.90977783000	1152	44	26	
A06	-33.04555722760	17.91034486840	-33.04556550000	17.91030417000	1111	36	30	
A07	-33.04555722760	17.91086467790	-33.04558133000	17.91086117000	1119	36	32	
A08	-33.04555722760	17.91138448740	-33.04557867000	17.91130283000	990	31	27	
A09	-33.04555722760	17.91190429700	-33.04554867000	17.91182767000	1178	28	29	
A10	-33.04555722760	17.91242410650	-33.04559000000	17.91240700000	1192	38	19	
A11	-33.04555722760	17.91294391600	-33.04550067000	17.91282633000	509	29	31	Wetland; soil still wet; clay type soil; at edge of wetland
A12	-33.04555722760	17.91346372550	-33.04551000000	17.91315383000	1322	30	24	Sand
A13	-33.04555722760	17.91398353510	-33.04547200000	17.91386467000	1149	36	28	
A14	-33.04555722760	17.91450334460	-33.04555117000	17.91438367000	1207	49	52	
A15	-33.04555722760	17.91502315410	-33.04554830000	17.91494250000	1117	33	38	
A16	-33.04555722760	17.91554296360	-33.04551350000	17.91554517000	1161	56	34	Light soil; to side of wetland
A17	-33.04555722760	17.91606277320	-33.04559799000	17.91593583000	1223	40	37	Different type of soil; soil lighter in colour (silk); wetland

A18	-33.04555722760	17.91658258270	-33.04555933000	17.91640900000	768	35	20	Some rocks; soil lighter in colour
A19	-33.04555722760	17.91710239220	-33.04554300000	17.91701333000	774	34	13	Rock +- 15cm below surface
A20	-33.04555722760	17.91762220170	-33.04558800000	17.91739200000	621	28	16	Between Calcite rocks and shells; darker soil; rock +- 15cm below surface
A21	-33.04555722760	17.91814201130	-33.04556650000	17.91787583000	574	27	13	Between Calcite rocks and shells; darker soil, rock +- 15cm below surface
B01	-33.04512779010	17.90774582080	-33.04515700000	17.90767767000	1149	50	41	
B02	-33.04512779010	17.90826563030	-33.04504617000	17.90830333000	1150	43	25	A few rocks in the vicinity of measurement between 1 - 3m from detector
B03	-33.04512779010	17.90878543980	-33.04516483000	17.90863567000	1185	39	40	
B04	-33.04512779010	17.90930524940	-33.04514067000	17.90927483000	1103	51	28	
B05	-33.04512779010	17.90982505890	-33.04513267000	17.90982200000	1174	43	31	
B06	-33.04512779010	17.91034486840	-33.04512033000	17.91026817000	1128	44	34	
B07	-33.04512779010	17.91086467790	-33.04505617000	17.91079417000	1232	43	38	
B08	-33.04512779010	17.91138448740	-33.04511733000	17.91126667000	1148	45	30	
B09	-33.04512779010	17.91190429700	-33.04514833000	17.91193450000	1252	43	25	
B10	-33.04512779010	17.91242410650	-33.04512417000	17.91238800000	1221	40	32	Soil ard and compact
B11	-33.04512779010	17.91294391600	-33.04511767000	17.91293483000	1422	37	36	At the edge of wetland
B12	-33.04512779010	17.91346372550	-33.04517233000	17.91358200000	1160	30	34	Soil is hard and compact at surface, +- 2cm thick crust
B13	-33.04512779010	17.91398353510	-33.04514883000	17.91398850000	1156	34	34	
B14	-33.04512779010	17.91450334460	-33.04513550000	17.91457550000	1152	41	29	Soil hard and compact

B15	-33.04512779010	17.91502315410	-33.04516183000	17.91511450000	1210	44	25	Soil hard and compact
B16	-33.04512779010	17.91554296360	-33.04514950000	17.91559500000	1134	41	26	Soil hard and compact
B17	-33.04512779010	17.91606277320	-33.04517350000	17.91616700000	1136	38	34	
B18	-33.04512779010	17.91658258270	-33.04509550000	17.91662800000	1183	54	36	Measurement taken 1m from side of the road
B19	-33.04512779010	17.91710239220	-33.04508900000	17.91715667000	1171	56	38	Light soil
B20	-33.04512779010	17.91762220170	-33.04508933000	17.91768783000	564	28	10	Between Calcite rocks and shells; darker soil; rock +/- 5cm below surface
B21	-33.04512779010	17.91814201130	-33.04510250000	17.91810800000	650	25	12	Between Calcite rocks and shells; darker soil
C01	-33.04469835260	17.90774582080	-33.04470050000	17.90769317000	1187	40	33	Much digging activity in the vicinity – moles
C02	-33.04469835260	17.90826563030	-33.04466400000	17.90816967000	1102	38	30	Soil hard and compact
C03	-33.04469835260	17.90878543980	-33.04471150000	17.90870667000	1107	38	29	
C04	-33.04469835260	17.90930524940	-33.04468500000	17.90931133000	1183	48	25	
C05	-33.04469835260	17.90982505890	-33.04468183000	17.90982167000	1145	57	32	
C06	-33.04469835260	17.91034486840	-33.04468350000	17.91031333000	1199	56	35	
C07	-33.04469835260	17.91086467790	-33.04472000000	17.91083267000	1214	57	32	
C08	-33.04469835260	17.91138448740	-33.04468650000	17.91130917000	1267	58	30	Between bushes
C09	-33.04469835260	17.91190429700	-33.04470617000	17.91192233000	1297	50	33	
C10	-33.04469835260	17.91242410650	-33.04469250000	17.91239733000	1446	36	35	
C11	-33.04469835260	17.91294391600	-33.04468733000	17.91294933000	1306	49	32	Soil hard and compact
C12	-33.04469835260	17.91346372550	-33.04472599000	17.91350133000	1196	47	26	Soil hard and compact
C13	-33.04469835260	17.91398353510	-33.04466933000	17.91396067000	1264	35	28	
C14	-33.04469835260	17.91450334460	-33.04469890000	17.91453200000	1262	53	40	
C15	-33.04469835260	17.91502315410	-33.04467400000	17.91504217000	1208	48	43	

C16	-33.04469835260	17.91554296360	-33.04469200000	17.91554350000	1086	58	28	
C17	-33.04469835260	17.91606277320	-33.04466783000	17.91606483000	1207	51	42	
C18	-33.04469835260	17.91658258270	-33.04469333000	17.91651800000	1168	56	46	
C19	-33.04469835260	17.91710239220	-33.04468150000	17.91714000000	1302	68	48	Next to boulder on the E side; darker soil
C20	-33.04469835260	17.91762220170	-33.04469411700	17.91763167000	938	49	20	Dark soil
C21	-33.04469835260	17.91814201130	-33.04471333000	17.91813717000	788	31	17	Darker soil; rock +- 10cm below surface; calcite rocks
D01	-33.04426891510	17.90774582080	-33.04427200000	17.90775467000	1201	31	30	
D02	-33.04426891510	17.90826563030	-33.04426083000	17.90828533000	1176	34	31	
D03	-33.04426891510	17.90878543980	-33.04426050000	17.90880517000	1216	39	24	
D04	-33.04426891510	17.90930524940	-33.04425817000	17.90933967000	1249	56	31	
D05	-33.04426891510	17.90982505890	-33.04426217000	17.90987367000	1366	101	130	Dense Bush; right next to boulder; rocks just below surface; small rocks in soil
D06	-33.04426891510	17.91034486840	-33.04428533000	17.91035883000	1380	64	80	Dense Bush, on and among rocks, boulders; rock at +- 15cm below surface
D07	-33.04426891510	17.91086467790	-33.04424300000	17.91085133000	997	92	56	Dense Bush; Darker Soil
D08	-33.04426891510	17.91138448740	-33.04426233000	17.91136300000	1359	68	45	Dense Bush
D09	-33.04426891510	17.91190429700	-33.04426733000	17.91194000000	1403	64	32	Top 10cm of soil hard and compact
D10	-33.04426891510	17.91242410650	-33.04426583000	17.91245833000	1408	70	37	
D11	-33.04426891510	17.91294391600	-33.04426900000	17.91296333000	1405	49	35	Ant nest underneath measurement
D12	-33.04426891510	17.91346372550	-33.04426783000	17.91343117000	1363	46	33	
D13	-33.04426891510	17.91398353510	-33.04427150000	17.91397783000	1360	56	32	Big boulder +- 5m E from detector

D14	-33.04426891510	17.91450334460	-33.04429050000	17.91454883000	1250	67	37	
D15	-33.04426891510	17.91502315410	-33.04426617000	17.91503983000	1299	71	41	
D16	-33.04426891510	17.91554296360	-33.04427800000	17.91552983000	1202	69	36	Soil hard and compact
D17	-33.04426891510	17.91606277320	-33.04425683000	17.91604483000	1257	58	37	Soil hard and compact
D18	-33.04426891510	17.91658258270	-33.04427183000	17.91657683000	1298	71	51	
D19	-33.04426891510	17.91710239220	-33.04427100000	17.91714067000	1365	60	25	In road
D20	-33.04426891510	17.91762220170	-33.04426383000	17.91765650000	1204	53	27	
D21	-33.04426891510	17.91814201130	-33.04426650000	17.91815517000	591	33	13	Rocks below surface; calcite rocks
E01	-33.04383947760	17.90774582080	-33.04386533000	17.90770617000	1068	35	28	
E02	-33.04383947760	17.90826563030	-33.04382650000	17.90831050000	1167	40	32	
E03	-33.04383947760	17.90878543980	-33.04384400000	17.90875533000	1268	41	37	
E04	-33.04383947760	17.90930524940	-33.04385417000	17.90928100000	1255	62	43	
E05	-33.04383947760	17.90982505890	-33.04399667000	17.90996650000	1161	85	72	
E06	-33.04383947760	17.91034486840	-33.04395133000	17.91030167000	1717	91	96	On and against rocks
E07	-33.04383947760	17.91086467790	-33.04382600000	17.91084617000	1396	83	54	
E08	-33.04383947760	17.91138448740	-33.04386383000	17.91137367000	1287	69	39	
E09	-33.04383947760	17.91190429700	-33.04384300000	17.91189783000	1410	80	47	
E10	-33.04383947760	17.91242410650	-33.04383883000	17.91244667000	1412	72	56	
E11	-33.04383947760	17.91294391600	-33.04383200000	17.91294550000	1422	66	39	
E12	-33.04383947760	17.91346372550	-33.04382967000	17.91342917000	1324	56	37	
E13	-33.04383947760	17.91398353510	-33.04384400000	17.91393133000	1243	100	54	
E14	-33.04383947760	17.91450334460	-33.04382417000	17.91450700000	1035	94	91	
E15	-33.04383947760	17.91502315410	-33.04383300000	17.91503283000	1274	84	45	Digging activity present

E16	-33.04383947760	17.91554296360	-33.04384650000	17.91551850000	1283	75	48	
E17	-33.04383947760	17.91606277320	-33.04384667000	17.91603717000	1223	100	47	
E18	-33.04383947760	17.91658258270	-33.04381600000	17.91650900000	1305	96	36	
E19	-33.04383947760	17.91710239220	-33.04385450000	17.91709517000	1262	64	38	
E20	-33.04383947760	17.91762220170	-33.04383983000	17.91764250000	1152	62	40	
E21	-33.04383947760	17.91814201130	-33.04383000000	17.91819550000	1056	49	32	
F01	-33.04341004010	17.90774582080	-33.04346167000	17.90786650000	1101	42	32	
F02	-33.04341004010	17.90826563030	-33.04341733000	17.90825900000	1143	36	33	
F03	-33.04341004010	17.90878543980	-33.04341350000	17.90878483000	1154	42	38	
F04	-33.04341004010	17.90930524940	-33.04349500000	17.90929383000	1311	59	36	
F05	-33.04341004010	17.90982505890	-33.04340767000	17.90987983000	1304	73	50	
F06	-33.04341004010	17.91034486840	-33.04339950000	17.91025467000	1331	67	54	Taken in a foot path
F07	-33.04341004010	17.91086467790	-33.04337000000	17.91086753000	1476	80	91	
F08	-33.04341004010	17.91138448740	-33.04343400000	17.91133400000	1194	86	41	
F09	-33.04341004010	17.91190429700	-33.04348400000	17.91193200000	1401	72	69	
F10	-33.04341004010	17.91242410650	-33.04344500000	17.91266000000	1510	75	48	
F11	-33.04341004010	17.91294391600	-33.04340233000	17.91294917000	1241	70	26	
F12	-33.04341004010	17.91346372550	-33.04342967000	17.91347517000	1247	86	48	
F13	-33.04341004010	17.91398353510	-33.04338600000	17.91396000000	1477	111	75	Thin layer of soil on top of rock
F14	-33.04341004010	17.91450334460	-33.04341167000	17.91452650000	1069	90	73	Rocky area, shallow soil on top of rock; much organic material in soil
F15	-33.04341004010	17.91502315410	-33.04341383000	17.91508367000	1218	89	51	
F16	-33.04341004010	17.91554296360	-33.04341900000	17.91551667000	1371	95	87	Top soil +/- 1 cm thick; rocks below surface

F17	-33.04341004010	17.91606277320	-33.04339533000	17.91610933000	1262	89	82	Shallow soil; rocks below surface
F18	-33.04341004010	17.91658258270	-33.04338500000	17.91654450000	1108	122	83	Rocks below surface
F19	-33.04341004010	17.91710239220	-33.04340767000	17.91708417000	1366	80	60	
F20	-33.04341004010	17.91762220170	-33.04341867000	17.91763717000	1331	78	43	
F21	-33.04341004010	17.91814201130	-33.04344300000	17.91815567000	1220	59	29	
G01	-33.04298060260	17.90774582080	-33.04300417000	17.90774633000	1045	50	30	
G02	-33.04298060260	17.90826563030	-33.04301767000	17.90829100000	1189	48	25	
G03	-33.04298060260	17.90878543980	-33.04299517000	17.90877283000	1170	54	45	
G04	-33.04298060260	17.90930524940	-33.04303200000	17.90922000000	1114	66	61	
G05	-33.04298060260	17.90982505890	-33.04313300000	17.90993817000	1114	83	64	MP taken out of position to be on the slope
G06	-33.04298060260	17.91034486840	-33.04302117000	17.91040767000	1147	56	54	MP on top of rock; measurement taken close to rock/boulder
G07	-33.04298060260	17.91086467790	-33.04303150000	17.91090999000	1227	70	67	
G08	-33.04298060260	17.91138448740	-33.04292067000	17.91120650000	1432	75	79	In between rocks; soil on top of rocks
G09	-33.04298060260	17.91190429700	-33.04293633000	17.91191633000	1278	79	76	In between rocks; soil on top of rocks
G10	-33.04298060260	17.91242410650	-33.04298317000	17.91246767000	1253	69	47	
G11	-33.04298060260	17.91294391600	-33.04295867000	17.91294100000	1379	64	23	
G12	-33.04298060260	17.91346372550	-33.04300917000	17.91337133000	1162	85	50	
G13	-33.04298060260	17.91398353510	-33.04297833000	17.91404650000	1062	82	78	
G14	-33.04298060260	17.91450334460	-33.04311550000	17.91452833000	1491	90	85	Taken on top of Granite Boulder
G15	-33.04298060260	17.91502315410	-33.04298350000	17.91500650000	1294	72	43	
G16	-33.04298060260	17.91554296360	-33.04310083000	17.91547067000	1429	88	82	Between boulders

G17	-33.04298060260	17.91606277320	-33.04299000000	17.91605117000	1260	98	75	
G18	-33.04298060260	17.91658258270	-33.04285683000	17.91625990000	1366	104	90	Between boulders
G19	-33.04298060260	17.91710239220	-33.04292133000	17.91716450000	1276	100	70	
G20	-33.04298060260	17.91762220170	-33.04300583000	17.91764950000	1333	79	39	
G21	-33.04298060260	17.91814201130	-33.04302467000	17.91812367000	1317	58	32	
H01	-33.04255116510	17.90774582080	-33.04255300000	17.90773433000	1073	52	23	
H02	-33.04255116510	17.90826563030	-33.04255217000	17.90826300000	1208	53	24	
H03	-33.04255116510	17.90878543980	-33.04254683000	17.90875283000	1229	80	22	Measurement taken next to large boulders; 3-8 m away
H04	-33.04255116510	17.90930524940	-33.04257167000	17.90936617000	1265	82	20	
H05	-33.04255116510	17.90982505890	-33.04251767000	17.90986133000	1303	74	43	Measurement taken +- 6m from boulder
H06	-33.04255116510	17.91034486840	-33.04253617000	17.91031650000	961	79	45	Measurement taken in between succulents (“vygies”)
H07	-33.04255116510	17.91086467790	-33.04255817000	17.91087033000	1173	74	55	Measurement taken next to bricks and road/gravel
H08	-33.04255116510	17.91138448740	-33.04254350000	17.91137183000	1600	84	38	
H09	-33.04255116510	17.91190429700	-33.04245883000	17.91197400000	1143	91	43	Off position due to rocks; between rocks and boulders
H10	-33.04255116510	17.91242410650	-33.04254900000	17.91249300000	1469	49	26	
H11	-33.04255116510	17.91294391600	-33.04251550000	17.91273767000	1194	62	46	Off position due to rocks
H12	-33.04255116510	17.91346372550	-33.04249583000	17.91322100000	1370	76	63	Off position due to rocks; close to boulders; thin layer of top soil +- 2cm on granite
H13	-33.04255116510	17.91398353510	-33.04255333000	17.91389100000	1047	75	65	Rocky area

H14	-33.04255116510	17.91450334460	-33.04254617000	17.91447700000	1341	87	69	Rocky area; organic matter in soil
H15	-33.04255116510	17.91502315410	-33.04255817000	17.91503550000	1195	74	60	
H16	-33.04255116510	17.91554296360	-33.04261150000	17.91560983000	1279	93	82	Soil overlying rocks
H17	-33.04255116510	17.91606277320	-33.04261150000	17.91600900000	1307	97	76	
H18	-33.04255116510	17.91658258270	-33.04252067000	17.91647033000	1355	99	86	
H19	-33.04255116510	17.91710239220	-33.04255883000	17.91692650000	1010	98	85	Rocky area against the Hill
H20	-33.04255116510	17.91762220170	-33.04252999000	17.91756017000	1379	79	53	
H21	-33.04255116510	17.91814201130	-33.04249000000	17.91813767000	1265	64	34	
J01	-33.04212172760	17.90774582080	-33.04211817000	17.90774899000	1182	57	17	
J02	-33.04212172760	17.90826563030	-33.04208417000	17.90826533000	1195	60	22	Point close to granite boulder; measurement taken +- 7m from boulder
J03	-33.04212172760	17.90878543980	-33.04210717000	17.90877817000	1293	57	28	
J04	-33.04212172760	17.90930524940	-33.04212033000	17.90932200000	1294	57	24	
J05	-33.04212172760	17.90982505890	-33.04210250000	17.90982333000	1343	60	31	
J06	-33.04212172760	17.91034486840	-33.04212283000	17.91033617000	1440	61	28	Digging activity present
J07	-33.04212172760	17.91086467790	-33.04212367000	17.91084617000	1330	74	48	Resembles a man-made gravel platform; different soil type (gravel)
J08	-33.04212172760	17.91138448740	-33.04201417000	17.91144817000	795	52	63	Measurement taken on top of ruin/building
J09	-33.04212172760	17.91190429700	-33.04211433000	17.91193617000	1147	70	38	
J10	-33.04212172760	17.91242410650	-33.04215000000	17.91234217000	1369	64	40	
J11	-33.04212172760	17.91294391600	-33.04208600000	17.91295250000	1292	63	45	
J12	-33.04212172760	17.91346372550	-33.04210900000	17.91340433000	1199	68	63	In-between rocks and boulders

J13	-33.04212172760	17.91398353510	-33.04209967000	17.91398000000	1311	83	65	3cm top soil on top of rocks; in-between rocks and boulders
J14	-33.04212172760	17.91450334460	-33.04204517000	17.91453100000	1320	98	54	Close to rocks and boulders
J15	-33.04212172760	17.91502315410	-33.04217567000	17.91495083000	1197	91	46	Close to rocks and boulders
J16	-33.04212172760	17.91554296360	-33.04219167000	17.91550950000	1350	99	49	
J17	-33.04212172760	17.91606277320	-33.04214900000	17.91604500000	1265	104	54	
J18	-33.04212172760	17.91658258270	-33.04217933000	17.91656500000	1026	127	85	On and among rocks; top soil +/- 5cm on top of rocks
J19	-33.04212172760	17.91710239220	-33.04212600000	17.91711517000	1042	110	61	
J20	-33.04212172760	17.91762220170	-33.04212183000	17.91761550000	1343	73	44	
J21	-33.04212172760	17.91814201130	-33.04211650000	17.91816167000	1163	55	42	
K01	-33.04169229010	17.90774582080	-33.04169500000	17.90776700000	1175	38	29	
K02	-33.04169229010	17.90826563030	-33.04170983000	17.90826733000	1170	43	32	
K03	-33.04169229010	17.90878543980	-33.04168817000	17.90875750000	1274	41	30	
K04	-33.04169229010	17.90930524940	-33.04169933000	17.90931500000	1283	43	32	
K05	-33.04169229010	17.90982505890	-33.04169417000	17.90984567000	1465	45	30	Soil relatively moist
K06	-33.04169229010	17.91034486840	-33.04168200000	17.91033717000	1388	70	36	
K07	-33.04169229010	17.91086467790	-33.04168150000	17.91085667000	1454	63	39	Rock/boulder +/- 2m North of detector
K08	-33.04169229010	17.91138448740	-33.04167150000	17.91138233000	1292	63	45	In-between rocks and boulders
K09	-33.04169229010	17.91190429700	-33.04165900000	17.91206467000	1104	74	54	Close to rocks and boulders
K10	-33.04169229010	17.91242410650	-33.04171900000	17.91244400000	1389	62	32	
K11	-33.04169229010	17.91294391600	-33.04171233000	17.91297383000	1443	62	28	
K12	-33.04169229010	17.91346372550	-33.04166300000	17.91343800000	1404	88	86	In-between rocks and boulders

K13	-33.04169229010	17.91398353510	-33.04156083000	17.91404000000	1417	83	94	In-between rocks and boulders
K14	-33.04169229010	17.91450334460	-33.04165500000	17.91467450000	1410	76	58	Out of position due to rocks and boulders; in-between rocks and boulders
K15	-33.04169229010	17.91502315410	-33.04168783000	17.91506867000	1255	90	69	Close to rocks and boulders
K16	-33.04169229010	17.91554296360	-33.04171648300	17.91542183000	1322	98	79	Close to rocks and boulders
K17	-33.04169229010	17.91606277320	-33.04160867000	17.91594383000	1302	100	75	rocks
K18	-33.04169229010	17.91658258270	-33.04170517000	17.91650617000	1329	96	83	
K19	-33.04169229010	17.91710239220	-33.04170133000	17.91711450000	1347	80	54	
K20	-33.04169229010	17.91762220170	-33.04167783000	17.91762217000	1345	61	43	
K21	-33.04169229010	17.91814201130	-33.04170867000	17.91814850000	1168	54	28	
L01	-33.04126285260	17.90774582080	-33.04126750000	17.90772800000	989	50	31	
L02	-33.04126285260	17.90826563030	-33.04126283000	17.90824333000	1043	50	20	
L03	-33.04126285260	17.90878543980	-33.04127583000	17.90877483000	1174	45	27	
L04	-33.04126285260	17.90930524940	-33.04126000000	17.90931283000	1328	38	27	
L05	-33.04126285260	17.90982505890	-33.04126600000	17.90983650000	1397	52	30	
L06	-33.04126285260	17.91034486840	-33.04126417000	17.91035267000	1299	50	37	
L07	-33.04126285260	17.91086467790	-33.04125000000	17.91083550000	1480	62	36	
L08	-33.04126285260	17.91138448740	-33.04131317000	17.91137767000	1216	109	46	In-between rocks and boulders
L09	-33.04126285260	17.91190429700	-33.04132150000	17.91205900000	1338	112	60	Close to rocks and boulders
L10	-33.04126285260	17.91242410650	-33.04120000000	17.91244083000	1467	87	86	On and among rocks; measurement taken out of position due to rocks
L11	-33.04126285260	17.91294391600	-33.04131750000	17.91317300000	1729	91	113	In-between rocks and boulders

L12	-33.04126285260	17.91346372550	-33.04127067000	17.91348767000	1415	90	58	Close to rocks and boulders
L13	-33.04126285260	17.91398353510	-33.04132700000	17.91398000000	1415	90	58	
L14	-33.04126285260	17.91450334460	-33.04132400000	17.91453700000	1051	109	88	
L15	-33.04126285260	17.91502315410	-33.04126250000	17.91501550000	1420	77	125	Close to rocks and boulders
L16	-33.04126285260	17.91554296360	-33.04135167000	17.91554817000	1585	89	136	Close to rocks and boulders
L17	-33.04126285260	17.91606277320	-33.04124800000	17.91605067000	1428	111	49	
L18	-33.04126285260	17.91658258270	-33.04126067000	17.91652700000	1580	69	57	
L19	-33.04126285260	17.91710239220	-33.04126817000	17.91712383000	1394	64	44	
L20	-33.04126285260	17.91762220170	-33.04127017000	17.91762200000	1275	58	23	
L21	-33.04126285260	17.91814201130	-33.04126983000	17.91813267000	1314	39	21	
M01	-33.04083341510	17.90774582080	-33.04081933000	17.90773900000	1187	41	32	
M02	-33.04083341510	17.90826563030	-33.04082483000	17.90828067000	1119	37	34	
M03	-33.04083341510	17.90878543980	-33.04080917000	17.90877300000	1176	40	33	
M04	-33.04083341510	17.90930524940	-33.04084267000	17.90932850000	1300	38	23	
M05	-33.04083341510	17.90982505890	-33.04084499000	17.90981733000	1315	48	26	
M06	-33.04083341510	17.91034486840	-33.04082750000	17.91032850000	1352	62	26	
M07	-33.04083341510	17.91086467790	-33.04084067000	17.91084867000	1433	68	30	
M08	-33.04083341510	17.91138448740	-33.04083317000	17.91138833000	1381	81	56	
M09	-33.04083341510	17.91190429700	-33.04083000000	17.91192917000	1304	94	53	
M10	-33.04083341510	17.91242410650	-33.04085183000	17.91244883000	1111	74	59	
M11	-33.04083341510	17.91294391600	-33.04081900000	17.91296333000	1333	90	74	Hard soil on top of mole run
M12	-33.04083341510	17.91346372550	-33.04083333000	17.91347717000	1445	86	33	
M13	-33.04083341510	17.91398353510	-33.04085160000	17.91398283000	1291	97	49	

M14	-33.04083341510	17.91450334460	-33.04083000000	17.91455900000	1340	77	66	
M15	-33.04083341510	17.91502315410	-33.04082517000	17.91509133000	1265	83	43	
M16	-33.04083341510	17.91554296360	-33.04085433000	17.91555450000	1471	71	47	
M17	-33.04083341510	17.91606277320	-33.04083699000	17.91605883000	1315	68	54	
M18	-33.04083341510	17.91658258270	-33.04082133000	17.91658283000	1460	62	41	
M19	-33.04083341510	17.91710239220	-33.04086000000	17.91711850000	1460	51	32	Measurement taken in the road
M20	-33.04083341510	17.91762220170	-33.04084800000	17.91764367000	1199	49	34	
M21	-33.04083341510	17.91814201130	-33.04085650000	17.91814000000	1297	49	25	
N01	-33.04040397760	17.90774582080	-33.04040467000	17.90776067000	1199	46	32	
N02	-33.04040397760	17.90826563030	-33.04039317000	17.90824600000	1110	45	30	
N03	-33.04040397760	17.90878543980	-33.04041767000	17.90878633000	982	45	25	
N04	-33.04040397760	17.90930524940	-33.04041667000	17.90928500000	1058	38	26	
N05	-33.04040397760	17.90982505890	-33.04040767000	17.90983867000	1402	32	27	
N06	-33.04040397760	17.91034486840	-33.04039550000	17.91032400000	1518	35	26	
N07	-33.04040397760	17.91086467790	-33.04042233000	17.91087717000	1555	40	36	Taken on top of a spider nest
N08	-33.04040397760	17.91138448740	-33.04040883000	17.91137167000	1434	56	49	Soil hard and compact
N09	-33.04040397760	17.91190429700	-33.04042567000	17.91191917000	1368	78	36	
N10	-33.04040397760	17.91242410650	-33.04042317000	17.91245900000	1294	60	48	
N11	-33.04040397760	17.91294391600	-33.04039000000	17.91294250000	1405	49	51	
N12	-33.04040397760	17.91346372550	-33.04041250000	17.91345583000	1443	53	46	
N13	-33.04040397760	17.91398353510	-33.04040167000	17.91396867000	1430	58	45	Taken in animal foot path
N14	-33.04040397760	17.91450334460	-33.04040417000	17.91452717000	1386	60	45	
N15	-33.04040397760	17.91502315410	-33.04041000000	17.91502767000	1258	71	45	

N16	-33.04040397760	17.91554296360	-33.04041133000	17.91554000000	1267	63	44	
N17	-33.04040397760	17.91606277320	-33.04039833000	17.91604050000	1254	55	35	
N18	-33.04040397760	17.91658258270	-33.04040350000	17.91658533000	1264	51	33	Hard clay type soil
N19	-33.04040397760	17.91710239220	-33.04041330000	17.91711567000	1402	47	32	
N20	-33.04040397760	17.91762220170	-33.04040200000	17.91767999000	1398	46	32	
N21	-33.04040397760	17.91814201130	-33.04039617000	17.91815233000	1383	53	27	Hard clay type soil
P01	-33.03997454010	17.90774582080	-33.03998583000	17.90776400000	1107	64	26	
P02	-33.03997454010	17.90826563030	-33.03997317000	17.90820817000	1200	62	29	Rocky area; soil hard and compact
P03	-33.03997454010	17.90878543980	-33.03998717000	17.90877133000	1141	37	23	
P04	-33.03997454010	17.90930524940	-33.03996183000	17.90933533000	1136	36	26	
P05	-33.03997454010	17.90982505890	-33.03995300000	17.90984950000	1176	32	24	
P06	-33.03997454010	17.91034486840	-33.03997150000	17.91035583000	1285	41	23	
P07	-33.03997454010	17.91086467790	-33.03996850000	17.91085617000	903	30	26	Taken in the road
P08	-33.03997454010	17.91138448740	-33.03997999000	17.91139033000	1322	54	25	
P09	-33.03997454010	17.91190429700	-33.03997117000	17.91195350000	1306	55	30	
P10	-33.03997454010	17.91242410650	-33.03998717000	17.91244117000	1410	47	29	
P11	-33.03997454010	17.91294391600	-33.03998383000	17.91294667000	1325	47	25	
P12	-33.03997454010	17.91346372550	-33.03998673300	17.91346250000	1313	49	32	
P13	-33.03997454010	17.91398353510	-33.03995167000	17.91398767000	1333	49	39	
P14	-33.03997454010	17.91450334460	-33.03996300000	17.91452117000	1355	50	38	
P15	-33.03997454010	17.91502315410	-33.03996250000	17.91505633000	1414	50	42	
P16	-33.03997454010	17.91554296360	-33.03997300000	17.91556433000	1360	45	51	
P17	-33.03997454010	17.91606277320	-33.03996550000	17.91604550000	1431	48	47	
P18	-33.03997454010	17.91658258270	-33.03998333000	17.91658217000	1536	58	47	

P19	-33.03997454010	17.91710239220	-33.03999183000	17.91711233000	1544	55	49	
P20	-33.03997454010	17.91762220170	-33.03996917000	17.91764087000	1422	63	38	
P21	-33.03997454010	17.91814201130	-33.03996200000	17.91812817000	1422	63	38	
Q01	-33.03954510260	17.90774582080	-33.03954583000	17.90772500000	1258	62	38	
Q02	-33.03954510260	17.90826563030	-33.03954500000	17.90823450000	1288	68	26	
Q03	-33.03954510260	17.90878543980	-33.03954883000	17.90876600000	1230	47	29	
Q04	-33.03954510260	17.90930524940	-33.03955917000	17.90929017000	1178	31	24	
Q05	-33.03954510260	17.90982505890	-33.03955000000	17.90984117000	1236	32	27	
Q06	-33.03954510260	17.91034486840	-33.03954333000	17.91034333000	1151	35	39	
Q07	-33.03954510260	17.91086467790	-33.03953617000	17.91084533000	1217	34	30	
Q08	-33.03954510260	17.91138448740	-33.03954000000	17.91134167000	1162	43	22	
Q09	-33.03954510260	17.91190429700	-33.03953350000	17.91190167000	1262	39	26	
Q10	-33.03954510260	17.91242410650	-33.03954267000	17.91245200000	1318	41	28	
Q11	-33.03954510260	17.91294391600	-33.03954367000	17.91294000000	1211	38	31	
Q12	-33.03954510260	17.91346372550	-33.03956400000	17.91344367000	1248	39	31	
Q13	-33.03954510260	17.91398353510	-33.03953800000	17.91394833000	1304	42	28	
Q14	-33.03954510260	17.91450334460	-33.03953567000	17.91451017000	1272	43	32	
Q15	-33.03954510260	17.91502315410	-33.03955483000	17.91496567000	1401	46	25	Taken +- 1m from the road
Q16	-33.03954510260	17.91554296360	-33.03954033000	17.91555050000	1427	62	47	
Q17	-33.03954510260	17.91606277320	-33.03953567000	17.91606850000	1518	57	40	
Q18	-33.03954510260	17.91658258270	-33.03953650000	17.91656133000	1641	53	33	
Q19	-33.03954510260	17.91710239220	-33.03959999000	17.91715850000	1426	60	54	
Q20	-33.03954510260	17.91762220170	-33.03954200000	17.91763167000	1353	57	38	
Q21	-33.03954510260	17.91814201130	-33.03954267000	17.91812417000	1555	42	37	

R01	-33.03911566510	17.90774582080	-33.03912000000	17.90776400000	1359	49	36	Flat rocky area
R02	-33.03911566510	17.90826563030	-33.03910817000	17.90826733000	1339	65	42	
R03	-33.03911566510	17.90878543980	-33.03913600000	17.90877200000	1372	46	37	
R04	-33.03911566510	17.90930524940	-33.03911017000	17.90930400000	1332	43	38	
R05	-33.03911566510	17.90982505890	-33.03909867000	17.90981000000	1321	28	24	Digging activity present
R06	-33.03911566510	17.91034486840	-33.03912217000	17.91035567000	1262	42	30	
R07	-33.03911566510	17.91086467790	-33.03911950000	17.91085833000	1087	38	28	
R08	-33.03911566510	17.91138448740	-33.03912467000	17.91133967000	1042	38	29	
R09	-33.03911566510	17.91190429700	-33.03909717000	17.91191450000	1087	37	26	
R10	-33.03911566510	17.91242410650	-33.03911000000	17.91243883000	1058	40	24	
R11	-33.03911566510	17.91294391600	-33.03911300000	17.91294200000	1097	40	26	Taken in road
R12	-33.03911566510	17.91346372550	-33.03911050000	17.91344233000	1097	40	26	
R13	-33.03911566510	17.91398353510	-33.03912133000	17.91395650000	1172	32	39	
R14	-33.03911566510	17.91450334460	-33.03912083000	17.91453250000	1352	51	34	
R15	-33.03911566510	17.91502315410	-33.03911467000	17.91502817000	1520	73	27	
R16	-33.03911566510	17.91554296360	-33.03910050000	17.91555900000	1556	74	45	
R17	-33.03911566510	17.91606277320	-33.03909667000	17.91601800000	1503	70	47	
R18	-33.03911566510	17.91658258270	-33.03912083000	17.91639183000	1432	75	34	
R19	-33.03911566510	17.91710239220	-33.03915500000	17.91707717000	1473	74	49	Close to rocks and boulders
R20	-33.03911566510	17.91762220170	-33.03911850000	17.91761750000	1409	49	37	
R21	-33.03911566510	17.91814201130	-33.03912150000	17.91814350000	1451	47	53	Close to rocks

APPENDIX B: ⁴⁰K ACTIVITY CALCULATIONS FROM NECSA CALIBRATIONS**SAMPLE K**

K₂O - Potassium 40	
Molar Mass (gmol)	94.1866
Molar Mass of Single K (gmol)	39.0983
%K in Molar Mass of K ₂ O	41.5115
% of K ₄₀ in K	0.0117
Molar mass of K ₄₀ (gmol)	0.0046
Avogadro's nr	6.0221E+23
1 Kg K ₂ O (nr molecules)	6.39384E+24
K atoms in 1 Kg K ₂ O	1.27877E+25
K ₄₀ atoms in 1 Kg K ₂ O (N)	1.49616E+21
T _{1/2} K ₄₀ (years)	1.28E+09
T _{1/2} K ₄₀ (seconds)	4.04E+16
Decay constant (λ)	1.72E-17
Activity (decays per second or Bq)	2.57E+04
Activity of 12.2% K ₂ O (Bq/kg)	3132.196745

U₃O₈ - Uranium 238	
Molar Mass (gmol)	842.0787
Molar Mass of Single U (gmol)	238.0289
%U in Molar Mass of U ₃ O ₈	84.80047
Avogadro's nr	6.02E+23
One ton of U ₃ O ₈ (nr of molecules)	7.15E+26
U ₂₃₈ atoms in one ton (N)	2.15E+27
T _{1/2} U ₂₃₈ (years)	4.47E+09
T _{1/2} U ₂₃₈ (seconds)	1.41E+17
Decay constant (λ)	4.91E-18
Activity (decays per second)	1.05E+10
Activity at 5 g/t	52711.27
Activity in Bq/kg	52.71127

ThO₂ - Thorium 232 (grams per ton)	
Molar Mass (gmol)	264.03606
Molar Mass of Single Th (gmol)	232.03806
%Th in Molar Mass of ThO ₂	87.88120077
Avogadro's nr	6.02214E+23
One ton of ThO ₂ (nr of molecules)	2.2808E+27
Th ₂₃₂ atoms in one ton (N)	2.2808E+27
T _{1/2} Th ₂₃₂ (years)	1.40E+10
T _{1/2} Th ₂₃₂ (seconds)	4.41806E+17
Decay constant (λ)	1.56889E-18
Activity (decays per second)	3578336316
Activity at 20 g/t	71566.72633
Activity in Bq/kg	71.56672633

APPENDIX C: ^{232}Th ACTIVITY CALCULATIONS FROM NECSA CALIBRATIONS**SAMPLE Th**

K₂O - Potassium 40	
Molar Mass (gmol)	94.1866
Molar Mass of Single K (gmol)	39.0983
%K in Molar Mass of K ₂ O	41.5115
% of K ₄₀ in K	0.0117
Molar mass of K ₄₀ (gmol)	0.0046
Avogadro's nr	6.0221E+23
1 Kg K ₂ O (nr molecules)	6.39384E+24
K atoms in 1 Kg K ₂ O	1.27877E+25
K ₄₀ atoms in 1 Kg K ₂ O (N)	1.49616E+21
T _{1/2} K ₄₀ (years)	1.28E+09
T _{1/2} K ₄₀ (seconds)	4.04E+16
Decay constant (λ)	1.72E-17
Activity (decays per second or Bq)	2.57E+04
Activity of 0% K ₂ O (Bq/kg)	0

U₃O₈ - Uranium 238	
Molar Mass (gmol)	842.07873
Molar Mass of Single U (gmol)	238.0289
%U in Molar Mass of U ₃ O ₈	84.80046753
Avogadro's nr	6.02214E+23
One ton of U ₃ O ₈ (nr of molecules)	7.15152E+26
U ₂₃₈ atoms in one ton (N)	2.14546E+27
T _{1/2} U ₂₃₈ (years)	4.47E+09
T _{1/2} U ₂₃₈ (seconds)	1.41E+17
Decay constant (λ)	4.91376E-18
Activity (decays per second)	10542253842
Activity at 326 g/t	3436774.753
Activity in Bq/kg	3436.774753

ThO₂ - Thorium 232 (grams per ton)	
Molar Mass (gmol)	264.03606
Molar Mass of Single Th (gmol)	232.03806
%Th in Molar Mass of ThO ₂	87.88120077
Avogadro's nr	6.02214E+23
One ton of ThO ₂ (nr of molecules)	2.2808E+27
Th ₂₃₂ atoms in one ton (N)	2.2808E+27
T _{1/2} Th ₂₃₂ (years)	1.40E+10
T _{1/2} Th ₂₃₂ (seconds)	4.41806E+17
Decay constant (λ)	1.56889E-18
Activity (decays per second)	3578336316
Activity at 14 320 g/t	51241776.05
Activity in Bq/kg	51241.77605

APPENDIX D: ²³⁸U ACTIVITY CALCULATIONS FROM NECSA CALIBRATIONS**SAMPLE U**

K₂O - Potassium 40	
Molar Mass (gmol)	94.1866
Molar Mass of Single K (gmol)	39.0983
%K in Molar Mass of K ₂ O	41.5115
% of K ₄₀ in K	0.0117
Molar mass of K ₄₀ (gmol)	0.0046
Avogadro's nr	6.0221E+23
1 Kg K ₂ O (nr molecules)	6.39384E+24
K atoms in 1 Kg K ₂ O	1.27877E+25
K ₄₀ atoms in 1 Kg K ₂ O (N)	1.49616E+21
T _{1/2} K ₄₀ (years)	1.28E+09
T _{1/2} K ₄₀ (seconds)	4.04E+16
Decay constant (λ)	1.72E-17
Activity (decays per second or Bq)	2.57E+04
Activity of 0.25% K ₂ O (Bq/kg)	64.18435953

U₃O₈ - Uranium 238	
Molar Mass (gmol)	842.07873
Molar Mass of Single U (gmol)	238.0289
%U in Molar Mass of U ₃ O ₈	84.80046753
Avogadro's nr	6.02214E+23
One ton of U ₃ O ₈ (nr of molecules)	7.15152E+26
U ₂₃₈ atoms in one ton (N)	2.14546E+27
T _{1/2} U ₂₃₈ (years)	4.47E+09
T _{1/2} U ₂₃₈ (seconds)	1.41E+17
Decay constant (λ)	4.91376E-18
Activity (decays per second)	10542253842
Activity at 4200 g/t	44277466.14
Activity in Bq/kg	44277.46614

ThO₂ - Thorium 232 (grams per ton)	
Molar Mass (gmol)	264.03606
Molar Mass of Single Th (gmol)	232.03806
%Th in Molar Mass of ThO ₂	87.88120077
Avogadro's nr	6.02214E+23
One ton of ThO ₂ (nr of molecules)	2.2808E+27
Th ₂₃₂ atoms in one ton (N)	2.2808E+27
T _{1/2} Th ₂₃₂ (years)	1.40E+10
T _{1/2} Th ₂₃₂ (seconds)	4.41806E+17
Decay constant (λ)	1.56889E-18
Activity (decays per second)	3578336316
Activity at 330 g/t	1180850.984
Activity in Bq/kg	1180.850984

APPENDIX E: AN EXTRACT OF THE BINNED VALUES OF ^{40}K ^{40}K

Energy channel	X2	X1	Y2	Y1	Binned Counts
331	332.7441261	329.4821	0.000655	0.00063	0.000641513
332	332.7441261	329.4821	0.000655	0.00063	0.000648993
333	336.0065162	332.7441	0.000610	0.000655	0.000651065
334	336.0065162	332.7441	0.000610	0.000655	0.000637407
335	336.0065162	332.7441	0.000610	0.000655	0.000623749
336	336.0065162	332.7441	0.000610	0.000655	0.000610092
337	339.2692292	336.0065	0.000622	0.000610	0.000613717
338	339.2692292	336.0065	0.000622	0.000610	0.000617457
339	339.2692292	336.0065	0.000622	0.000610	0.000621196
340	342.5322650	339.2692	0.000612	0.000622	0.000619946
341	342.5322650	339.2692	0.000612	0.000622	0.000616857
342	342.5322650	339.2692	0.000612	0.000622	0.000613768
343	345.7956238	342.5323	0.000617	0.000612	0.000612809
344	345.7956238	342.5323	0.000617	0.000612	0.000614271
345	345.7956238	342.5323	0.000617	0.000612	0.000615734
346	349.0593055	345.7956	0.000565	0.000617	0.000613676
347	349.0593055	345.7956	0.000565	0.000617	0.000597911
348	349.0593055	345.7956	0.000565	0.000617	0.000582146
349	349.0593055	345.7956	0.000565	0.000617	0.000566381
350	352.3233101	349.0593	0.000591	0.000565	0.000572784
351	352.3233101	349.0593	0.000591	0.000565	0.000580584
352	352.3233101	349.0593	0.000591	0.000565	0.000588385
353	355.5876376	352.3233	0.000549	0.000591	0.000582220
354	355.5876376	352.3233	0.000549	0.000591	0.000569383
355	355.5876376	352.3233	0.000549	0.000591	0.000556546
356	358.8522880	355.5876	0.000539	0.000549	0.000547729
357	358.8522880	355.5876	0.000539	0.000549	0.000544642

Energy 1	CC	Energy 2
627.65	0.000213	630.9439
630.94	0.000232	634.2357
634.24	0.000214	637.5278
637.53	0.000218	640.8202
640.82	0.000228	644.113
644.11	0.000213	647.406
647.41	0.000212	650.6994
650.70	0.000216	653.9931
653.99	0.000223	657.2872
657.29	0.000198	660.5815
660.58	0.000178	663.8762
663.88	0.000208	667.1712
667.17	0.000212	670.4665
670.47	0.000201	673.7622
673.76	0.000219	677.0582
677.06	0.000196	680.3545
680.35	0.00017	683.6511
683.65	0.000198	686.948
686.95	0.000198	690.2453
690.25	0.000192	693.5429
693.54	0.000191	696.8408
696.84	0.00019	700.139
700.14	0.000201	703.4376
703.44	0.000182	706.7364
706.74	0.000191	710.0356
710.04	0.000187	713.3352
713.34	0.000185	716.635

APPENDIX F: AN EXAMPLE OF THE STANDARD NORMALISED SPECTRA AND *IN SITU* SPECTRA DATA

	Sample K	Sample Th1	Sample U1
	Bq/kg	Bq/kg	Bq/kg
K ₄₀	3132.20	0.00	64.18
U ₂₃₈	52.71	3436.77	44277.47
Th ₂₃₂	71.57	51241.78	1180.85
Live T	601.89	280.33	404.54

Potassium 40				
Cal Coef	Channel	K Counts	Energy (keV)	Corrected Count (/Bq/sec)
0	1	0	-30.60	0.000000000
1.61E-04	2	0	-27.37	0.000000000
3.23E+00	3	0	-24.15	0.000000000
-	4	0	-20.92	0.000000000
3.38E+01	5	0	-17.69	0.000000000
	6	0	-14.47	0.000000000
	7	0	-11.24	0.000000000
	8	0	-8.01	0.000000000
	9	0	-4.78	0.000000000
	10	0	-1.55	0.000000000
	11	0	1.68	0.000000000
	12	0	4.91	0.000000000
	13	0	8.14	0.000000000
	14	0	11.37	0.000000000
	15	0	14.60	0.000000000
	16	0	17.83	0.000000000
	17	0	21.06	0.000000000
	18	0	24.29	0.000000000
	19	0	27.52	0.000000000
	20	0	30.75	0.000000000
	21	0	33.99	0.000000000
	22	4169	37.22	0.002211392
	23	4584	40.45	0.002431523
	24	5115	43.68	0.002713185

Thorium 232				
Cal Coef	Channel	K Counts	Energy (keV)	Corrected Count (/Bq/sec)
0	1	0	-18.03	0.000000000
2.10E-04	2	0	-14.98	0.000000000
3.04E+00	3	0	-11.94	0.000000000
-	4	0	-8.89	0.000000000
2.11E+01	5	0	-5.84	0.000000000
	6	0	-2.80	0.000000000
	7	0	0.25	0.000000000
	8	0	3.30	0.000000000
	9	0	6.35	0.000000000
	10	0	9.39	0.000000000
	11	0	12.44	0.000000000
	12	0	15.49	0.000000000
	13	0	18.54	0.000000000
	14	0	21.59	0.000000000
	15	0	24.64	0.000000000
	16	0	27.69	0.000000000
	17	0	30.75	0.000000000
	18	0	33.80	0.000000000
	19	0	36.85	0.000000000
	20	0	39.90	0.000000000
	21	0	42.96	0.000000000
	22	90944	46.01	0.006331116
	23	90078	49.06	0.006270829
	24	89898	52.12	0.006258299

Uranium 238				
Cal Coef	Channel	K Counts	Energy (keV)	Corrected Count (/Bq/sec)
0.00	1	0	-24.26	0.000000000
1.65E-04	2	0	-21.10	0.000000000
3.15E+00	3	0	-17.95	0.000000000
-	4	0	-14.79	0.000000000
2.74E+01	5	0	-11.64	0.000000000
	6	0	-8.48	0.000000000
	7	0	-5.33	0.000000000
	8	0	-2.17	0.000000000
	9	0	0.98	0.000000000
	10	0	4.14	0.000000000
	11	0	7.30	0.000000000
	12	0	10.45	0.000000000
	13	0	13.61	0.000000000
	14	0	16.77	0.000000000
	15	0	19.93	0.000000000
	16	0	23.08	0.000000000
	17	0	26.24	0.000000000
	18	0	29.40	0.000000000
	19	0	32.56	0.000000000
	20	0	35.72	0.000000000
	21	0	38.88	0.000000000
	22	178836	42.04	0.009984141
	23	188975	45.20	0.010550186
	24	202241	48.36	0.011290807

Recorded Spectrum					Live Time
					724.53
Cal Coef	Channel	Counts	Energy (keV)	Corrected Count (Cps)	
0.00E+00	1	0	-25.32	0.000000000	
1.01E-04	2	0	-22.29	0.000000000	
3.03E+00	3	0	-19.25	0.000000000	
-2.84E+01	4	0	-16.22	0.000000000	
	5	0	-13.18	0.000000000	
	6	0	-10.14	0.000000000	
	7	0	-7.11	0.000000000	
	8	0	-4.07	0.000000000	
	9	0	-1.04	0.000000000	
	10	0	2.00	0.000000000	
	11	0	5.04	0.000000000	
	12	19	8.07	0.026223897	
	13	13	11.11	0.017942666	
	14	18	14.15	0.024843692	
	15	28	17.18	0.038645743	
	16	96	20.22	0.132499689	
	17	304	23.26	0.419582350	
	18	822	26.30	1.134528591	
	19	1560	29.34	2.153119954	
	20	2245	32.37	3.098560446	
	21	2897	35.41	3.998454170	
	22	3425	38.45	4.727202462	
	23	3700	41.49	5.106758864	
	24	4312	44.53	5.951444385	

APPENDIX G: EXTRACT OF THE TABLE FOR FSA

Natural Radionuclide Activity Concentrations						Concentrations (Bq/Kg)		
Energy (keV)	CC K ₄₀	CC Th ₂₃₂	CC U ₂₃₈	Com Sp	Rec Sp	⁴⁰ K	²³² Th	²³⁸ U
331	0.0006415	0.0083175	0.0075823	1.496351136	1.677847125	1266	54	31
332	0.0006490	0.0083300	0.0076095	1.507338690	1.684730091			
333	0.0006511	0.0083357	0.0076368	1.511115163	1.69510965			
334	0.0006374	0.0083413	0.0076642	1.494978631	1.705489209			
335	0.0006237	0.0083468	0.0076975	1.479016740	1.723306895			
336	0.0006101	0.0083499	0.0077323	1.462972054	1.742710877			
337	0.0006137	0.0083530	0.0077671	1.468808360	1.762114858			
338	0.0006175	0.0083561	0.0078110	1.475073362	1.730387876			
339	0.0006212	0.0083509	0.0078608	1.481063673	1.683009188			
340	0.0006199	0.0083455	0.0079105	1.480731586	1.635630500			
341	0.0006169	0.0083401	0.0079656	1.478240987	1.635135778			
342	0.0006138	0.0083085	0.0080282	1.474562724	1.654086003			
343	0.0006128	0.0082738	0.0080907	1.473411727	1.673036227			
344	0.0006143	0.0082391	0.0081542	1.475356653	1.653988384			
345	0.0006157	0.0082264	0.0082207	1.478585895	1.614285772			
346	0.0006137	0.0082192	0.0082873	1.477655396	1.574583159			
347	0.0005979	0.0082120	0.0083529	1.459343573	1.565421734			
348	0.0005821	0.0081562	0.0083973	1.437749161	1.577602413			
349	0.0005664	0.0080801	0.0084417	1.415056255	1.589783093			

$d\sigma/da$	$d\sigma/db$	$d\sigma/dc$	x	y	z	Com Err	Stat Test
-0.0002329	-0.00301918	-0.002752308	-0.010193	-0.1345993	-0.1404286	0.02201408	6.695138304
-0.0002303	-0.00295534	-0.002699704				0.02087634	
-0.0002396	-0.00306744	-0.00281026				0.02240330	
-0.0002684	-0.00351188	-0.003226771				0.02964237	
-0.0003048	-0.00407809	-0.003760847				0.04034956	
-0.0003413	-0.00467159	-0.004326039				0.05348961	
-0.0003600	-0.00489999	-0.004556261				0.05857041	
-0.0003153	-0.00426688	-0.003988547				0.04419136	
-0.0002509	-0.00337283	-0.003174892				0.02753561	
-0.0001921	-0.00258541	-0.002450650				0.01620393	
-0.0001936	-0.00261703	-0.002499536				0.01665221	
-0.0002204	-0.00298313	-0.002882490				0.02185638	
-0.0002447	-0.00330330	-0.003230210				0.02704603	
-0.0002195	-0.00294352	-0.002913192				0.02162819	
-0.0001671	-0.00223263	-0.002231101				0.01245410	
-0.0001190	-0.00159334	-0.001606530				0.00635804	
-0.0001269	-0.00174223	-0.001772115				0.00771071	
-0.0001628	-0.00228135	-0.002348779				0.01360386	
-0.0001979	-0.00282362	-0.002949990				0.02157474	

APPENDIX H: AN EXAMPLE OF A VISUAL FIT OF ONE OF THE MEASUREMENT POSITIONS

